Department of Geomatics Engineering

Sensor Aiding of HSGPS Pedestrian Navigation
(URL: http://www.geomatics.ucalgary.ca/links/GradTheses.html)

by

Oleg Mezentsev

March 2005

UNIVERSITY OF
CALGARY

Abstract

This thesis illustrates how a set of low-cost, self-contained MEMS sensors can be used to aid a High Sensitivity GPS (HSGPS) based pedestrian navigation system in signal-degraded environments. The HSGPS utilizes long dwell time technology and provides excellent signal availability in areas such as urban canyons, where conventional GPS receivers barely provide any position solutions. Large signal attenuation and degradation effects characteristic of downtown areas, along with a high probability of acquiring echo-only or cross-correlation signals through the HSGPS receiver, introduce significant errors in HSGPS measurements. These, in turn, cause very significant position and velocity solution errors. In this situation, it is very hard to estimate measurement errors based on common GPS signal quality characteristics, such as a carrier-to-noise ratio or satellite elevation. Inaccurate estimates of measured signals ultimately result in an unknown distribution of HSGPS solution errors, which present a challenge for the proper modeling of the covariance matrix of HSGPS updates for system integration.

For pedestrian navigation applications, sensor data is mechanized in a pedestrian dead reckoning (PDR) mode, where the position is propagated through the detection of user steps. In this way, errors are proportional to the distance traveled, and not to the time. The analysis of the effects of errors introduced by the primary PDR system parameters, such as heading and step length on PDR position accuracy, is studied. A method for modeling PDR position error growth versus traveled distance for several stochastic step-length and heading drift error models is proposed.

Based on the results of individual system performance analysis, a method to integrate the sensor and HSGPS data is proposed. This proposed method utilizes a

loosely coupled integration technique with an adaptive measurement error covariance matrix. This approach is more robust in tolerating poor position and velocity HSGPS updates that are frequently undetected after receiver autonomous integrity monitoring (RAIM) statistical testing. Optimal filtering results are achieved when the error covariance matrix of the HSGPS measurement updates is based on the user equivalent range error (UERE) assumed for a given urban environment and geometrical dilution of precision (DOP) parameters. In the tests that have been analyzed, the distance root-mean-square (RMS) error of the integrated solution stays below 150 metres more than 95% of the time.

Acknowledgements

There are special people that mean very much or simply everything to me, and I would like to thank them for their help, support and love throughout my abroad education experiences. I am thankful to:

- My **parents** for always believing in me, for your unconditional love and support during my whole life! I can never be thankful enough for what you have done for me.

- My beautiful fiancée **Katia**, for your wonderful love and for your patient wait of me over these several years. Without your love, support and help I wouldn't have done it.

- My supervisor **Gérard Lachapelle** for all his help, guidance, encouragement and support during my pursue of this degree. You have made my work in this research group a wonderful learning experience full of challenges and precious moments that I will remember throughout my life.

- **Jussi Collin** who has not only become my friend but also a partner, who has been an infinite source of ideas for discussion that lead to so many research opportunities over these years.

- The support of my friends and colleagues at the Geomatics department cannot be over-appreciated. Specifically, I would like to thank: **Olivier Julien**, **Glenn MacGougan**, **Diep Dao**, **Mark Petovello**, **Natalya Nicholson**, **Heidi Kuusniemi**, **Chaminda Basnayake**, **Cecile Mongredien**, **Junjie Liu**, **Ross Stirling**, **Leo Soliz** and **Procopio Stein** for their precious suggestions and discussions on my work and for simply being my good friends.

- And to all members of PLAN group at the Department of Geomatics Engineering.

Table of Contents

List of Tables

List of Figures

Notation

Symbols

$\{\bullet\}^-$	...	Prediction of quantity $\bullet$
$\{\bullet\}^+$	...	Updated quantity $\bullet$
$\{\bullet\}^*$	...	Approximated (linearized) quantity $\bullet$
$\{\hat{\bullet}\}$	...	Estimated quantity $\bullet$
$\{\bullet\} \cdot \{\circ\}$	...	Algebraic multiplication of quantities $\bullet$ and $\circ$
$\otimes$	...	Multiplication of quaternions
$\mathrm{E}\{\bullet\}$	...	Expectation of $\bullet$
$f(\bullet)$	...	Function of $\bullet$
$\mathbf{F}$	...	System (or dynamics) matrix
$\mathbf{H}$	...	Design matrix
$H{:}\{\bullet\}$	...	Statistical hypothesis with condition $\bullet$
$\mathbf{K}$	...	Kalman gain matrix
$N(\bullet, \circ)$	...	Normal distribution with ($\bullet$) mean and ($\circ$) variance
$\mathbf{Q}$	...	Process noise matrix
$\mathbf{R}$	...	Measurement covariance matrix
L1	...	GPS Signal Carrier Frequency at 1575.42 MHz
L2	...	GPS Signal Carrier Frequency at 1227.60 MHz
t	...	User clock bias
$\mathbb{R}_i^3$	...	i^{th} 3-D coordinate frame
λ	...	Longitude
ϕ	...	Latitude
$\mathbf{\Phi}$	...	Transition matrix
$\vec{\mathbf{i}}, \vec{\mathbf{j}}, \vec{\mathbf{k}}$	...	Unit vectors in a pre-defined 3D coordinate system
$Var(\bullet)$	...	Variance of $\bullet$
σ	...	Standard deviation
ρ	...	Pseudorange observable
∂	...	Partial derivative
C_l	...	Covariance matrix of observations
H	...	Least squares design matrix
S_r	...	Power of the GPS signal at Earth surface
G_c	...	Gain after coherent integration
G_n	...	Gain after non-coherent integration
a_i	...	Acceleration along i axis

ω	...	Angular velocity
b_ω	...	Gyro bias
f	...	Specific force
b_f	...	Accelerometer bias
$\mathbf{q}$	...	Hamilton's quaternion
Φ	...	Rotation vector
$\mathbf{x}$	...	State vector
Δt	...	Kalman filter step size
$\mathbf{w}$	...	Process noise vector
$\mathbf{v}$	...	Measurement error vector
$\mathbf{P}$	...	Error covariance matrix
$\mathcal{O}$	...	Observability matrix
r	...	Range observable
P	...	barometric pressure
$\mathbf{E}$	...	Easting coordinate
$\mathbf{N}$	...	Northing coordinate
$\mathbf{H}$	...	Heading
$\mathbf{S}$	...	Step length
g	...	Local gravity
N	...	Number of steps
$\mathbf{HR}$	...	Heading rate
$V_{E,N}$	...	GPS East and North velocity
∇	...	Vector containing a blunder

Abbreviations and Acronyms

2D	...	two dimensional
3D	...	three dimensional
AD	...	Analog to Digital
AGPS	...	Assisted Global Positioning System
C/A	...	Coarse Acquisition
CDMA	...	Code Division Multiple Access
DAQ	...	Data Acquisition
DGPS	...	Differential GPS
DLL	...	Delay Lock Loop
DR	...	Dead Reckoning
DRMS	...	Distance Root Mean Square

DOP	. . .	Dilution of Precision
EF	. . .	Earth Fixed
ECEF	. . .	Earth Centered Earth Fixed
FDE	. . .	Fault Detection and Exclusion
FFT	. . .	Fast Fourier Transform
FLL	. . .	Frequency Lock Loop
GNSS	. . .	Global Navigation Satellite System
GPS	. . .	Global Positioning System
GLONASS	. . .	Global Orbiting Navigation Satellite System
HOW	. . .	Hand Over Word
HS	. . .	High Sensitivity
HSGPS	. . .	High Sensitivity GPS
IF	. . .	Intermediate Frequency
IMU	. . .	Inertial Measurement Unit
INS	. . .	Inertial Navigation System
ISA	. . .	Inertial Sensor Assembly
LAAS	. . .	Local Area Augmentation System
LBS	. . .	Location-Based Services
LL	. . .	Local Level
LLA	. . .	Latitude, Longitude and Altitude
LOS	. . .	Line Of Sight
MDB	. . .	Marginally Detectable Blunder
PDA	. . .	Personal Digital Assistant
PDR	. . .	Pedestrian Dead Reckoning
PLL	. . .	Phase Lock Loop
ppm	. . .	Part-Per-Million
PPS	. . .	Precision Positioning Service
PRN	. . .	Pseudo Random Noise
RAIM	. . .	Receiver Autonomous Integrity Monitoring
RF	. . .	Radio Frequency
RLG	. . .	Ring Laser Gyroscope
RMS	. . .	Root Mean Square
SNR	. . .	Signal To Noise Ratio
SPS	. . .	Standard Positioning Service
SSI	. . .	Sum of Squared Innovations
SV	. . .	Space Vehicle
TOA	. . .	Time Of Arrival
TTFF	. . .	Time To First Fix
UERE	. . .	User Equivalent Range Error
UTC	. . .	Coordinated Universal Time

UWB	...	Ultra Wide Band
WAAS	...	Wide Area Augmentation System
WLAN	...	Wireless Local Area Network
WGS-84	...	World Geodetic System - 1984
ZUPT	...	Zero Velocity Update

Nomenclature

In literature, the term *'pedestrian navigation'* is frequently being interchanged with the term *'personal navigation'* that refers to much broader area of positioning such as positioning of people traveling by cars, bikes etc. The term *'pedestrian navigation'* refers only to navigation systems developed for a person on foot.

Chapter 1

Introduction

In the last few years, interest in pedestrian navigation has expanded significantly. Recent technological advances in mobile computing have allowed some mobile technology, such as cellular phones and Personal Digital Assistants (PDA), to have processor power unimaginable several years ago. Technological advances in microelectronics have also reduced the size of a GPS receiver from order of cubic decimetres ten years ago to about the size of a coin. Micro-Electro Mechanical Systems (MEMS) have progressed to a level whereby a full six degrees of freedom Inertial Measurement Unit (IMU) can be compounded in less than one cubic centimetre volume (Barbour and Schmidt, 2001). This miniaturization progress in the electronics industry drives research in other scientific areas. In the science of navigation, one of these new and exciting research areas is the navigation of pedestrians.

Without a doubt, the problem of outdoor pedestrian navigation can be addressed by means of Global Positioning System (GPS) only; that is, by using a stand-alone GPS receiver. Small, inexpensive GPS receivers are widely available for PDAs and are now embedded into new cellular phone models. However, there are obvious problems with this type of navigation: availability, continuity and accuracy of the solution in signal-degraded environments. In very dense urban environments, a navigation system relying solely on a GPS receiver will have significant position errors and will possibly experience long data gaps. Also, this type of navigation system will most likely not comply with the Federal Communications Commission (FCC) E-911 mandate requirements for handset-based solutions (FCC, 2001). A form of aiding

for a GPS receiver that is convenient and suitable for a typical pedestrian user is required. One of the possible forms of such aiding is the use of a miniature self-contained low-cost sensor unit.

This thesis demonstrates how to significantly improve the performance of stand-alone GPS for pedestrian navigation in signal-degraded environments by analyzing the integration of GPS with a set of self-contained low-cost sensors.

1.1 Background

GPS was intended to be a line-of-sight radionavigation system for use in the outdoors. This means that an unobstructed view of GPS satellites is required in order for the system to provide a navigation solution according to the given specifications. In downtown areas, or in any environment where a clear view of the sky is obstructed, the user will quite likely be able to directly observe only one or two satellites, near the zenith. Signals from other satellites may be severely affected by line-of-sight obstacles and may be reflected to the user by numerous reflective surfaces, such as glass windows and nearby cars, causing multipath. Figure 1.1 shows a possible geometry of signals in an urban area where a user can receive both the direct line-of-sight (LOS) and multipath signals from some satellites, and multipath only (echo only) signals from others.

The power of direct GPS signals reaching the Earth is already very low due to the geometric spreading effect, and when additionally faded this power may go to a level many orders below thermal noise. A recent development in GPS technology called High Sensitivity GPS is capable of acquiring and tracking much weaker signals than the conventional power signals at the Earth's surface (Peterson et al., 1997; Garin et al., 1999; MacGougan et al., 2002). It is achieved by employing so-called longer

non-coherent integration of the incoming GPS signals with the receiver-generated signal replicas. In this method, the correlation value is squared prior to dumping to a total correlation value. In so doing, the problem of possible appearance of the data bit transition in the navigation data is overcome. Unfortunately, the noise is also amplified, thus increasing the effects of multipath and the possibility of acquiring a wrong correlation peak (Chansarkar and Garin, 2000).
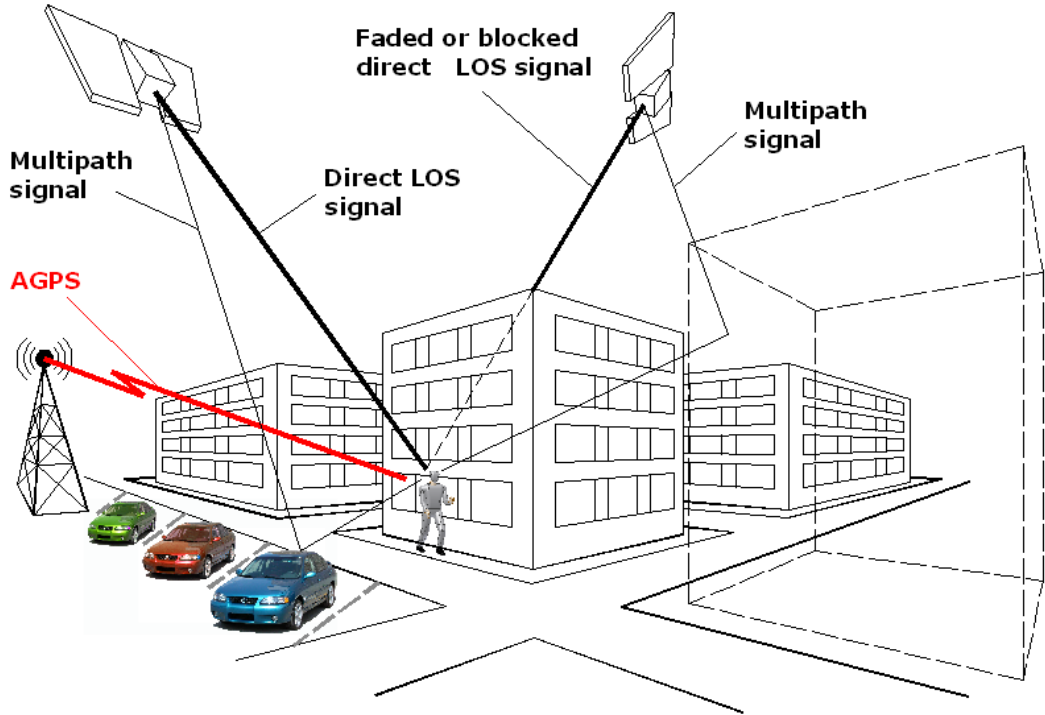
Figure 1.1: Possible Urban Signal Environment

This method has been shown to be capable of tracking signals with fading of up to 25 dBHz (MacGougan et al., 2002). A thorough overview of the current status of HSGPS is given in Lachapelle (2004). The obvious problem that comes with the advantage of tracking very weak signals is the possibility of acquiring (and, generally speaking, tracking) a false correlation peak. Such a peak might be a cross-

correlation peak with a wrong PRN code or a wrong correlation peak with the right PRN code. Both these scenarios are likely to happen when the direct LOS signal is very weak, so the correct correlation peak is very small. Another problem is frequently called the tracking of an echo-only signal. In both cases, the errors caused by tracking the wrong signals will be significantly larger than the errors caused by conventional multipath, when the direct LOS signal is present. Thus, the positioning solution based only on the data from an HSGPS receiver in an urban environment is likely to be contaminated by large position errors caused by the above-mentioned complications.

The significance of the problem of pedestrian navigation might in fact be overlooked if a person thinks of it exclusively as an accessory for leisure activities, where the information does not need to be exact. For example, a pedestrian navigation system may be used for these purposes (Gartnet et al., 2004):

- To find direction and the shortest route to a particular location;

- To provide the user with a walking summary, such as the number of steps made by a user and the approximate distance traveled;

- To keep track of the user's walking path history, with marks of certain locations;

- To help in navigation of visually-impaired;

- To perform as a PDA tourist guide, announcing tourist information depending on the location of the user.

While this type of information is important for a particular group of potential users engaged in leisure activities, it is not exceptionally critical. What is more critical is the knowledge of the user coordinates at the moment of an emergency call, such as E-911 in North America or E-112 in Europe.

Several years ago, the United States Federal Communications Commission established the E-911 mandate that requires wireless operators to be able to locate the position of the originator of an emergency call to within a certain degree of accuracy (FCC, 2001). This mandate essentially started the escalation of the location-based services (LBS) market that is expected to grow from USD 0.5 billion dollars in 2003 to a 28 billion dollar market by 2008. The revised standards for Phase II location, accuracy and reliability of this mandate[1] are the following:

For handset-based solutions: 50 metres for 67 percent of calls, 150 metres for 95 percent of calls;

For network-based solutions: 100 metres for 67 percent of calls, 300 metres for 95 percent of calls.

These requirements are very stringent. The emergency calls may originate from practically any environment, varying from an open sky rural area to the basement of a downtown building. A pedestrian equipped with additional sensors, or a form of aiding to a stand-alone GPS receiver, will have the advantage of more accurately determining his/her coordinates in the case of an emergency call. Forms of aiding to a GPS receiver for a pedestrian can broadly be divided into the following groups:

- Networks aiding: Assisted GPS (AGPS) or differential corrections (network dependent);

- Indoor systems aiding: Pseudolites, Ultra-wide band (UWB), Wireless local area networks (WLAN) (building dependent);

- Sensors-based aiding: INS, PDR (self-contained)

---

[1]Deployment of Phase II FCC's mandate was initiated on October 1, 2001

In terms of networks aiding, there are three types of aiding information a user may get from a cellular network: the current satellite ephemeris, the approximate user location and the approximate time. This approach has been known as Assisted GPS (AGPS). A thorough overview of AGPS can be found in Syrjärinne (2001). If a GPS receiver in a signal-degraded environment is supplied with this aiding information, the acquisition of GPS signals may be made easier and faster. In other words, the bandwidth of the tracking loops can be made smaller, which narrows the time-frequency search of the signals. This approach is nearly *a must* for a receiver in very harsh signal environments.

Cellular networks themselves can essentially act as a positioning system. Methods to calculate a position are many, including time of arrival (TOA), angle of arrival (AOA), cell ID, etc. Navigation systems that provide an integrated solution for GPS and cellular networks are called *hybrid positioning systems*. Descriptions of various positioning algorithms and the recent developments in hybrid systems can be found in Klukas et al. (1997); Biacs et al. (2002) and Ma (2003). In urban areas, accuracy of the cellular network positioning alone with the continuity of the solution is quite poor due mainly to rapidly changing cell geometry. Also, practical implementation of such systems requires installation of quite expensive and complicated hardware at the cell site.

The second item in the list is indoor systems aiding. Using GPS or a hybrid system indoors results in all of the above acquisition/tracking problems (multipath, cross-correlation, echo-only signal tracking) but in a more amplified form. It is likely that a user will not have any direct LOS GPS signals indoors. All of the signals (if any) acquired by the receiver, or tracked while the user entered a building, will likely be severely faded, or there will be complex reflections from windows, walls, etc. The problem of indoor location with GPS is an extreme example of the problem that

will be addressed in this thesis. Research results on the performance of GPS indoors can be found in Soderholm et al. (2001); Haddrell and Pratt (2001); van Diggelen (2001a) and MacGougan et al. (2002). The recent results of testing a HSGPS receiver in an unaided mode are very promising (Lachapelle et al., 2004) and demonstrate that positioning in light-wooden or concrete-type buildings with many windows is possible. However, effective positioning is not yet possible deep in a concrete-type commercial building.

Currently, for many navigation applications indoor, a stand-alone GPS receiver is insufficient. One of the common approaches for indoor navigation (as well as aiding to GPS) is the development of a specific indoor positioning system infrastructure such as UWB or pseudolite transmitters. A quite thorough overview of aiding methods and techniques for a GPS receiver with such methods can be found in Gilliéron et al. (2004); Godefroy and Jeannot (2004). An obvious problem with these techniques is the use of a building-dependent infrastructure that rigorously limits the application of such systems to only certain buildings.

The last item in the list of possible aiding sources for a pedestrian navigation system based on a GPS receiver is the use of a self-contained sensor assembly. A sensor unit may contain just a few-low cost sensors, or it may be a full 6 degrees of freedom IMU or INS. The quality of the IMU may also vary from low-cost to essentially navigation grade if the price and the weight of the designated system permit. For instance, aiding by a high-quality IMU has its own market of high accuracy surveying in signal-degraded environments. These applications may include surveying for the oil and gas industry, precision forestry surveying or mining surveying (Scherzinger, 2004). Such systems are quite bulky and expensive, and they are most certainly impractical for the everyday navigation of pedestrians in, say, urban canyons.

Currently, the most practical approach to aid a GPS-based pedestrian navigation

system is the use of a self-contained MEMS inertial sensor unit. First, these sensors are inexpensive: most MEMS sensors in mass production quantities cost a few dollars. Second, these sensors are truly miniature - usually less than (10x10x5 mm) in size, and they consume little power (< 50 mA). Obviously, these sensors cannot be used in a classical inertial mechanization scheme, even for very short periods of time. Conservatively, the biases of MEMS gyros can be brought down to a level of less than 300 degrees per hour after appropriate temperature compensation. Such a large drift, even assuming an accurate initialization of attitude, will lead to very large position errors after almost 10 seconds of INS-only navigation (El-Sheimy, 2003). However, data from MEMS sensors can still be extremely helpful when the mechanization algorithm exploits the specifics of human walking.

In 1999, Levi and Judd patented the novel idea of using accelerometers to detect the steps of a person walking (Levi and Judd, 1999). For this task, miniature MEMS accelerometers, called pedometers, are the perfect choice. Since 1999, when pedometers were patented, various low-cost pedometers have been marketed, and there has been a lot of research on this subject. Various algorithms to count steps and characterize the motion of a user have been developed. For example, Lee and Mase (2001) studied the acceleration patterns resulting from walking and proposed the recognition model that classifies walking behaviour into predefined groups such as "straight", "upward" and "downward". The use of a pedometer by itself is fairly limited, since the only information it provides is the number of steps performed and the approximate distance traveled.

A sensor system that is equipped with a heading sensor in addition to a pedometer is referred to as a PDR system. Unlike pedometers, there are only a few commercial PDR systems available. The difficulty lies in the problem of integrating a PDR system (which is a relative positioning system) with an absolute positioning system,

such as GPS. There are many problems related to developing a filter that will combine the GPS and PDR measurements to produce a reliable position solution. These problems will be discussed and addressed in great detail throughout this thesis.

1.2   Overview of Research on PDR/GPS Integrated Systems

In the area of PDR navigation, the difficulties and problems associated with Kalman filtering have been clearly overlooked. In most of the work, the user's step frequency is used as the filter time base. In general, steps do not occur at the times of GPS updates. Thus, GPS data have to be interpolated or extrapolated to the time that each step occurs. In most of the work, good quality GPS data (mostly DGPS) have been integrated with the sensors' data; thus, this procedure is somewhat reasonable.

Gabaglio (2001) introduced a Kalman filter for the PDR system integrated with DGPS. In his work, the PDR system is based on a magnetic compass and a metre-accurate differential GPS has been used for the system updates. Few experimental validation results have been presented and the effects of sporadic magnetic disturbances, which are very possible in downtown areas (the environment this system is primarily designed for), have not been addressed. A comparison of PDR systems based on a compass and a gyro is given in Ladetto et al. (2001).

Jirawimut et al. (2000) also presents the results of integration of DGPS and DR techniques for pedestrian navigation. The results were simulated for the case of metre-accurate DGPS on a short trajectory. For the filter developed, it was concluded that a well-tuned system and measurement noise covariance matrices need to be used, which are difficult to adjust for different people and varying GPS environments. An analysis of PDR/GPS integration and map-matching algorithms for an indoor and outdoor PDR system is also reported by Gartnet et al. (2004).

One of the problems in PDR integration is the modeling and calibration of step length. An algorithm to continuously calibrate step length while walking was studied by Ladetto (2000). The use of a PDR system in a handheld device brings new challenges to the design of the integration filter. In this case, the sensor signals may be slightly or significantly damped, due to the motion of the user hands. Also, since the unit is held in hand, its orientation with respect to the user body is not known. Thus, the biggest problem is the detection of the user's motion state and the determination of usefulness of the sensor data.

A lot of interesting research has been accomplished in aiding PDR/GPS with special sensor systems. Currently, these systems target very specific markets, but with new technological developments these techniques may be adopted for everyday use in the future. Recently, Brand and Phillips (2003) have proposed a system using RF signals to estimate step length. A phase discriminator attached to the belt of the user with two RF cables going down along the legs combines with a proposed RF foot-to-foot measurement system. The radio frequency transmitted by one foot is received by the other. Since the length of the cables is known, the only unknown is the distance between the legs. This approach allows a very accurate estimate of step length down to the millimetre level. This hardware can be used on a tactical unit soldier but not as part of an everyday PDR system; in addition, it is rather expensive at this time.

Another interesting implementation of a PDR system is the use of the sensor unit mounted on (or in) the user's shoes. One of the early works on this subject is reported by Elwell (1999). In his work, fairly accurate IMUs have been implemented in the shoes of a pedestrian (as an indoor navigation system for an urban or indoor warrior) and the technique of performing frequent zero velocity updates (ZUPT) at every step has been applied. The problems with this kind of approach are fairly obvious: it requires special shoes, and it is fairly expensive. Recently, very promising research

has been done where a set of low-cost sensors has been tied onto a shoe (Stirling et al., 2005). A model has also been developed that relates the signature of the acceleration profile by the sensor unit on a shoe to the step length. In this model, zero-velocity updates on every step have been applied that help to reduce the drift of gyros to a reasonable value.

Another special form of a PDR/GPS aiding technique is the so-called *visual odometer*. The user wears a camera with special algorithms of image processing to extract navigation information. An analysis and the results of using such a system for pedestrian navigation can be found in Jirawimut et al. (2003); Kourogi and Kurata (2003). The results are somewhat interesting, but this approach is quite impractical.

A very important issue in any integrated navigation system is the reliability testing of the integrated results. Recent results of reliability analysis applied to stand-alone HSGPS are reported in Kuusniemi et al. (2004); Kuusniemi and Lachapelle (2004). It is concluded that the RAIM techniques are not overly reliable when applied to HSGPS observations, due to the frequent presence of multiple blunders at a single epoch. Few works exist on this subject for PDR/GPS integrated systems (Collin et al., 2003a; Lachapelle et al., 2003a), and more analysis is required.

After this brief overview it can be concluded that, until now, most of the research on PDR/GPS systems relies on either expensive, very specific, hardware or the use of precise GPS. Keeping in mind that the aiding of a GPS-based pedestrian navigation system is actually needed only in signal-degraded areas such as downtown, high quality GPS updates are something that are rarely available. An expensive or inconvenient system (i.e. camera or special shoes) is also a rather unreasonable choice for an everyday pedestrian navigation system.

1.3 Objectives of This Thesis

The overall objective of this research is the analysis of a pedestrian navigation system based on a set of low-cost MEMS sensors and an HSGPS receiver. This sensor combination is currently regarded as being the most practical, functional and up-to-date considering cost and implementation factors. It is self-contained (it does not require any specific network or building system infrastructure) and can truly be miniature and inexpensive. The specific objectives of this thesis are:

1. **Analysis of stand-alone HSGPS performance.** The use of HSGPS significantly increases the availability of GPS measurements. In a signal-degraded environment, many of those measurements may be of very poor quality. In other words, the measurements might be severely contaminated by multipath, or they may simply be the result of echo-only signal tracking or even possible cross-correlation tracking. It will be shown that even in the presence of significant redundancy in measurements, detection of such blunderous measurements in a single epoch is a real challenge. The analysis of HSGPS performance will be illustrated on a variety of real field data collected in different urban and indoor environments. A comparison between epoch-to-epoch least-squares (LSQ) and Kalman filtered solutions will be made. An important aspect of GPS receiver initialization will be discussed.

2. **Analysis of a low-cost PDR system.** The use of truly low-cost sensors in a PDR system brings a lot of challenges that have to be addressed. Through real data analysis, an optimal configuration of low-cost sensors for a PDR system is proposed. The choice of optimal sensor data processing techniques is discussed. The main goal of such an analysis is the proper stochastic modeling of the key pedestrian system states, such as step length error and heading rate error, for

further integration of the system with GPS.

3. **PDR/HSGPS Kalman filter design.** Up to now, very little research has been conducted on a detailed analysis of Kalman filtering for PDR/GPS systems. In this work, a thorough analysis of system modeling, depending on the state of the user, is performed. The selection of proper filter states for the given quality IMU and GPS measurements is discussed and evaluated through simulations and experimental results. Important issues of any filtering, such as system observability and state convergence, are also analyzed for a given model.

4. **Integrity analysis.** Various algorithms of integrity analysis for an HSGPS/PDR integrated system are evaluated and the results analyzed. It is shown that the fault detection and exclusion (FDE) methods applied to the stand-alone HSGPS results are frequently not reliable. The applicability of the reliability analysis is discussed for the proposed integrated system since it largely depends on the quality of the system initialization.

1.4 Thesis Outline

Chapter 2 contains an overview of pedestrian navigation technologies. This chapter includes an overview of GPS, mostly covering topics relevant to the stated pedestrian navigation problem. An overview of inertial positioning techniques, inertial sensor types and various mechanization schemes is also given.

Chapter 3 contains an overview of the estimation and reliability theories. The background of state-space modeling and the basics of Kalman filtering are presented. More advanced topics on Kalman filtering, such as filter extension to non-linear systems, aspects of filter initialization, convergence and stability, are then presented.

Elements of statistical testing and reliability theory relevant to the area of navigation are summarized.

Chapter 4 describes in detail the prototyping of the integrated system that is used in this thesis. The system mechanical and electrical design is discussed. The time synchronization of the sensor data with GPS is discussed.

Chapter 5 presents an analysis of a pedestrian dead-reckoning system based on a set of low-cost sensors. Important aspects of PDR mechanization are discussed. Stochastic modeling of the key system parameters is presented. The analysis is carried out through simulations and real data.

Chapter 6 presents an analysis of stand-alone HSGPS in a signal-degraded environment, the city downtown. The results are shown for epoch-to-epoch LSQ and Kalman filtered modes. The results of RAIM analysis applied to the epoch-by-epoch LSQ solution are presented and discussed.

Chapter 7 presents the methodology proposed for aiding HSGPS with a set of low-cost sensors. A step-by-step development of the Kalman filter for a PDR/HSGPS integrated system is presented. A detailed analysis of this system and filter performance is illustrated on simulations.

Chapter 8 presents an analysis of the proposed system and an integration method based on experimental results in the downtown core environment.

Chapter 9 presents the conclusions drawn from this research and gives recommendations for future work.

Chapter 2

Overview of Pedestrian Navigation Techniques

This chapter contains an overview of GPS and inertial navigation techniques related to the problem of pedestrian navigation. GPS methods and the most significant error sources in GPS for a certain environment will be discussed. Finally, an overview of inertial positioning techniques, low-cost inertial sensors and inertial system mechanizations is provided.

2.1   Global Positioning System

After GPS became operational in 1996, the civil share of the GPS market quickly started to grow. Currently, civil applications using GPS include personal and vehicular navigation, airborne applications, surveying, time transfer and many more. Different applications use different signal processing and positioning techniques and algorithms ranging from single point pseudorange-based to multiple reference station real-time kinematic (RTK) positioning. In the scope of this work, no attempt will be made to give a complete overview of the principles of GPS operation. Instead, only GPS topics relevant to the stated problem of pedestrian navigation in urban areas will be discussed. Thorough references on GPS by Parkinson and Spilker (1996) and Kaplan (1996) and more recent books such as Misra and Enge (2001) cover a whole variety of topics related to the system operation, from basic to advanced.

2.1.1 System Overview

Initially, a full GPS constellation was meant to consist of 24 satellites in six orbital planes (Parkinson and Spilker, 1996). Currently[1], there are 28 healthy GPS satellites positioned in six orbital planes as shown in Figure 2.1. Each GPS satellite transmits two signals on two different central frequencies named L1 and L2. The signal on L1 is an open source signal called C/A (coarse acquisition) code and consists of a particular pseudorandom sequence based on the Gold code sequence (ibid). In this overview, the properties and characteristics of the civil C/A code will be discussed. All Gold codes have the very important property of a very distinctive autocorrelation peak that is used as a tracking point in the receiver signal search. The C/A signal essentially consists of three parts (Misra and Enge, 2001):

- **Carrier wave**. 1575.4 MHz for L1;

- **Pseudo-random noise (PRN) sequence with special auto-correlation properties**. PRN sequences are unique for every satellite. C/A codes are generated on a satellite using two 10-bit shift registers and thus are $(2^{10} - 1) = 1023$ bits in length.

- **Navigation message**. The navigation message consists of information on satellite health status, satellites ephemeris, satellite clock bias modeling parameters and a full-constellation almanac.

The method of C/A signal transmission on a carrier frequency used in GPS is phase modulation. In GPS signal processing, it is common to refer to the GPS C/A code as a sequence of 1s and 0s. In practice, however, the magnitude of the second value of the C/A code is -1 rather than 0, so the phase of the signal changes by 180° during

---

[1]as of December 27th, 2004

the phase modulation. The rate of generation of the C/A code is 1.023 MHz or, as C/A code bits are frequently called *chips*, 1.023 Megachips per second. Thus, the length of one full replica of the C/A code of 1023 chips is equal to approximately 1 ms. Transmission of the C/A code is constantly being repeated over and over again.
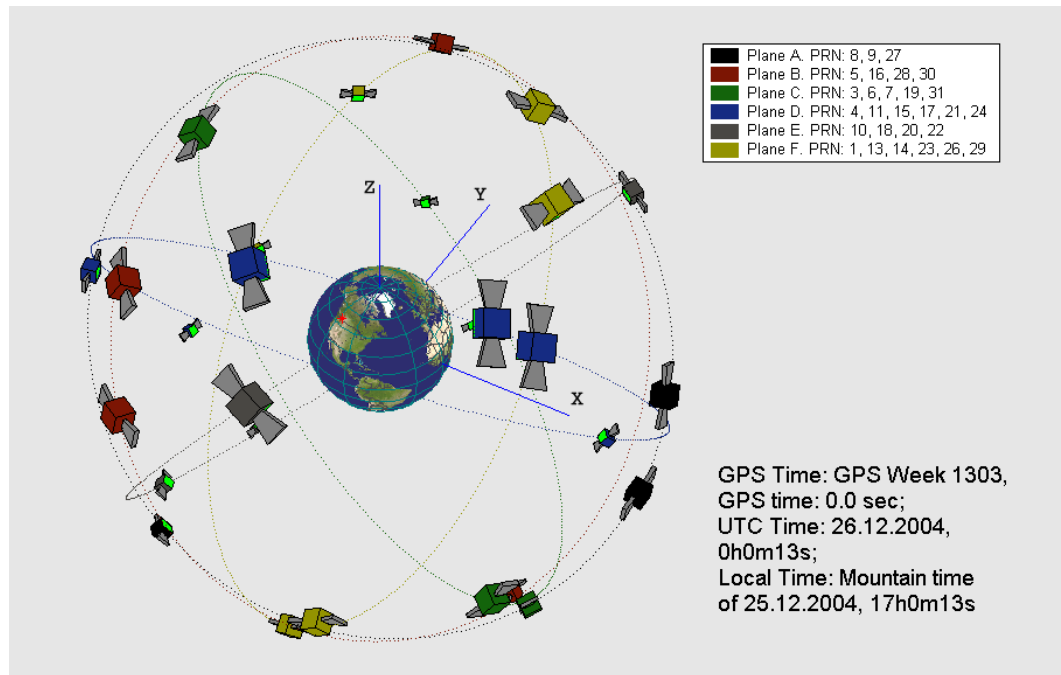
Figure 2.1: GPS Satellite Constellation. The Constellation is Shown at UTC Time of 0:0:13 h, 26 December, 2004 (Larger satellites on the figure mean they are closer to the observer)

The main principle of GPS positioning is the range measurement technique. If the receiver determines the geometrical distances to the GPS satellites with known coordinates, the user coordinates (the antenna coordinates, in fact) can then be determined. To measure the distances to satellites, a GPS receiver generates replicas of the PRN signals for all the satellites being searched. This search is performed in both the code-delay and frequency domains. The code delay is caused by the user to

satellite distance; propagation delay is caused by the media, that is the atmosphere. The frequency shift of the signal is caused by the Doppler effects from the relative satellite to user motion. Due to the clock biases on both receiver and satellite ends and the propagation delay, the range measurement made by the receiver is called the *pseudorange.* If the receiver knows the approximate position of its antenna (through AGPS, for example), then the receiver search can be narrowed to satellites that are theoretically visible to the receiver at a given time.

Nowadays, GPS receivers use massive parallel correlator arrays to correlate the internally generated signal replicas over the code-frequency search space with incoming signals for all satellites. The acquisition time for modern receivers is becoming shorter and shorter. It should be noted that the signal acquisition time and the common characteristic for many receivers of the time to first fix (TTFF) are very different. The acquisition time may be a fraction of a second, while the TTFF depends on whether the receiver has the satellite ephemeris prior to acquiring the signals (AGPS). If the receiver does not have the satellite ephemeris preloaded prior to acquiring satellites, the TTFF may be as much as 45 seconds for a GPS receiver[2] operating under line-of-sight conditions. If the signals are obstructed and weak, the TTFF can increase dramatically. The full ephemeris consists of about 900 bits and is transmitted in the hand over word (HOW) of the navigation message. At the rate of transmission of the navigation message of 50 bits per second, it takes almost 18 seconds for a GPS receiver to receive the full satellite ephemeris. The ephemeris is repeated every 30 seconds in the navigation data. If the ephemeris information is already loaded in the receiver, then the TTFF may be shortened to several seconds.

Once the peak of a certain PRN signal is found, the receiver determines the code delay of the PRN code with respect to its local replica (local time); the frequency shift is

---

[2]For a SiRF HSGPS receiver in cold start mode (www.sirf.com)

determined with respect to the receiver internal oscillator frequency. Two observables are then formed: the pseudorange and the Doppler measurements. This information can now be used in a positioning algorithm to calculate the user coordinates and velocity in a specified coordinate frame.

There is another observable that results in the receiver making the pseudorange measurement. Called a carrier-phase observable, it is the phase of the signal carrier at the time of measurement. This type of measurement is ambiguous to the whole number of cycles that the signal contains on the path from the satellite to the receiver antenna. In carrier-phase positioning methods, this unknown number of carrier cycles is called the ambiguity and is usually estimated using single or double difference techniques in the relative network positioning methods (Kaplan, 1996). The required conditions for the carrier phase positioning method are a change in the geometry of the satellites, and the continuity of the carrier phase measurements. If the continuity of the carrier measurements is satisfied for every subsequent measurement, the unknown number of whole cycles (ambiguity) will remain the same, which assures the eventual convergence of the solution. Carrier-phase positioning techniques are inappropriate for positioning in urban canyons where the continuity of the carrier phase measurements is not achieved, which together with the very poor and rapidly changing satellite geometry makes for a bad combination. This thesis thus provides a discussion of the code-based positioning methods and error sources on the code (pseudorange) measurements.

2.1.2 Coordinate Frames

Before beginning a discussion of positioning algorithms and geometrical solution accuracy measures, the necessary coordinate frames first need to be discussed. Coordinate frames and datums commonly used in navigation and geodesy are well described

in many books, for example Torge (1991). In this section, the coordinate systems that are used in this thesis are briefly covered.

The coordinate datum with respect to which the GPS satellites' coordinates are formed is the WGS-84 coordinate system (Parkinson and Spilker, 1996). This is an Earth Centered Earth Fixed (ECEF) coordinate frame originating at the centre of the Earth. The X axis lies in the Earth equatorial and Greenwich planes; the Z axis points along the axis of the Earth rotation; and the Y axis accomplishes the right-angled frame. This coordinate frame is denoted as XYZ and is shown in Figure 2.2.

A Local Level (LL) coordinate system is the system that is frequently used when the positioning and navigation of an object is performed in a rather small area. It is also a 3D orthogonal coordinate system. Usually, the plane formed by the E and N (standing for Easting and Northing) axes of the LL frame is tangent to the surface of the Earth ellipsoid. The U axis (stands for Up coordinate) points upward, along the normal to the ellipsoid (Figure 2.2). The LL coordinate frame is also used to show the coordinates in a more comprehensive way than is possible in the XYZ and Latitude-Longitude-Height (LLA) coordinate frames. Most of the results in this thesis will be shown with respect to a specified LL coordinate frame. To uniquely define the LL coordinate frame, the coordinates of the LL frame origin with respect to one of the above-described frames must be provided. Coordinate transformations between the WGS84 XYZ, LLA and LL coordinate frames are rather straightforward and are well explained in, for example, Misra and Enge (2001).

Figure 2.2: ECEF, LL and LLA Coordinate Systems

2.1.3 Positioning Algorithms

In this section, methods to calculate user position and velocity based on the pseudorange and Doppler measurements are discussed. The basic user-to-satellite range measurement equations in a given ECEF XYZ coordinate frame (Kaplan, 1996) can be written as

$$
\begin{cases}
\sqrt{(x-x_1)^2 + (y-y_1)^2 + (z-z_1)^2} + ct = \rho_1 \\
\ldots\ldots\ldots\ldots\ldots\ldots\ldots\ldots\ldots\ldots\ldots\ldots\ldots\ldots\ldots\ldots\ldots\ldots\ldots\ldots \\
\sqrt{(x-x_N)^2 + (y-y_N)^2 + (z-z_N)^2} + ct = \rho_N
\end{cases}
\tag{2.1}
$$

where

x, y, z ...   are the user coordinates in the given ECEF coordinate frame, and

x_i, y_i, z_i ...   are the ith satellite coordinates in the given ECEF coordinate frame, and

t ...   is the user clock bias, and

c ...   is the speed of light, and

ρ_i ...   is the pseudorange measurement to satellite i, and

N ...   is the number of visible satellites at the solution epoch.

There are several methods used to solve the system of Equations 2.1, of which the most commonly-used ones are:

1. **Iterative Least-squares (LSQ) method**. In this method, an iterative routine to compute position and velocity through a linearized set of equations is initiated. An initial position guess with a fairly broad proximity of the true position must be provided. This method is fairly computationally robust provided there is redundancy in the observations. The LSQ method of obtaining a position with GPS measurements is used in this thesis.

2. **Closed-form solution**. A set of nonlinear GPS Equations 2.1 can be solved in a closed-form using only 3 or 4 (if height fixing is used) pseudorange measurements. Mostly, the closed form solutions are analyzed to investigate a faster converged, and sometimes more reliable, solution than the iterative LSQ (Bancroft, 1985; Leva, 1996).

In the LSQ solution, the system of Equations 2.1 must be linearized around an initial position. The design matrix is then written as

$$H = \underbrace{\begin{bmatrix} \frac{\partial f_1}{\partial x} & \frac{\partial f_1}{\partial y} & \frac{\partial f_1}{\partial z} & 1 \\ \vdots & \vdots & \vdots & \vdots \\ \frac{\partial f_N}{\partial x} & \frac{\partial f_N}{\partial y} & \frac{\partial f_N}{\partial z} & 1 \end{bmatrix}}_{N \times 4} \tag{2.2}$$

where

$\frac{\partial f_i}{\partial x}, \frac{\partial f_i}{\partial y}, \frac{\partial f_i}{\partial z}$ ... are the direction cosines of the vector pointing from a user position to an ith satellite at the kth epoch in some XYZ EF coordinate frame.

The solution for the system of Equations 2.1 in a least squares sense can be written as

$$\Delta \hat{x} = \left(H^T C_l^{-1} H \right)^{-1} H^T C_l^{-1} \Delta \rho \qquad (2.3)$$

where

$\Delta \hat{x}$ ... is the misclosure vector of coordinates and the clock bias from the linearization point, and

C_l ... is the covariance matrix of observations, and

$\Delta \rho$ ... is the pseudoranges misclosure vector.

The covariance matrix of observations can be assigned in different ways. It is common to form a diagonal covariance matrix (uncorrelated measurements) and assign the observation variances to be equal to, say, 1 m^2 to 10 m^2. However, in the case of HSGPS, methods of proportionally weighting the observations according to certain observation parameters, such as the carrier-to-noise ratio, are used (Wieser, 2001).

A similar set of linearized equations can be written in order to determine user velocity. The same design matrix (Equation 2.3) is used, but instead of pseudorange measurements and user clock bias unknowns, range-rate measurements and clock bias drift terms are used (Kaplan, 1996). The solution is then obtained in a similar LSQ fashion as Equation 2.3.

When the vertical coordinate component (and vertical velocity) is of little interest, as in the case with pedestrian navigation, a method known as *height fixing* can be used. Height fixing is also frequently applied when the number of observations is limited,

especially in a signal-degraded environment such as an urban canyon. Height fixing is usually applied in a LL coordinate frame rather than in XYZ where the height constraint is harder to implement. In the LL coordinate frame, the height coordinate can simply be removed from the set of pseudorange equations, or it can be heavily constrained through a variance adjustment in the LSQ algorithm. Obviously, when height fixing is applied, the redundancy of the solution increases by one, which can be very significant in some cases.

In this work, the LSQ positioning algorithm will be used to process the GPS pseudorange and Doppler observations. It will be noted whenever height fixing is applied.

2.1.4   Error Sources and Accuracy Measures

Undoubtedly, the largest error source for HSGPS in signal-degraded environments is multipath. Multipath is defined as an effect when, in addition to the LOS direct GPS signal, several reflections of this signal are also coming to the user antenna from the surrounding reflective surfaces. Multipath signals are always delayed when compared to the LOS signal because of the longer traveling paths.

The effects of multipath are extremely hard to estimate. Permanently changing satellite geometry and user motion (if kinematic) makes the signal reflections from the surrounding environment truly unpredictable. However, extensive studies have been done on the effects of multipath on receiver tracking performance, and numerous techniques have been developed to decrease the effects of multipath to some extent for line-of-sight signals. The maximum range error introduced by multipath on GPS code signals (when LOS signal is present) is theoretically limited to 150 metres in the case of line-of-sight signals (Parkinson and Spilker, 1996). One of the most successful approaches to multipath mitigation is known as the Narrow Correlator

Spacing technique which is well described by van Dierendonck et al. (1992). The use of an antenna array has also been shown to be successful in the case of line-of-sight signals (Ray, 2000), but it is hardly practical for mobile applications.

A special form of multipath, for which the HSGPS is especially susceptible, is echo-only signal tracking (e.g., Lachapelle, 2003). In this situation, the direct LOS signal is faded to non-acquirable power level, but a few strong signal reflections of the signal still reach the antenna. The range of error caused by this type of multipath is theoretically unlimited.

It is often concluded that the most reliable way to fight multipath is to position the antenna away from all possible reflective surfaces and to use ground plate or choke ring antennas. These suggestions are obviously aimed at reference GPS stations in the outdoors and are not for mobile pedestrian users in urban environments. Thus, in regards to this work, the multipath has to be dealt with through integration with inertial sensors and Kalman filtering in the position domain. It will be shown on numerous field data what level of multipath the user is experiencing in a dense urban canyon environment, and how it is difficult, and sometimes practically impossible, to estimate these effects using only HSGPS measurements.

In the position domain, one of the main performance parameters of a GPS solution is called the dilution of precision (DOP). Dilution of precision is a geometrical factor and represents how accurate the position solution may be, based on the given geometry of the satellite constellation (Kaplan, 1996). There are several geometrical factors, namely, *geometrical* DOP (GDOP), *position* DOP (PDOP), *horizontal* DOP (HDOP), *vertical* DOP (VDOP), and *time* DOP (TDOP). These values are given in the LL coordinate frame, that is in the ENU coordinate frame. The smaller the corresponding DOP parameter, the better the geometry. To compute these DOP values for a given user-satellite geometry, the design matrix, H (Equation 2.2), must

be composed in the LL coordinate frame. Then, a special matrix must be calculated based on this design matrix as

$$D = \left(H^T H\right)^{-1} \tag{2.4}$$

where

H . . . is the design matrix in the LL coordinate frame.

The DOP parameters can then be calculated as shown in Equation 2.5.

$$GDOP = \sqrt{D_{11} + D_{22} + D_{33} + D_{44}}; \quad PDOP = \sqrt{D_{11} + D_{22} + D_{33}}$$
$$HDOP = \sqrt{D_{11} + D_{22}}; \quad PDOP = \sqrt{D_{33}}; \quad TDOP = \sqrt{D_{44}} \tag{2.5}$$

From a practical point of view, especially for pedestrian navigation when horizontal coordinates are of more importance, the HDOP factor is frequently of more interest. In a geometrical perspective, the satellite geometry that provides a better HDOP (smaller value) must include a larger volume in the 3D figure that is formed by connecting the user with all satellites used in the solution. Since for 3D positioning, a minimum of four satellite observations is required, it means that the more satellites there are spread around the sky, the better. Geometry that is composed with only satellites of high elevation will be quite poor. Figure 2.3 shows two cases of satellite geometries using only four satellites. In one plot, only satellites with high elevation have been selected, and in the other, satellites with rather low elevation have been chosen. In the case of "good" geometry (diversity in satellites), the HDOP factor is quite small, 2.61. On the other hand, when only satellites with large elevations are used ("bad" geometry), the HDOP factor is quite large and is equal to 4.71.

These HDOP values are fairly large because only four satellites have been used. When all visible satellites are used to calculate geometrical factors, these DOP values become significantly smaller. Figure 2.4 shows all 10 visible satellites and the
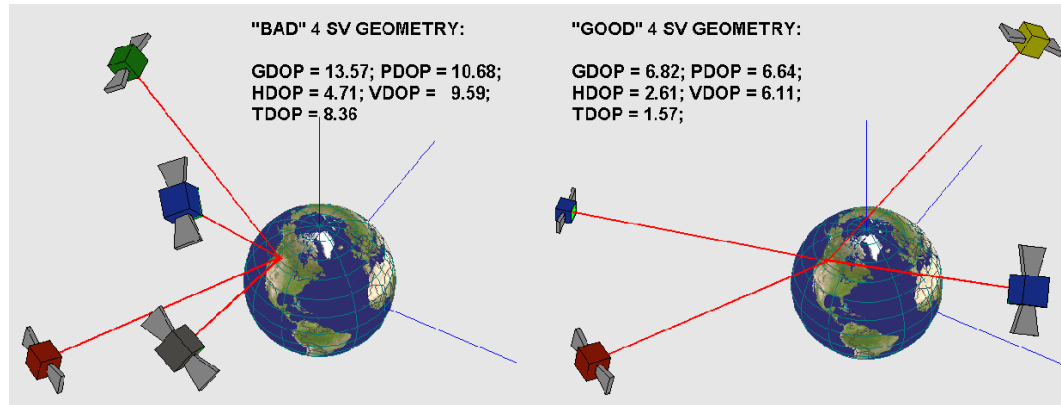
Figure 2.3: DOP Factors Calculated at Calgary Location for "Good" and "Bad" Four Satellite Geometries. "Good" Geometry Satellites are # 3,4,19,21 at UTC Time of 0:0:13 h, 26 December, 2004. "Bad" Geometry Satellites are # 4,5,9,15 at UTC Time of 0:0:13 h, 26 December, 2004.

corresponding DOP factors in Calgary at UTC time of 0:0:13 h, 26 December, 2004. In this case, for example, the HDOP value is significantly smaller and is equal to 1.6.

The geometrical DOP values can be converted to the expected position domain accuracy by multiplying the DOP factor by the estimated user equivalent pseudorange error (UERE). Assuming mild values for atmosphere and multipath errors, the current GPS system UERE can be taken as approximately 5 metres (1σ). The expected horizontal accuracy of the solution (1σ) can then be estimated according to

$$\sqrt{\sigma_E^2 + \sigma_N^2} = HDOP \times \sigma_{UERE} \tag{2.6}$$

where

σ_E, σ_N ...   are the corresponding 1σ Easting and Northing position accuracy, and

σ_{UERE} ...   is 1σ pseudorange error.

An approach to the selection of satellites in urban canyons based on the geome-
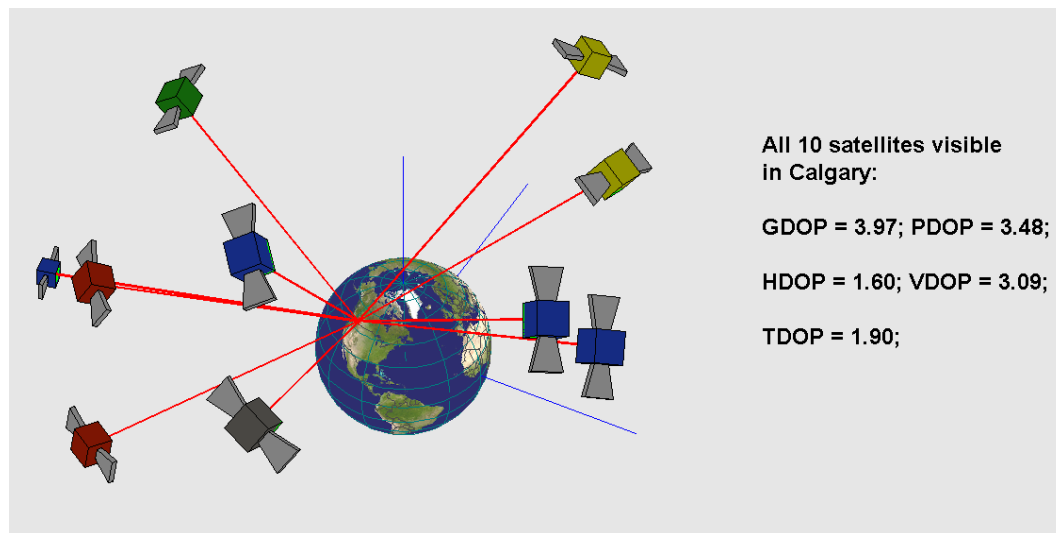
Figure 2.4: DOP Factors for Calgary for all visible Satellites. The satellites visible are # 3;4;5;9;11;15;19;21;22;27 at UTC Time of 0:0:13 h, 26 December, 2004.

try factor is somewhat ambiguous. In a downtown area, there is more chance that the satellites with low-elevation (that can potentially deliver better geometry of solution) will be either severely attenuated or be echo-only reflections of the direct LOS paths. In both these cases, the pseudorange measurement errors might be very significant. On the other hand, signals from satellites that are closer to the zenith (potentially bad solution geometry) have less possibility of being severely faded. Essentially, due to poor overall visibility of satellites in downtown areas, it is frequently not possible to select or reject observations based on the geometry factor. If only four measurements are available and the user is seeking a 3D solution, all four of these observations must be used in the solution, despite any geometrical considerations.

The most fundamental GPS signal characteristic that can potentially describe the quality of the acquired GPS signals is the carrier-to-noise (C/N_0) ratio. The C/N_0

parameter is independent of the receiver type and can be computed as

$$C/N_0 = S_R + G_a - 10 \log \cdot (K_B \cdot T_0) - NF \qquad (2.7)$$

where

S_R ... is the power of the GPS signal at the Earth's surface, and

G_a ... is the antenna gain, and

$10 \cdot \log (K_B \cdot T_0)$ ... is the ambient noise density (dBW-Hz), and

NF ... is the receiver noise figure.

The C/N_0 parameter is representative of the GPS signal quality. A typical C/N_0 value for a GPS signal in the open sky is about 43 dB-Hz. In an urban downtown environment, a lower the C/N_0 means that there are more chances that the signal is faded by LOS obstacles, or that it is affected by multipath. The C/N_0 values for GPS signals in downtown environments can be reduced to 20-23 dB-Hz. Thus, it seems reasonable to assign the covariance matrix of the observations in Equation 2.3 based on C/N_0 values. This statement, though, is not always true, primarily because of the high probability of echo-only signals with significant power. In this case, the relation between the UERE error and the power does not hold. The range error can be very significant and this will not be reflected in the weighting of the observation based on the C/N_0 value.

The C/N_0 parameter is also used to compute an important (receiver dependent) parameter called the Signal-to-Noise (SNR) ratio. The SNR parameter depends on the integration method used in the receiver and is discussed in the following section on the High Sensitivity GPS method.

Atmospheric effects are other significant sources of error in GPS. Atmospheric effects on GPS signal propagation can be divided into ionospheric and tropospheric com-

ponents. These mediums result in additional delays in the propagation time of the signals. The delays depend on several factors, such as satellite elevation, the time of day and the amount of moisture in the troposphere, and the level of ionospheric activity. Ionospheric effects can be modeled and estimated to some extent, especially when using dual-frequency GPS receivers. The accuracy of estimation of atmospheric propagation delays (especially for the ionosphere) in single-point positioning mode is essentially limited. When compared to the errors caused by multipath or echo-signal tracking in urban canyon signal environments, these types of atmospheric errors can be treated as minor. For instance, over 90% of the troposphere effect can be removed using a standard model, leaving a range error well below 1 m (Kaplan, 1996). The ionosphere induced delay can be estimated with the broadcast model with accuracy better than 10 metres. In case of a wide area augmented receiver (WAAS) which uses an ionospheric grid model, residual error is expected to appear less than 3 metres.

2.1.5   High Sensitivity GPS

During propagation from a satellite to a user's antenna, GPS signals experience losses. The radiated power by a GPS satellite is equal to about 27 W. The final power of the GPS signals received by users on Earth is equal to approximately -160.0 dBW. The total GPS signal power budget is summarized in Table 2.1.5 (Lachapelle, 2003).

Such a low power signal is well below the thermal noise power in the receiver, even for a 2 MHz receiver tracking bandwidth. The GPS receiver is able to acquire and track such low power signals by using the process of coherent correlation. By exploiting the properties of the Gold code, which has a very distinctive autocorrelation peak, during integration (correlation) this peak grows faster than the noise. The integration gain during the correlation process for a 2 Mhz bandwidth receiver (main lobe of the C/A

Table 2.1: GPS Signal Power Budget

Characteristic/Parameter	Value
SV radiated power (dBW)	26.8
Free space loss (dB)	-184.4
User antenna gain (dBW)	3.0
Atmosphere attenuation (dB)	-2.0
Depolarization Loss (dB)	-3.4
Received power by user (dBW)	-160.0

code only) can be computed as (van Diggelen, 2001b)

$$G_c = 10 \log (N) \tag{2.8}$$

where

G_c ... is the gain after coherent integration (dB), and

N ... is the integration time (s).

High Sensitivity GPS is known as a technology that utilizes longer integration of signals to make signal peaks visible out of noise even for very low-power GPS signals (Peterson et al., 1997). This process is called non-coherent integration. Generally speaking, in this technique the correlation values are squared prior to dumping to a total correlation value due to the possible presence of navigation data bit transitions in the signals. The problem with such a longer integration (squaring of the correlation value) is the growth of noise. The total gain using coherent and non-coherent integration can be given by (van Diggelen, 2001b)

$$G_n = 10 \log (N) + 10 \log (M) + S_l \tag{2.9}$$

where

G_n ... is the gain after coherent and non-coherent integration (dB), and

N ... is the coherent integration time (s), and

M ... is the number of non-coherent accumulations, and

S_l ... is the squaring loss due to non-coherent accumulation.

This method of coherent integration and longer non-coherent accumulation allows the receiver to achieve approximately 30 dB more processing gain (Ray, 2002). Such a large additional processing gain makes it possible to target signals with a power as low as -188 dBW (Ray, 2002). The SNR parameter for a given GPS signal can then be computed as

$$SNR = C/N_0 + G_{c,n} \qquad (2.10)$$

where

C/N_0 ... is the signal to noise ratio for a given GPS signal (dB-Hz), and

$G_{c,n}$ ... is either coherent or non-coherent integration gain (dB).

In practical terms, the SNR acquisition threshold for low-power GPS signals for a static GPS receiver is currently equal to approximately 10 dB (ibid). The tracking SNR threshold is an ad-hoc parameter that depends on receiver time and user dynamics, and it can be taken as approximately 5 dB for a mild dynamics case of an HSGPS receiver. Signals with lower SNR values are now practically untraceable. Let us consider one example. Suppose, a very low power GPS signal with a C/N_0 of 30 dB-Hz is available. With the use of conventional coherent integration of 12 ms, the resulting SNR is equal to 5.8 dB. This SNR is too low to be acquired by a conventional GPS receiver. If the signal is integrated coherently for 12 ms and then accumulated in a non-coherent manner for about 500 ms, then the SNR is equal to about 19 dB. This assumes a squaring loss of about 3 dB for the pre-squaring SNR of 5.8 dB (van Diggelen, 2001b). The SNR value of 19 dB is already significant and can be acquired by the HSGPS receiver.

2.2 Inertial Navigation

2.2.1 History and Overview of Inertial Navigation

The science of inertial navigation essentially started in 1852 when Leon Foucault first designed a gyroscope. That gyro was a fast-rotating rotor in a gimballed suspension and Foucault planned to observe the rotation of the Earth with respect to the (motionless) stars. The experiment was not that successful, but it prompted vast scientific and engineering research on the design of gyroscopes and other inertial sensors, such as accelerometers.

Probably the first significant success in gyroscopic engineering was the development of a gyroscopic compass in the early 1900s. The gyroscopic compass measures the Earth's rotation vector with high precision in a projection to the local horizontal plane axes. Such projections make it possible to determine the orientation of those axes with respect to the geodetic north direction. This instrument has allowed ships and submarines to navigate more reliably in high latitudes where magnetic compassing has always been troublesome. Nowadays, most ships, submarines, aircraft and spacecraft are equipped with some form of an inertial system.

The gyroscope is an instrument that is capable of sensing the rotation of an object on which it is installed w.r.t to an inertial frame. An inertial coordinate frame can be any coordinate frame (with the associated time scale) that is neither accelerating nor rotating with respect to a *absolute* coordinate frame (Ishlinskii, 1987). An absolute coordinate frame is an abstraction in the science of classical mechanics that represents the unmoving universal space of the universe with respect to which the motion of objects is analyzed. The Galileo equivalence principle states that every inertial coordinate system is equivalent, that is the movement of an object with respect to any inertial frame follows Newton laws. For an analysis of the movement of objects

on or near the Earth, an inertial frame with its centre at the centre of the mass of the solar system and axes fixed with respect to distant motionless stars can accurately be used (ibid).

There are many types of physical phenomena that can be used to build a gyroscope. The basic theoretical principle of the traditional (oldest) type of gyroscope is based on the fact that a quickly rotating body with one fixed point (such as a finger top) without external forces tries to preserve its axis of rotation in inertial space. One of the newer types of gyroscopes, called ring-laser gyroscopes (RLG), is based on a totally different phenomena (Sagnac effect) where the two electromagnetic waves emitted in opposite directions travel different paths around a closed loop when this closed loop is rotating in its plane with respect to an inertial frame (Titterton and Weston, 1997). The operational principle of MEMS gyroscopes are discussed in more detail in the next section.

Another type of an inertial device is an accelerometer. An accelerometer, sometimes called a gravimeter, is a device for measuring an object's acceleration and the effects of gravity. According to the general relativity theory's principle of equivalence, the effects of gravity cannot be distinguished from the effects of an object's acceleration. Therefore, an accelerometer cannot make the distinction between these effects. When an accelerometer is static in an inertial frame, it measures the sum of gravitational forces acting on the sensing element.

The simplest form of an accelerometer can be represented by a mass suspended on a spring that is limited to one axis movement. Since the mass reacts to gravitational and external forces, the pickup from the spring length is proportional to the sum of the external and gravitational forces and, thus, can be converted to an acceleration measurement. Nowadays, this pendulous principle of accelerometer work is used for nearly all types of MEMS accelerometers. As an interesting note, it can also be

mentioned that a gyro can be used as an accelerometer as a device called *a gyroscopic integrator of linear accelerations.* Such a device represents a 3-axis gyroscope with a shifted centre of mass with respect to the axis origin. An acceleration or gravitational force acting on this shifted centre of mass causes the gyroscope to precess with an angular speed proportional to the experienced acceleration.

Traditionally, inertial navigation systems are constructed so that accelerometers are positioned on a platform that is kept in the same orientation with respect to inertial space with the use of gyroscopes. This platform configuration of the inertial system is called a Cardano[3] suspension. This suspension in its simplest form consists of three concentric circles that freely rotate inside each other. Gyroscopes and small motors are required to keep the internal frame in the same position it was set in at the beginning of the vehicle movement. The gravity vector with respect to the initial platform position is known (through the initial alignment procedure), resulting in the removal of the Earth's gravity from the accelerometer measurements.

The main principle of inertial navigation is the measurement of acceleration in a given reference frame and its double integration to get a position as shown below

$$\Delta \xi = \int_{t_1}^{t_2} \int_{t_1}^{t_2} (a_\xi - g_\xi)\, dt dt, \quad \text{and} \quad V_\xi(t_1) = V \tag{2.11}$$

where

$\Delta \xi$ ... is the position increment along ξ axis for time period (t_1, t_2), and

a_ξ ... is the measured acceleration along ξ axis, and

g_ξ ... is the total gravitational acceleration projection on ξ axis, and

$V_\xi(t_1)$ ... is the velocity along ξ axis at time t_1.

Due to this integration, all inertial systems are relative navigation systems in nature.

---

[3]named after Girolamo Cardano (1501-1570)

At the very least, the initial position and initial velocity of an object must be provided in order to propagate the position and velocity solution forward.

Over the years, mechanical gimbaled inertial systems have become extremely complicated from virtually all engineering perspectives. However, they offer superb performance. Difficult in design, expensive to make and usually very large and heavy, mechanical inertial systems continue to be the main navigation systems of submarines, spacecraft and military missiles, where performance is the primary goal.

Due to recent developments in computer technology, another alternative algorithm of inertial navigation has been developed, called the strapdown inertial navigation system. In this setup, the inertial sensors, gyroscopes and accelerometers are assembled in a perpendicular fixed triad scheme; this assembly, in turn, is directly mounted onto the vehicle's body. In this strapdown mechanization, algorithmic calculation is performed to keep the system orientation in inertial space instead of a mechanical platform. Gyroscope measurements are used to keep track of vehicle attitude. The computed attitude is then used to transform the measured acceleration from the body frame to a desired coordinate frame of navigation Finally, after the gravity removal, the integration of acceleration into velocity and position increments can be performed (Equation 2.11).

The difference between the two inertial system realizations can be shown in the following example (Figure 2.5). Suppose that one is interested in the 2D positioning of a missile flying in a known ballistic plane[4]. Before beginning the test, we know the object's initial coordinates and speed, which, in this case, are equal to zero. In this simplified example, in order to calculate the missile position in that plane at any given time, we need to know the acceleration along the axis of the missile (assuming

_____

[4]it is hard to show the gimballed inertial system on a pedestrian; therefore, this example is being used even though it is slightly off-topic

the speed along the axis is a much larger lateral movement) and the angle between the missile axis and the coordinate frame.
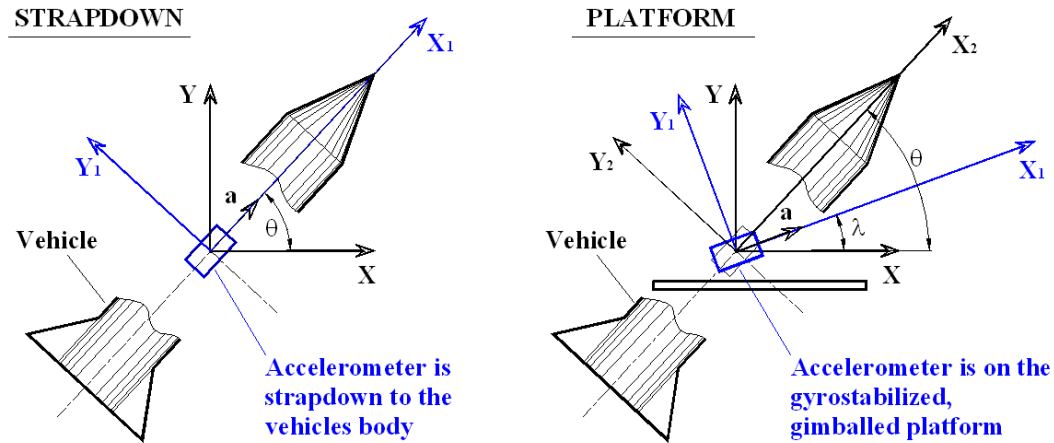
Figure 2.5: Gimballed vs. Strapdown Accelerometer Installation. On this figure: **XY** is the navigation coordinate system, $\mathbf{X_1 Y_1}$ is the accelerometer coordinate system, and $\mathbf{X_2 Y_2}$ is the vehicle body coordinate system.

In strapdown mechanization, the accelerometer is attached directly to the object's body. In order to compute the **X** and **Y** local level object coordinates, the angle θ must be known. This is performed by the gyroscope with the sensitivity axis perpendicular to the plane where the object intends to move. In the mechanical gimballed platform, the accelerometer is installed on the plate that keeps its orientation with respect to the inertial plane (in here, the LL **XY** plane). Therefore, the angle λ is constant during the flight and is known before the object starts moving[5].

Mechanical inertial systems are still being developed because they deliver unmatched, unaided performance that is still much needed in some applications. Mechanical systems were briefly discussed here to better illustrate the idea of inertial system positioning. It should be obvious that any MEMS inertial system is built based on

---

[5]the angle λ does not necessarily have to be zero

the strapdown configuration concept.

Usually, inertial systems are classified according to their assembly type and whether any type of navigation computer is used as a part of the system. The common inertial system classification is shown in Table 2.2 (e.g., El-Sheimy, 2003). The MEMS sensor assembly used in this thesis represents an inertial sensor assembly (ISA), rather than any other type of system. A detailed description of the system assembly used in this thesis is given in Chapter 4.

Table 2.2: Classification of Inertial Systems

Inertial Sensor Assembly (ISA)	The unit outputs the raw sensor measurements
Inertial Measurement Unit (IMU)	The sensor outputs are compensated for errors such as scale factors and biases
Inertial Navigation System	The sensor outputs are fed into a navigation computer inside the system so the position, velocity and attitude are estimated. The unit may also output the compensated raw sensor measurements.

2.2.2   MEMS Sensors

MEMS devices can be seen as simplified versions of the larger instruments because they are generally based on the same operational principles as the classical types of accelerometers and gyros. This section provides a brief overview of MEMS sensors, their principles of operation and the classification of the main errors. A good overview of current state-of-the art MEMS sensors can be found in Barbour and Schmidt (2001).

MEMS Gyroscopes

The main type of MEMS gyros is the vibrating type of gyroscope. In this gyro, a sensing element (a wheel) is rotated in a sinusoidal manner around a torsion spring with a certain frequency. Often, it is the torsion suspension resonant frequency. If this system is rotated around any axis other than the axis of its internal in-plane vibration, the Coriolis force causes the wheel to vibrate in the plane perpendicular to the plane of the wheel, (for example, Grewal et al. (2001)). This vibration is picked-up by the sensing capacitors and is proportional to the angular speed of sensor rotation. Essentially, this vibrating Coriolis effect is the main operational principle for all quartz and silicon micromachined gyros. Basically, all MEMS gyros can be classified as follows: vibrating beams, vibrating plates, ring resonators, and dithered accelerometers (Barbour, 2004). As in the traditional mechanical systems, it is harder to improve the performance of MEMS gyroscopes than it is to improve the performance of the MEMS accelerometers. The gyros carry on as the cornerstone of the inertial navigation, but research is ongoing. An exhaustive overview of the MEMS gyros under development can be found in Shkel (2001).

The measurement equation for a gyroscope that includes the most significant errors common for a MEMS gyro type can be written as

$$G_\omega = \omega + b_\omega + S \cdot \omega + \varepsilon(\omega) \tag{2.12}$$

where

G_ω ... is the gyro measurement, and

ω ... is the true angular velocity, and

b_ω ... is the gyro bias, and

S ... is the gyro scale factor error, and

$\varepsilon(\omega)$ ... is the gyro noise.

Theoretically, all of the error parameters in Equation 2.12 can be estimated in the integration scheme, provided good quality GPS measurements are available and a careful observability analysis of the system is done. When HSGPS data of poor quality is used in the system, the MEMS gyro errors cannot be observed separately; since such separation will require GPS errors to be very small (Scherzinger, 2004). Therefore, they are modeled simply as a gyro bias. Presented as one error, the gyro bias will include all of the above errors, such as a turn-on to turn-on bias, scale factor instability and noise. More on this will be given in Chapter 7 on sensor integration methodology.

MEMS Accelerometers

The main types of MEMS accelerometers include *pendulous* and *resonant* accelerometers. In the pendulous type of accelerometers, a sensing element (proof mass) is placed on a hinge that allows the sensing mass to move along only one axis. The accelerometer control scheme tries to keep the proof mass in the same plane. The force required to do this is proportional to the experienced acceleration. In resonant accelerometers, the acceleration is measured by the change of the vibration frequency of the sensing element due to the experienced acceleration (Barbour, 2004).

A more detailed description of MEMS accelerometers' operation principles can be found in, for example, Grewal et al. (2001). The reported accuracy achievable with pendulous types of MEMS accelerometers ranges from 1 mg to practically 25 μg biases (Barbour, 2004). The resonant accelerometers can potentially deliver a higher accuracy of 1 μg bias (ibid). The output of the accelerometer, that is the specific force, can be given by (El-Sheimy, 2003)

$$A_f = f + b_f + S_1 \cdot f + S_2 \cdot f^2 + \delta g + \varepsilon\left(f\right) \qquad (2.13)$$

where

A_f ...   is the accelerometer measurement, and

f ...   is the true specific force, and

b_f ...   is the accelerometer bias, and

S_1 ...   is the accelerometer linear scale factor error, and

S_2 ...   is the accelerometer non-linear (quadratic) scale factor error, and

δg ...   is the gravity anomaly (deviation from the theoretical gravity value, and

$\varepsilon(f)$ ...   is the accelerometer noise.

Also, in a properly designed integrated system provided good quality GPS measurements are available, it is common to include these accelerometer errors into the state error model. In the case of pedestrian reckoning, accelerometers are only used for the detection of steps; the estimation of these errors is simply not required. Also, as in the case with MEMS gyros, these errors cannot be estimated because of the poor quality of the HSGPS data in urban downtown.

The overview of the current state of the art MEMS gyro and accelerometer technology and expected quality in near future can be found in Barbour (2004).

2.2.3   Strapdown Inertial System Attitude Algorithm

As will be discussed in Chapter 5, PDR mechanization is very different from classical inertial mechanization schemes that exploit double integration of acceleration methods. The one thing that is very similar is the attitude computation algorithm of the PDR system when the gyros are used for heading determination.

The attitude computation algorithm can broadly be divided into two parts: *Initial Alignment* and *Attitude Updating*. In the period of initial alignment, the orientation of the strapdown sensor unit with respect to a certain coordinate frame, most often

the LL ENU coordinate frame, is performed. During user motion, the attitude of the system is updated using the gyro measurements. In this section, a brief overview of the attitude updating algorithm is presented.

Attitude Propagation Algorithm

An orientation of one coordinate frame with respect to another coordinate frame, i.e. the attitude, can be expressed in several ways, such as a direction cosine matrix, Euler angles or quaternions. In this section, a brief overview of attitude updating using quaternions is given because it is the most convenient and computationally efficient way.

Quaternions make the rotations of vectors between the coordinate frames convenient, robust and computationally efficient. Hamilton's quaternion is defined as a hyper-complex number as (Hamilton, 1847)

$$\mathbf{q} = q_0 + q_1 \cdot \vec{\mathbf{i}} + q_2 \cdot \vec{\mathbf{j}} + q_3 \cdot \vec{\mathbf{k}} \tag{2.14}$$

where

q_0, q_1, q_2, q_4 ... are the four quaternion constituent numbers, and

$\vec{\mathbf{i}}, \vec{\mathbf{j}}, \vec{\mathbf{k}}$ ... are the unit vectors of a 3D orthogonal coordinate systems.

From a rotational point of view, the three constituent numbers of a quaternion, namely q_1, q_2, q_3, together with the unit vectors, define a vector in space around which the rotation takes place. The fourth number, q_0, represents the degree of rotation around this vector. Quaternions, obviously, can be used to rotate vectors between the coordinate frames as well as to rotate a vector in the same coordinate frame. To rotate a vector, $x_{\mathbb{R}^3_1}$, from a 3-dimensional coordinate frame $\mathbb{R}^3_1$, to a

vector $x_{\mathbb{R}_2^3}$ of a coordinate frame $\mathbb{R}_2^3$, the quaternion equation is used, namely

$$\left[0, x_{\mathbb{R}_2^3}\right] = \mathbf{q} \otimes \left[0, x_{\mathbb{R}_1^3}\right] \otimes \mathbf{q}^{-1} \tag{2.15}$$

where

$\mathbf{q}$ ... is the quaternion of rotation between coordinate frames $\mathbb{R}_1^3$ and $\mathbb{R}_2^3$, and

$x_{\mathbb{R}_1^3}$ ... is vector x in coordinate frame $\mathbb{R}_1^3$, and

$x_{\mathbb{R}_2^3}$ ... is vector x in coordinate frame $\mathbb{R}_2^3$.

Quaternions are represented using four numbers, but actually only three of them are independent, as only three independent parameters describe the transformation of one 3D coordinate frame to another. The fourth quaternion parameter is dependent on the condition of normality, that is, the unit length quaternions are used to represent rotations. It is common to say that a quaternion represents an orientation of one coordinate frame with respect to another. A detailed description of quaternion techniques for mobile positioning applications can be found in Collin (2001).

Let us define a quaternion that represents a current ISA attitude with respect to LL ENU frame as $\mathbf{q}_t$. To form a quaternion update from the gyro measurements to update the attitude quaternion $\mathbf{q}_t$ at time t to time $(t+1)$, the gyro measurements have to be converted into angular increments along three axes of a body frame - $(\Phi_x, \Phi_y, \Phi_z)_b$ for the period of time $(t; t+1)$. Then, the so-called rotation vector is formed - $\Phi(\Phi_x, \Phi_y, \Phi_z)$. The quaternion $\mathbf{q}_{t+1,t}$ and the quaternion numbers that represent the rotation from a new (rotated according to the gyro measurements) coordinate frame to the previous one (represented by $\mathbf{q}_t$) can be formed according to

$$q_0 = \cos\frac{|\Phi|}{2}; \quad q_1 = \frac{\Phi_x}{|\Phi|} \cdot \sin\frac{|\Phi|}{2}; \quad q_2 = \frac{\Phi_y}{|\Phi|} \cdot \sin\frac{|\Phi|}{2}; \quad q_3 = \frac{\Phi_z}{|\Phi|} \cdot \sin\frac{|\Phi|}{2} \tag{2.16}$$

where

$|\Phi|$ ... is the l_2-norm of the rotation vector Φ.

The attitude quaternion that represents the new orientation of the ISA at time $(t+1)$ can be written as Equation 2.17.

$$\mathbf{q}_{t+1} = \mathbf{q}_{t+1,t} \otimes \mathbf{q}_t \qquad (2.17)$$

Equation 2.17 is the essence of the quaternion attitude propagation algorithm. The smaller the step of the update, the more accurate the attitude computation. There are numerous issues with precise attitude algorithms, such as coning and sculling errors, and these are addressed in great detail by Savage (1998).

2.2.4   Principles of Attitude System Alignment

There are numerous methods of attitude system alignment which can broadly be divided into *static* and *kinematic*. Kinematic alignment is frequently called *in-motion* alignment procedure. Kinematic alignment requires fairly good quality GPS measurements, but this procedure will not be addressed in this thesis. In these paragraphs, we will cover the principle of static alignment of the MEMS based strapdown IMU.

Every static alignment procedure is usually divided into two parts: *horizontal* and *azimuth* alignment. Horizontal alignment can be performed by using accelerometers and can be seen as a self-contained procedure that is capable of being performed by the IMU itself. Actually, the azimuth alignment can also be accomplished in a self-contained manner, in a process called gyrocompassing. In this method, highly accurate gyroscopes with drift rates far below the Earth's rotation rate are required

(Titterton and Weston, 1997). If MEMS gyros are used, gyrocompassing is simply impossible. Methods of azimuth alignment for a PDR system, later referred to as heading initialization, are discussed in Chapter 5.

As has been mentioned earlier, the purpose of the alignment procedure is to determine the orientation of the IMU body frame (the sensors' sensitivity axes) with respect to another coordinate frame, for example, a Local Level coordinate frame. Figure 2.6 shows an alignment procedure that is suitable for a low-cost MEMS inertial system. This alignment can usually provide a sub-degree of accuracy that is sufficient for a PDR algorithm (Chapter 5) that does not utilize classical acceleration integration.

Suppose that angles η and ξ, the angles between the horizontal EN plane and body frame axes X and Y, are small. This is a valid assumption since several similar alignment steps can be performed. In the case of a static IMU, angles η and ξ are measured by accelerometers since the only acceleration they measure when static is gravity. Horizontal alignment can be accomplished in two subsequent rotations. The first rotation takes place around axis X counterclockwise on the angle ξ (**B** on Figure 2.6) on and is defined by

$$
\begin{aligned}
[0, x_{X'Y'Z'}] &= \mathbf{q}' \otimes [0, x_{XYZ}] \otimes (\mathbf{q}')^{-1} \\
\Phi' &= (\xi, 0, 0)
\end{aligned}
\tag{2.18}
$$

where

$\mathbf{q}'$ ...   is the quaternion of rotation between frames XYZ and $X'Y'Z'$, and

Φ' ...   is the rotation vector around axis X.

After this rotation, axis Y' is in the horizontal plane (assuming angle η is small!). To rotate X' axis to the horizontal plane, the second rotation around axis Y' (**C** on
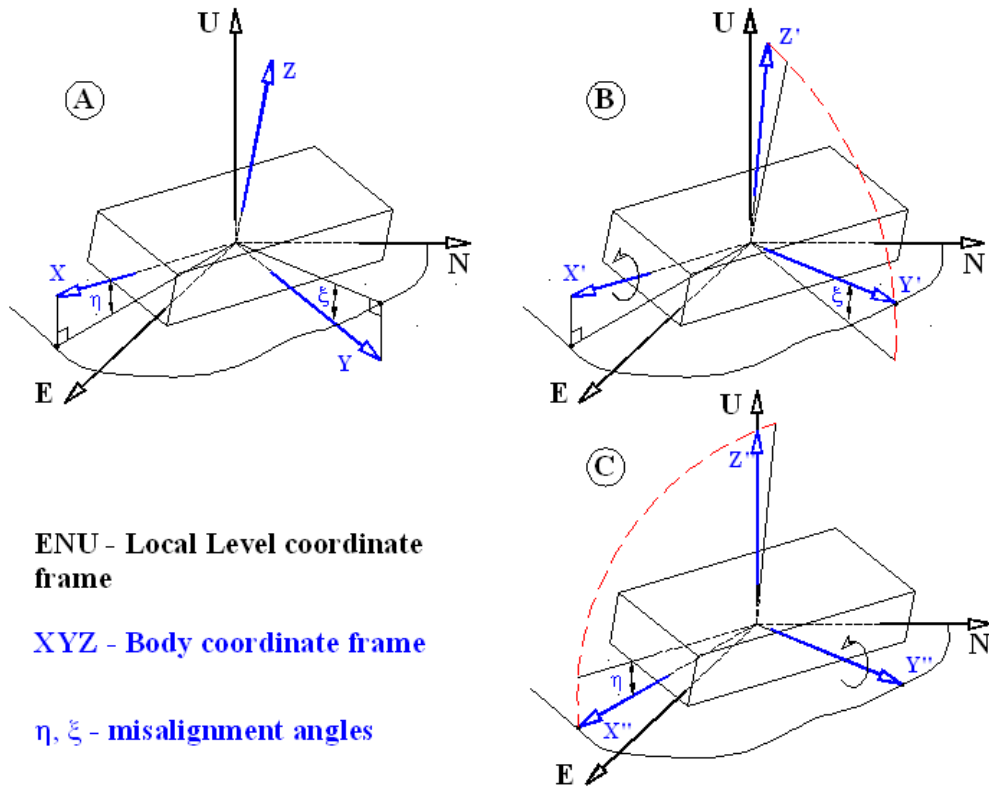
Figure 2.6: Principle of MEMS Inertial System Alignment

Figure 2.6) is performed according to

$$[0, x_{X"Y"Z"}] = \mathbf{q"} \otimes [0, x_{X'Y'Z'}] \otimes (\mathbf{q"})^{-1}$$
$$\Phi" = (0, -\eta, 0) \qquad (2.19)$$

where

$\mathbf{q"}$ ... is the quaternion of rotation between frames $X'Y'Z'$ and $X"Y"Z"$, and

$\Phi"$ ... is the rotation vector around axis X.

These two rotations can be simplified as one, with only one quaternion. The one

quaternion is the result of the quaternion multiplication as shown in Equation 2.20.

$$\mathbf{q} = \mathbf{q}'' \otimes \mathbf{q}' \tag{2.20}$$

There is still one parameter required to fully represent the orientation of the body frame with respect to an LL ENU frame. This parameter is the unknown azimuth angle, which is the angle between $\mathbf{X}''$ and $\mathbf{E}$ or $\mathbf{Y}''$ and $\mathbf{N}$ axes in Figure 2.6. The process of aligning the system in the horizon is called an azimuth alignment; it requires knowledge of this angle, i.e. the azimuth. In PDR mechanization, the user has to rely on GPS to obtain the azimuth. The methods of azimuth initialization, and the associated problems with the heading determination in the proposed system, are described in Chapter 5.

Chapter 3

Overview of Estimation and Reliability Theories

This chapter contains an overview of the elements in the estimation and reliability theories relevant to this research. The stochastic processes that will be used in this thesis are introduced, followed by a presentation of basic and more advanced topics on Kalman filtering, such as filter linearization for non-linear systems. Principles of statistical testing and the elements of reliability theory are then covered.

3.1 Estimation Theory

Essentially, in all engineering systems measurements or signals are contaminated by noise. The magnitude of this noise, its frequency spectrum and correlation properties vary for different cases, but one thing never changes: the noise is undesirable. The purpose of any estimation technique is essentially to estimate the effects of that undesirable noise on system parameters as accurately as possible considering the system and noise properties. In some estimation methods, the variables that are estimated are the system state errors; in other methods, the estimated variables are system states themselves. In both cases, the goal of the estimation procedure is to estimate the possible influence of noise on the system's performance while properly assessing the accuracy of the estimated output.

Most of the time, we deal with errors that are random in nature. Such random errors are analyzed and taken into account in various estimation methods by using stochastic processes and stochastic parameters to represent them. The most commonly used

stochastic models to represent errors, especially in the area of navigation, are *white noise sequences, Gaussian white noise sequences, random walk* and *1ˢᵗ order Gauss-Markov processes*. All these processes are well described in detail in Brown and Hwang (1992). In this section, an overview of these processes is provided because they will be used in applied filtering of the proposed integrated system.

A white noise sequence is defined as a set of uncorrelated, zero-mean values. The power spectral density of this sequence is constant over the whole frequency spectrum. Thus, a true white noise sequence contains infinite power, which is non-realizable in practice. A more common variation of a white noise sequence is the Gaussian white noise sequence. The random values of this random sequence are normally distributed. This is also a physically non-realizable random process since it contains infinite power. These models are commonly used to describe band-limited noise sequences (that exist in reality) due to their simple mathematical handling in estimation techniques when compared to the band-limited processes.

The other two processes, the random walk and the Gauss-Markov processes, are also extensively used in modeling errors in the Kalman filtering. From the perspective of the application of the discrete Kalman filter in this thesis, a discrete interpretation of those processes is given. Continuous counterparts are analogously derived. The discrete random walk process is analogous to a variable that is computed as the distance a user has walked along one line from the origin, making every step forward or backward at random. Mathematically, such process can be represented as

$$X(t_{k+1}) = X(t_k) + W(t_k) \tag{3.1}$$

where

$W(t_k)$ ⋯ is the uncorrelated zero-mean Gaussian sequence.

Every next epoch, the random walk sequence is equal to the previous epoch value with added Gaussian noise. In other words, it can be seen as a process that is the result of white noise integration. Another stochastic process that is somewhat similar to the random walk process is a 1st order Gauss-Markov process. Here, the current value of the process is correlated with the previous epoch value only to some extent, specified by a degree of correlation β. Mathematically, this process can be written as

$$X\left(t_{k+1}\right) = e^{-\beta \Delta t} \cdot X\left(t_k\right) + W\left(t_k\right) \tag{3.2}$$

where

$1/\beta$ ...   is the time constant of the process, and

$W\left(t_k\right)$ ...   is the uncorrelated zero-mean Gaussian sequence.

The Gauss-Markov process has an exponential autocorrelation function, which means that the values of the Gauss-Markov sequence are less correlated the further apart in time they are. The random walk and the Gauss-Markov processes are important in describing error behaviour in the inertial navigation systems and sensors. The accelerometer and gyro biases are frequently modeled by either random walk or Gauss-Markov process. As will be shown in Chapter 5, they are also useful in describing errors in pedestrian dead reckoning systems.

The Kalman filter has been an increasingly popular estimation tool for the navigation community after the famous paper by Rudolf Kalman (Kalman, 1960). In general, the Kalman filter is a technique that allows estimation of the quantity of interest provided that we have some knowledge of its dynamic behaviour and some measurements containing information about this quantity. The essence of the Kalman filter lies in its formulation, where the measurements and the model prediction are weighted to produce an estimate with a minimum quadratic mean error. This esti-

mate is based on the stochastic assumptions of process and measurement noises. In the following section, Kalman filter engineering topics are presented. A very detailed overview of Kalman filtering can be found in Gelb (1974); Brown and Hwang (1992).

3.1.1 Discrete Kalman Filtering

In order to apply the Kalman filter, a state-space model of the system has to be developed. If a vector of unknown parameters is denoted as $\mathbf{x}$, then either a continuous differential or a discrete difference model needs to be developed, as shown by

$$\dot{\mathbf{x}} = \mathbf{F} \cdot \mathbf{x} \tag{3.3}$$

$$\mathbf{x}_{k+1} = \mathbf{\Phi} \cdot \mathbf{x}_k \tag{3.4}$$

where

$\mathbf{F}$ ... is the dynamics matrix for the continuous model, and

$\mathbf{\Phi}$ ... is the state transition matrix for the discrete model.

The state transition matrix of the discrete system can be evaluated numerically from the dynamics matrix of the continuous model. Assuming that this matrix, $\mathbf{F}$, is constant over the (t_k, t_{k+1}) period of time, the state transition matrix can be computed according to (Gelb, 1974)

$$\mathbf{\Phi}_k = e^{\mathbf{F}\Delta t} = \mathbf{I} + \mathbf{F}\Delta t + \frac{(\mathbf{F}\Delta t)^2}{2!} + \cdots \tag{3.5}$$

where

Δt ... is the filter step time.

The system of Equations 3.5 describe the dynamics of the system itself or the evolution of the system states. In order to estimate the errors of the system, some

measurements are required. These measurements may be directly equivalent to the system states or may be functionally dependent on the system states through linear (or nonlinear) relationships. Thus, we can write the discrete system model and the discrete process measurements equations as

$$\mathbf{x}_{k+1} = \mathbf{\Phi}_k \mathbf{x}_k + \mathbf{w}_k \tag{3.6}$$

$$\mathbf{z}_k = \mathbf{H}_k \mathbf{x}_k + \mathbf{v}_k \tag{3.7}$$

where

$\mathbf{x}_k$ ... is the process state vector at time t_k with dimension $(n \times 1)$, and

$\mathbf{w}_k$ ... is the process white noise vector with dimension $(n \times 1)$ and with known covariance, and

$\mathbf{z}_k$ ... measurements vector with dimension $(m \times 1)$, and

$\mathbf{H}_k$ ... design matrix linearly connecting measurements to the system states with dimension $(m \times n)$, and

$\mathbf{v}_k$ ... measurement error vector with dimension $(m \times 1)$ and with known covariance.

In the derivation of the traditional Kalman filter equations for the above model, one important assumption needs to be made. It is assumed that the noise sequences $\mathbf{w}_k$ and $\mathbf{v}_k$ are uncorrelated with respect to each other.

The Kalman filter is divided into two parts. The first stage predicts the propagation of the model states forward in time. The other stage updates the propagated estimates with the available measurements. The prediction stage of the model state vector is taken from the dynamic model and can be written as

$$\hat{\mathbf{x}}_{k+1}^- = \mathbf{\Phi}_k \hat{\mathbf{x}}_k \tag{3.8}$$

The error covariance matrix associated with the prediction stage of the filtering can

be written as

$$\mathbf{P}_{k+1}^- = E\left[\mathbf{e}_{k+1}^- \mathbf{e}_{k+1}^{-T}\right] = \mathbf{\Phi}_k \mathbf{P}_k \mathbf{\Phi}_k^T + \mathbf{Q}_k \tag{3.9}$$

where

$\mathbf{P}_k$ ...   is the error covariance matrix at epoch k.

$\mathbf{Q}_k$ ...   is the covariance matrix of the process noise.

It can be seen from Equation 3.9 that if the filter only runs in prediction mode, the covariance of the prediction errors can only grow. This is logical since if there are no measurements or updates available, the errors keep accumulating. Once the measurement is available, the updated estimate of the system state vector is performed according to

$$\hat{\mathbf{x}}_{k+1}^+ = \hat{\mathbf{x}}_{k+1}^- + \mathbf{K}_{k+1}\left(\mathbf{z}_{k+1} - \mathbf{H}_{k+1}\hat{\mathbf{x}}_{k+1}^-\right) \tag{3.10}$$

where

$\mathbf{K}_{k+1}$ ...   is Kalman gain matrix at epoch $(k+1)$.

The Kalman gain matrix weights the measurements and system predictions to produce minimum mean-square error estimates of the states. These are based on the assumed noise properties of model and measurement noise. The Kalman gain matrix is computed according to

$$\mathbf{K}_{k+1} = \mathbf{P}_{k+1}^- \mathbf{H}_{k+1}^T \left(\mathbf{H}_{k+1}\mathbf{P}_{k+1}^- \mathbf{H}_{k+1}^T + \mathbf{R}_{k+1}\right)^{-1} \tag{3.11}$$

The last step in the discrete Kalman filter is an update of the error covariance matrix, $\mathbf{P}_{k+1}^+$, after the measurement update. This step is done according to

$$\mathbf{P}_{k+1} = \left(\mathbf{I} - \mathbf{K}_{k+1}\mathbf{H}_{k+1}\right)\mathbf{P}_{k+1}^- \tag{3.12}$$

One of the rather complicated steps in Kalman filtering is the proper calculation of the process noise matrix $\mathbf{Q}$. Formally, the process noise matrix can be computed from the state transition matrix $\mathbf{\Phi}$ and the specified driving noise sequence covariances as

$$
\begin{aligned}
\mathbf{Q}_k \quad &= E\left[\mathbf{w}_k\mathbf{w}_k^T\right] \\
&= \int_{t_k}^{t_{k+1}} \int_{t_k}^{t_{k+1}} \mathbf{\Phi}\left(t_{k+1}, \xi\right) \mathbf{G}\left(\xi\right) E\left[\mathbf{u}\left(\xi\right)\mathbf{u}^T\left(\eta\right)\right]\mathbf{G}^T\left(\eta\right) \cdot \mathbf{\Phi}^T\left(t_{k+1}, \eta\right) d\xi d\eta
\end{aligned}
\tag{3.13}
$$

where

$\mathbf{G}$ $\ldots$ is the matrix relating the white noise sequences to the model states.

Even for relatively basic models, the calculation of the $\mathbf{Q}$ matrix using Equation 3.13 is not that straightforward. However, several methods exist that simplify the solution of this equation (Brown and Hwang, 1992). The calculation of this matrix becomes even simpler in the case of a time-invariant system (Brown and Hwang, 1992). To calculate the process noise matrix, an intermediate matrix A needs to be computed as

$$
\mathbf{A} = \begin{bmatrix} -\mathbf{F}\Delta t & \mathbf{G}\mathbf{W}\mathbf{G}^T\Delta t \\ 0 & \mathbf{F}^T\Delta t \end{bmatrix}
\tag{3.14}
$$

The state transition and process noise matrices can be computed from the upper-right and the lower-right partitions of the matrix $\mathbf{B}$ using

$$
\mathbf{B} = e^{\mathbf{A}} = \begin{bmatrix} \cdots & \mathbf{\Phi}^{-1}\mathbf{Q}_k \\ 0 & \mathbf{\Phi}^T \end{bmatrix}
\tag{3.15}
$$

In the discrete system, measurements are available at discrete times. In the proposed PDR/HSGPS system, the measurement updates are the GPS measurements with (ideally) 1 Hz updating rate. The matrix $\mathbf{R}$ is thus discrete by default and is usually assigned as the variances of the GPS measurements used in the filter updating obtained after the LSQ adjustment procedure.

An important issue in the Kalman filter design is filter convergence. The convergence of the filter implies that the Kalman gain for a particular state reaches a steady state value after a number of iterations. The Kalman gain will converge to a steady-state position if the $\mathbf{Q}$ and $\mathbf{R}$ matrices are time-invariant. In the HSGPS data, $\mathbf{R}$ is constantly being changed due to either a better or worse GPS solution. In this case, the convergence of the Kalman filter is very problematic, especially for pedestrian navigation in signal degraded environments (Mezentsev et al., 2004).

3.1.2 Linearized Kalman Filter

If the model of the random process or the relationship between the measurements and the system states are nonlinear, the linearized discrete Kalman filter can be used instead (Brown and Hwang, 1992). In this case, the filter equations are linearized around the *nominal* trajectory, that is around the state vector values predicted by some means. The linearized equation for the filter states is given by

$$\mathbf{x}(t) = \mathbf{x}^*(t) + \Delta\mathbf{x}(t) \tag{3.16}$$

where

$\mathbf{x}^*(t)$ ... is the approximate trajectory (approximates the state vector), and

$\Delta\mathbf{x}(t)$ ... is the deviation of the actual trajectory from the linearized values.

After a Taylor's series expansion of the non-linear transition and design matrices, the system dynamics and measurement updating equations can be written as

$$
\begin{aligned}
\dot{\mathbf{x}}^* + \Delta\dot{\mathbf{x}} &\approx \mathbf{F}(\mathbf{x}^*, t) + \left[\frac{\partial\mathbf{F}}{\partial\mathbf{x}}\right]_{\mathbf{x}=\mathbf{x}^*} \cdot \Delta\mathbf{x} + \mathbf{w}(t) \\
\mathbf{z} &\approx \mathbf{H}(\mathbf{x}^*, t) + \left[\frac{\partial\mathbf{H}}{\partial\mathbf{x}}\right]_{\mathbf{x}=\mathbf{x}^*} \cdot \Delta\mathbf{x} + \mathbf{v}(t)
\end{aligned}
\tag{3.17}
$$

Linearized dynamics and design matrices can be computed by considering only the first order terms of the Taylor's series expansion and can be written as

$$\frac{\partial \mathbf{F}_{[\mathbf{n} \times \mathbf{n}]}}{\partial \mathbf{x}} = \begin{bmatrix} \frac{\partial \mathbf{F}_1}{\partial \mathbf{x}_1} & \cdots & \frac{\partial \mathbf{F}_1}{\partial \mathbf{x}_n} \\ \cdots\cdots\cdots\cdots \\ \frac{\partial \mathbf{F}_n}{\partial \mathbf{x}_1} & \cdots & \frac{\partial \mathbf{F}_n}{\partial \mathbf{x}_n} \end{bmatrix} ; \qquad \frac{\partial \mathbf{H}_{[\mathbf{m} \times \mathbf{n}]}}{\partial \mathbf{x}} = \begin{bmatrix} \frac{\partial \mathbf{H}_1}{\partial \mathbf{x}_1} & \cdots & \frac{\partial \mathbf{H}_1}{\partial \mathbf{x}_n} \\ \cdots\cdots\cdots\cdots \\ \frac{\partial \mathbf{H}_m}{\partial \mathbf{x}_1} & \cdots & \frac{\partial \mathbf{H}_m}{\partial \mathbf{x}_n} \end{bmatrix} \qquad (3.18)$$

where

n ... is the length of the state vector, and

m ... is the length of the measurement vector.

Since the approximate values of the state vector are obtained with the sensor measurements, the Kalman filter procedure is applied to estimate the difference between the true trajectory and the approximated one. The formulation of the filter equations can be written as

$$\begin{aligned} \Delta \dot{\mathbf{x}} &= \left[\frac{\partial \mathbf{F}}{\partial \mathbf{x}}\right]_{\mathbf{x}=\mathbf{x}^*} \cdot \Delta \mathbf{x} + \mathbf{w}\left(t\right) \\ \left[\mathbf{z} - \mathbf{H}\left(\mathbf{x}^*, t\right)\right] &= \left[\frac{\partial \mathbf{H}}{\partial \mathbf{x}}\right]_{\mathbf{x}=\mathbf{x}^*} \cdot \Delta \mathbf{x} + \mathbf{v}\left(t\right) \end{aligned} \qquad (3.19)$$

After this linearization procedure, linear discrete Kalman filter equations can be applied to estimate the deviation of the state vector from the actual trajectory, $\Delta \hat{\mathbf{x}}$. As will be discussed in Chapter 7, the Kalman filter developed for the PDR/HSGPS system will have a non-linearity only in the dynamic model, that is in $\mathbf{F}$. The measurement equation will be linear.

The extended Kalman filter is another tool that makes it possible to apply a Kalman filter to non-linear discrete systems. The extended Kalman filter is similar to the linearized Kalman filter, but in this case, a linearization takes place in relation to the filter's estimated trajectory and not the filter's predicted trajectory (ibid). The

methodology and development of the Kalman filter for this research will be covered in Chapter 7, where it will be shown that PDR sensor measurements are used to propagate the trajectory forward (prediction mode), and GPS measurements are used to update the trajectory. The HSGPS measurements in a city downtown are of poor quality, which may lead to actual degradation of the estimated trajectory after the measurements become available. This means that the estimated trajectory might be worse than that the propagated after the filter prediction. The applicability of the extended Kalman filter may lead to an eventual divergence of the filter (ibid). This means that the linearized Kalman filter is preferable for use in such signal-degraded environments over the extended Kalman filter.

3.1.3   Observability Analysis

One of the important issues in Kalman filter engineering is the analysis of the system observability. The purpose of the observability analysis is to determine whether the system states can theoretically be observed with the available set of measurements. In Kalman filter design, it is often impossible to measure all the states included in the system model. The observations or the measurements are functionally related to the filter states either through linear or non-linear relationships. The observability can be analyzed through a so-called *observability* matrix. The observability matrix for the discrete system case can be computed according to (Gelb, 1974)

$$\mathcal{O} = \begin{bmatrix} \mathbf{H}^T & \mathbf{\Phi}^T \mathbf{H}^T & (\mathbf{\Phi})^2 \mathbf{H}^T & \cdots & (\mathbf{\Phi})^{n-1} \mathbf{H}^T \end{bmatrix} \tag{3.20}$$

The system is declared as observable if the observability matrix has a full rank if

$$\text{rank}\,(\mathcal{O}) = n \tag{3.21}$$

If a certain system state is unobservable, then the error covariance matrix of the filter estimates, $\mathbf{P}$, usually tends to increase without limits. Thus, it is very important to

properly design the system equations so all the states of the filter will be observable with the available measurements.

To demonstrate the principle of observability, let us consider a simple example. A similar problem will arise in the development of the Kalman filter for the PDR system so it is well worth considering. Suppose the system model consists of two states: one is the user heading and the other is the rate of heading change. Also, let us suppose we can have either a measurement of heading or a measurement of the heading rate but not both. The transition matrix and the design matrices for these cases is obtained by

$$\mathbf{\Phi} = \begin{bmatrix} 1 & 1 \\ 0 & 1 \end{bmatrix}; \quad \mathbf{H}_H = \begin{bmatrix} 1 & 0 \end{bmatrix}; \quad \mathbf{H}_{HR} = \begin{bmatrix} 0 & 1 \end{bmatrix}; \quad (3.22)$$

where

$\mathbf{H}_H$ ... is the design matrix if the heading variable is measured, and

$\mathbf{H}_{HR}$ ... is the design matrix if the heading rate is measured.

The observability matrices can be calculated according to Equation 3.20. The rank of the matrices is computed as

$$\text{rank}\,(\mathcal{O}_H) = 2; \quad \text{rank}\,(\mathcal{O}_{HR}) = 1; \quad (3.23)$$

where

$\mathcal{O}_H$ ... is the observability matrix in case of heading measurement, and

$\mathcal{O}_{HR}$ ... is the observability matrix in case of the heading rate measurement.

It is easy to see that in the case of the heading rate measurement, the observability matrix is rank deficient. In this case, the heading error is not directly observable.

The error that accumulates in heading can grow infinitely large. The above case of the system with the heading rate measurement can be called a poor design and should be avoided.

3.2   Statistical Testing and Reliability

The science of statistical testing can be seen as a statistical gamble. In most cases, assumptions have to be made about whether a set of measurements belongs to a certain distribution, usually a normal distribution. Let us assume that a certain measured parameter belongs to a normal distribution with parameters $N \sim (0, \sigma^2)$. That implies that 67 of the measurements will lie in $[-\sigma; +\sigma]$ region. What can be said about a measurement with a value of, say, 10σ? There is a slight chance that this measurement also belongs to this distribution. This probability is very small, but it is larger than 0. From a practical perspective, we simply do not know for sure whether it belongs to the assumed distribution or not, so we have to make a decision.

In engineering statistics, in order to deal with such situations a *significance level* parameter is introduced. Let us consider the situation shown in Figure 3.1. Suppose we assume that the measurements follow a certain distribution shown in this figure in blue (this distribution may not be normal and may not necessarily with zero mean). Then, we propose that every measurement that falls beyond the line of significance level belongs to a different distribution. There is a very small possibility that this measurement can still belong to our known distribution. In this case, we will commit a so-called **Type I** error; that is, we will find a significant difference when there is none. In statistical testing, therefore, we wish to set the value α as small as possible (shown in Figure 3.1 for one tailed distribution).

When we do so, there is a chance that a measurement that does not belong to our

distribution will "slip" through our testing procedure as the one that belongs to our given, known distribution. Suppose a certain measurement belongs to an unknown distribution shown in the figure in red. The higher we set our limit for the Type I error, α, the more our known distribution crosses with the unknown distribution. If the measurement belongs to unknown distribution and falls into the β region on the figure, then it would be considered as the one that belongs to our known distribution. That means we will treat the measurement as a good one, that is, the one that belongs to the distribution we are testing the measurements against. In this case, we have committed a **Type II** error, which means that we have not found a difference when there was one. One would obviously wish to make this value of β as small as possible.
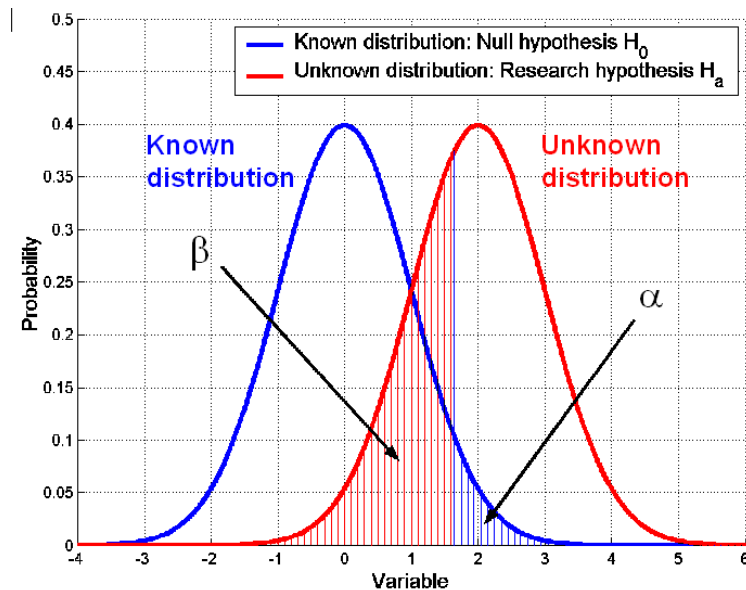
Figure 3.1: The Risk of a Type I or Type II Error

The problem is that in practice we cannot minimize both parameters, α and β, which are dependent on the non-centrality parameter of the unknown distribution. This is

the third parameter that alone with α and β completes the set of parameters required to set the statistical testing procedure.

This statistical testing is called hypothesis testing. By a hypothesis, a certain statement is implied; for example, if a measurement is said to belong to a known distribution, then the null hypothesis, H_0, is said to be accepted. If it is concluded that the measurement belongs to a different distribution, that is when a significant difference is found, and it is said that the alternative, or research, hypothesis, H_a, is accepted.

It should be clearly noted what is meant by "acceptance of a hypothesis". The acceptance of a hypothesis means that during statistical testing, no significant difference was found that could motivate us to reject the hypothesis (Hinton, 2004). Some authors argue that it should be said that "we have failed to reject the null hypothesis" rather than "the hypothesis is accepted" if no significant difference is found (Cohen, 1988).

This briefly described hypothesis testing methodology is the basis for the reliability theory applied to GPS. The statistical analysis in GPS is not that straightforward because the GPS observables cannot be directly subjected to such testing. The pseudoranges must first be involved in an LSQ computation of the position and user clock bias. The statistical testing method in GPS is called Receiver Autonomous Integrity Monitoring (RAIM) and is discussed in the following section.

3.2.1 RAIM Algorithm

In GPS, the position solution is calculated through a least squares or Kalman filter procedure. In this algorithm we wish to use only reliable measurements. In other words, we wish to test whether the measurements contain an outlier or a blunder. If so, it is obviously desired to detect such an outlier and remove it from the solution.

The directly measured pseudoranges cannot be subjected to any statistical testing because the user position and the clock biases are known. In statistical testing words, the true (or assumed to be true) distribution is not known. First, a LSQ solution must be obtained.

The statistical testing for the LSQ procedure was first developed by Baarda (1968) for the geodetic network adjustment problem and is called reliability theory. It was then adopted for satellite navigation, especially for precise navigation applications, such as aviation. A detailed overview of reliability theory can also be found in Leick (1995). In this section, a brief overview of the reliability theory that will be applied to HSGPS data is given.

The linearized pseudorange measurement equations in the least-squares epoch-by-epoch procedure can be expressed as

$$\Delta\rho = H\Delta\hat{x} + \varepsilon \tag{3.24}$$

where

$\Delta\rho$ . . . is the misclosure vector, that is the difference between the predicted and measured pseudorange measurements, and

ε . . . is the vector containing pseudorange measurement errors assumed to be normally distributed with zero-mean, and

H . . . the design matrix, and

$\Delta\hat{x}$ . . . incremental coordinate component from the linearization point.

If redundant observations have been made, least-squares residuals of pseudorange measurements can be obtained from the least-squares estimation as (Wieser, 2001; Ryan, 2002)

$$\hat{r} = H\Delta\hat{x} - \Delta\rho \tag{3.25}$$

The resulting residual vector, $\hat{r}$, can be used to test internal consistency among the pseudorange measurements (Kuang, 1996). The residuals can be standardized/studentized (Ryan, 2002; Kelly, 1988) according to

$$w_i = \left| \frac{\hat{r}_i}{\sqrt{(C_{\hat{r}})_{ii}}} \right| \quad , \quad i = 1 : n \tag{3.26}$$

where

n ...   is the number of observations, and

$C_{\hat{r}}$ ...   is the covariance matrix of the residuals.

The covariance matrix of the residuals, $C_{\hat{r}}$, can be calculated according to

$$C_{\hat{r}} = C_l - H \left(H^T C_l^{-1} H \right)^{-1} H^T \tag{3.27}$$

Reliability theory is usually classified as internal and external reliability. Internal reliability refers to the procedure of detecting an inconsistent measurement among the measurements. This is analogous to the example discussed in Section 3.2. External reliability deals with the matter of assessing what effect a Type II error, that is the one that passed undetected, can cause in the final result. In internal reliability theory, the minimum error that can be detected assuming certain probability distributions, and values of α and β, is called the marginally detectable blunder (MDB). In this thesis, we will cover only topics related to internal reliability theory

To detect a measurement error in the position solution computation, least-squares range residuals must be statistically tested. Errors in the functional models in the solution computations are assumed Gaussian zero-mean in unbiased cases. Unfortunately, this assumption does not hold for HSGPS in degraded signal environments (Kuusniemi and Lachapelle, 2004). It will be shown in the Section 6.3 later in the thesis that reliability theory is not very successful when applied to HSGPS data.

To detect an inconsistent navigation situation, a so-called *global* test is performed. The global test consists of testing whether or not an 'a posteriori' variance factor, $\hat{\sigma}_0^2$, multiplied by the degrees of freedom $(n - p)$ is centrally χ-squared distributed with a significance level of α and $(n - p)$ degrees of freedom as (Kuang, 1996)

$$\hat{\sigma}_0^2 = \frac{\hat{r}^T C_l^{-1} \hat{r}}{n - p} \tag{3.28}$$

$$\hat{\sigma}_{0,threshold}^2 = \frac{\chi_{\alpha,(n-p)}^2}{n - p} \tag{3.29}$$

$$H_0 : \hat{\sigma}_0^2 < \hat{\sigma}_{0,threshold}^2 \quad \text{(integrity failure)} \tag{3.30}$$

$$H_a : \hat{\sigma}_0^2 \geq \hat{\sigma}_{0,threshold}^2 \quad \text{(no integrity failure)} \tag{3.31}$$

where

n ... is the number of satellites in view, and

p ... is the number of estimated parameters.

In case the global test fails, an attempt to correct the inconsistent position solution may be performed if there is enough redundancy. This procedure is referred to as a *local* test. Assuming that only one blunder exists at a time, to detect that blunder, each standardized residual w_i can be statistically tested with a fault-free hypothesis $H_{0,i}$ against an alternative hypothesis $H_{\alpha,i}$. The underlying assumption is that the standardized residuals are normally distributed (Baarda, 1968; Leick, 1995; Ryan, 2002) with zero expectation in the unbiased case (Kuang, 1996). Local testing of the standardized residuals against the normal distribution is conducted according to the conditions

$$H_{0,i} : w_i < n_{1-\frac{\alpha_0}{2}} \quad \text{(i acceptable)} \tag{3.32}$$

$$H_{\alpha,i} : w_i \geq n_{1-\frac{\alpha_0}{2}} \quad \text{(i erroneous)} \tag{3.33}$$

In the local test, the measurement with the largest standardized residual exceeding the threshold is regarded as an outlier and that measurement is excluded from the solution computation (Kelly, 1988; Teunissen, 1998). The kth observation is suspected to be erroneous when the following conditions are satisfied.

$$w_k \geq w_i \forall i \quad \wedge w_k > n_{1-\frac{\alpha_0}{2}} \tag{3.34}$$

As an approximation for a testing procedure to detect multiple observation errors using the local fault identification test, the single-fault local test may recursively be applied whenever a fault is detected. Thus, if an outlier is found and excluded, the test is repeated on the sub-sample remaining after deletion of the outlier (Hawkins, 1980; Petovello, 2003) assuming that there is enough redundancy to perform multiple exclusions. The identification and exclusion of measurements with the local test is performed sequentially until no more outliers are found in the navigation situation.

As was already briefly mentioned, the results of reliability analysis may not be that successful when applied to HSGPS data, and there are several reasons for this. The main one is that this theory is best suited for situations where we can assume only one blunder at a time. In the case of HSGPS, several observations in a single epoch may be outliers. In some extreme cases in downtown or indoor locations, all the measurements may essentially be more or less outliers whereby all the measurements in this case may have very substantial range measurement errors. This leads to another important parameter of reliability theory that is the breaking point of the method. The algorithm breaking point defines how many outliers may be present in a set of measurement that still allows us (theoretically) to detect and exclude them all. In the RAIM algorithm it is 50%, and it should be clear why. Let us assume we have 8 observations and 5 of them are outliers. For the sake of argument, let us assume that all of them are substantially biased in one direction, that is towards large positive biases. After applying a sequential RAIM algorithm (global and local tests), the

chances are that the 3 correct measurements will be removed since they represent the minority of the measurements in comparison to 5 blunderous measurements. Lacking other information, such as a previous epoch estimate or another source of navigation information (i.e. an inertial system), there is no theoretical way of distinguishing what is true from what is false in this case. This is the main reason why RAIM techniques frequently fail on HSGPS data.

Chapter 4

Integrated System Prototyping

This chapter describes the development of a prototype-integrated system for experimental testing. It then describes the mechanical design aspects taken into consideration, and provides the characteristics of MEMS sensors used in the system. In addition, the important issue of time synchronization of sensor data with GPS is discussed, and the method used in this work to synchronize the PDR data with GPS time is presented.

4.1 Sensor Unit Configuration

In the following chapters, the experimental data will be used numerous times in various aspects of the analysis. The development of the low-cost MEMS sensor based PDR system is first presented in this chapter.

Researchers imply different things when referring to low-cost sensor units. For some applications, a thousand dollar IMU is considered low-cost. For a pedestrian navigation application (with potential use in cell phones), a low-cost 6 degrees of freedom ISA should cost no more than tens of dollars. This very stringent price restriction limits one to MEMS sensors that are truly low-cost, at a price of several dollars or less in current or future mass production. Such a unit has been designed and assembled in this thesis to meet this requirement.

This assembled unit represents an Inertial Sensor Assembly (ISA). In such a configuration, the ISA outputs raw sensor data in analog form that is sampled by an

Analog-to-Digital (AD) converter. There are many mechanical, electric and engineering aspects in designing such an ISA. The objective of this thesis is not the development of the inertial system assembly with low-cost MEMS sensors. However, this chapter is included to demonstrate that an ISA made with only low-cost sensors has been designed, and to show that we have full control of the signals processing algorithm of the sensors data inside this ISA. Therefore, only the most important mechanical and electric design issues will be described, and the measures that were taken to address them in this design will be discussed.

The most important problems in the mechanical and electrical design of an ISA (or an IMU) that always have to be carefully addressed are perpendicularity of ISA sensitivity axes, vibration, temperature compensation, and supply power stabilization. These will be explored in the following paragraphs.

- **Perpendicularity of ISA Sensitivity Axes.** The sensitivity axes in a full 6 degrees of freedom ISA must be perpendicular to each other and form a right-angled triad. Traditionally (in both mechanical and strapdown systems), this is not achieved by only precise assembling, but also through a calibration procedure after the unit is assembled (Titterton and Weston, 1997). When MEMS sensors are used in the system, both the accurate assembling and the calibration requirements are hard to achieve and perform. First of all, the exact orientation of the MEMS sensors' sensitivity axes with respect to the sensor body is usually not known. Also, the MEMS sensors' bias drift rates will cause errors higher than slight axis misalignment in the system would cause. The system calibration techniques applied to a MEMS ISA would increase the price of the unit several times over. The sensors are mounted in a perpendicular triad as precisely as possible, with sub-degree accuracy with respect to the sensor cases. The accuracy of the sensors sensitivity axes orientation with respect to

the casing is normally within 1-2 degrees (www.analog.com). Therefore, it is expected that the achieved accuracy of perpendicularity of the sensitivity axes is around 1-2 degrees.

- **Vibration.** Vibration and associated resonance effects are some of the main concerns in mechanical system design. In such an ISA assembly, vibration is not crucially important, mostly because the system is meant to be used on the human body. For example, as compared to a vehicle, the human body does not generate the high frequency spectrum vibration that can affect sensor performance. In the assembled ISA, rigid mounting of the sensors on the perpendicular mounting planes is performed.

- **Temperature Compensation.** Temperature affects the entire spectrum of inertial devices, from hi-end to low-cost mechanical and strapdown systems. A successful solution to temperature problems almost always mean a successful inertial system product. Temperature plays an important role in the MEMS ISA as well. Preferably, the unit housing should be well isolated from the outside environment so that the temporal temperature variations and indoor/outdoor transitions minimally affect the unit. Algorithmic compensation is a whole separate study. Recent research results on temperature compensation of MEMS sensors can be found in Abdel-Hamid (2004). Such methods of temperature calibration of each and every sensor will also raise the price of such sensors. Without temperature calibration routines, a linear temperature model can be applied which is successful to some degree (Mezentsev et al., 2004). In this work, the temperature of the unit was stabilized by powering the unit for a substantial amount of time prior to the start of the test, and no temperature compensation routines were applied. This very much corresponds to linear temperature compensation models. In this way, the hardware part

of the system was simplified. However, in an operational system, temperature compensation routines must certainly be applied.

- **Supply Power Stabilization.** Most of the MEMS inertial sensors are ratiometric with respect to supplied power. This means that an error in the supplied voltage proportionally propagates into the sensor output signal. In MEMS inertial systems, voltage stabilization can be achieved fairly easily since such sensors consume minimal amounts of power. This design uses a high-quality voltage stabilizing circuit based on a TI TPS7250 voltage regulator microchip to stabilize the power supply. The voltage stabilizing circuit is essentially a heat emitter; therefore, this circuit is housed in a separate powering unit. In a commercial system design, this separation of heat-emitting elements, such as a power supply, from the sensing elements is always performed.

Conceptually, the ISA system structure is shown in Figure 4.1. Three MEMS accelerometers, three MEMS gyroscopes and a miniature pressure sensor are mounted on three perpendicular base plates. The perpendicularity of the plates is held within 1-2 degrees. The assembly case contains a tiny opening which allows the air pressure to change according to the environment for the correct pressure sensor operation. The sensor output and powering connections are made through an RS232 connector.

4.2   MEMS Sensors

In this section, descriptions of the MEMS sensors used in the system are given.
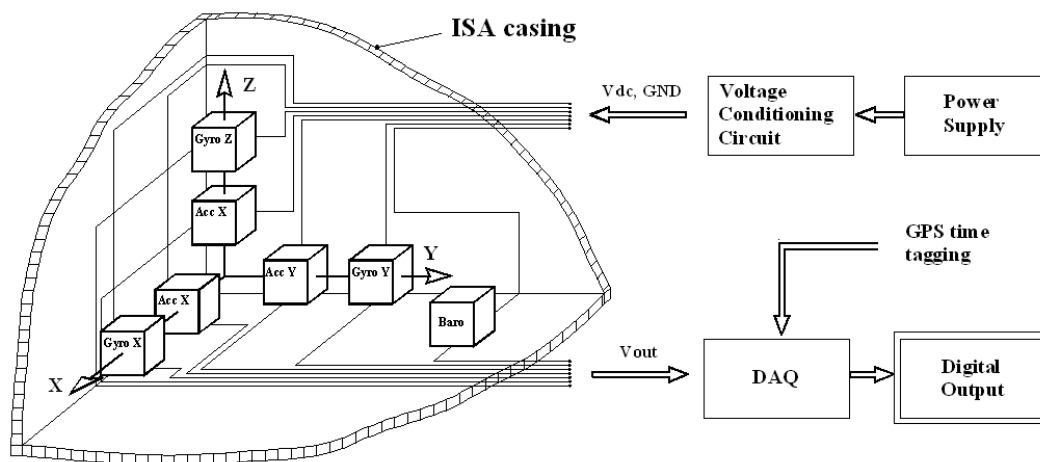
Figure 4.1: Inertial Sensor Assembly Layout

4.2.1 Analog Devices ADXRS150 MEMS Gyros

The analog Devices ADXRS150 gyro is a complete micro-machined rate sensor integrated with electronics on one chip. The dynamic range of this gyro is 150 degrees per second. However, the dynamic range of the gyros can be expanded tremendously, up to several thousand degrees per second, if the application requires it, by the appropriate selection of external resistors and capacitors (Weinberg, 2003). For pedestrian navigation application, the predefined bandwidth of 150 degrees per second is broad enough. This type of gyro is available in an ultra-small package size (7x7x3 mm) with a ball-grid array surface mounting and is shown in Figure 4.2 integrated onto an electric component board. The main operational characteristics of this gyro are given in Table 4.2.1.

Table 4.1: Main Operating Characteristics of Analog Devices ADXRS150 Gyros (www.analog.com)

Characteristic/Parameter	Value	Units
Dimensions	7x7x3	mm
Operating Temperature	$-55°\ldots+125°$	$°$C
Dynamic Range	±150	$°$/sec
Typical Supply Voltage	5.0	Vdc
Typical Supply Current	6.0	mAdc
Rate Noise Density at 25°C	0.05	$°/s/\sqrt{Hz}$
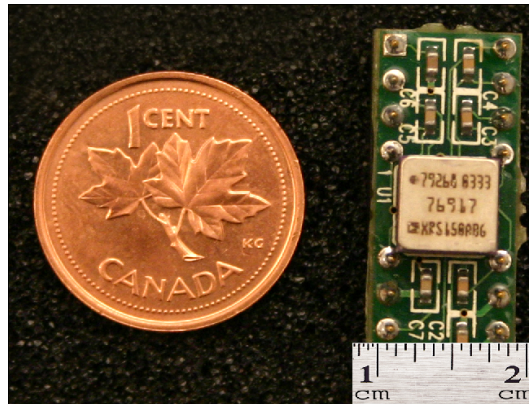
Figure 4.2: Analog Devices ADXRS150 Rate Gyro with Integrated Electronics

4.2.2   VTI SCA-600 Series MEMS Accelerometers

The MEMS accelerometers used in the system are low cost and miniature MEMS devices from VTI Technologies (Figure 4.3). These instruments offer excellent bias stability over temperature. Typical values for biases are in the order of several milli-g. The main operating parameters of the VTI SCA600-series accelerometers are given in Table 4.2.2.

Currently, the technology of accelerometers is far more advanced than the technology

Table 4.2: Main Operating Characteristics of VTI SCA600-C23H1G Accelerometers (www.vti.com)

Characteristic/Parameter	Value	Units
Dimensions	11x12x5	mm
Operating Temperature	$-40° \ldots + 125°$	°C
Dynamic Range	± 1.5	g
Typical Supply Voltage	5.0	Vdc
Typical Supply Current	< 4.0	mAdc
Zero Point Error for $-25° \ldots + 85°$C	± 80	mg
Sensitivity Error for $-25° \ldots + 85°$C	± 3	%

of MEMS gyro manufacturing. It is now possible to produce an accelerometer with a milli-g level bias and good bias stability in a volume equivalent to a state-of-the-art MEMS gyro. To precisely determine a bias in an MEMS accelerometer, testing in a precise leveling platform would be required. For the given application, these sensors exhibit good performance, on the level of several milli-g. From the manufacturer's data sheets, it can be assumed that the biases of these sensors do not exceed 5 milli-g when the temperature is fairly stable. Since these accelerometers will not be used in a classical mechanization scheme, but rather for leveling and detection of steps, this accuracy will give an alignment accuracy of less than 0.3 degrees. Such accuracy is sufficient considering the quality of the gyros that are used for the attitude computation.
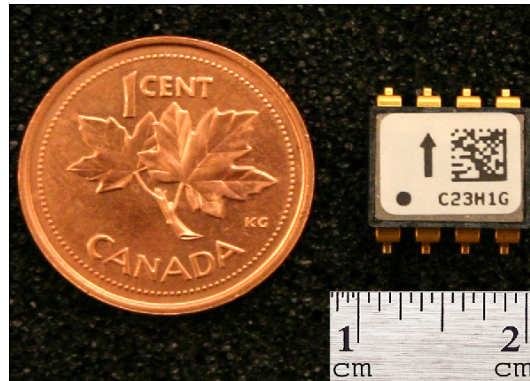
Figure 4.3: VTI SCA-610 Series Accelerometer

4.2.3 Motorola MPXA6115A Miniature Pressure Sensor

The low-cost miniature pressure sensor used in this system is the Motorola MPXA6115A. This type of pressure sensor measures the current raw barometric pressure, without converting it to altitude. This sensor is shown in Figure 4.4 and its main operating characteristics are given in Table 4.2.3. A brief overview of what this type of pressure sensor can provide for a navigation system is given; however, there is often a lot of confusion on this subject.
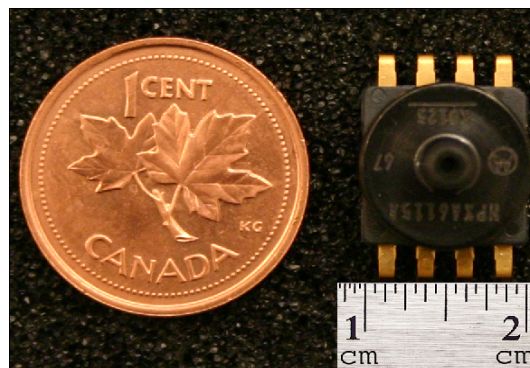
Figure 4.4: Motorola MPXA6115A Pressure Sensor

Table 4.3: Main Operating Characteristics of Motorola MPXA6115A Pressure Sensor

Characteristic/Parameter	Value	Units
Dimensions	11x11x13	mm
Operating Temperature	$-40° \dots +125°$	°C
Pressure Range	15...115	kPa
Typical Supply Voltage	5.0	Vdc
Typical Supply Current	6.0	mAdc
Max pressure error at 25°C	± 1.5	% of pressure

Firstly, the output of this sensor depends on many parameters. The two main factors attributing to error in the pressure sensor measurement are supply voltage instability and temperature drift. These issues can be dealt with in a somewhat similar manner as MEMS inertial sensors. Assuming normal values for the pressure, supply voltage and temperature errors, the pressure sensor error does not usually exceed 1 to 2 kPa.

Next is the conversion of the measured barometric pressure to altitude. To accomplish this, the current distribution of pressure with altitude must be known. Provided the user is mobile and has no links to some data aiding (such as AGPS), this problem can be difficult or impossible to deal with. An empirical model to convert the pressure to altitude assuming certain initial parameters, such as pressure at sea level and the certain distribution of pressure with altitude, must be used.

Several closed form and empirical (data-fitted) models that relate barometric pressure to altitude exist. The altitudes calculated using different models with the same value of the pressure normally vary by only a few centimetres. In this work, an empirically fitted model has been chosen for the altitude calculation. Assuming the standard atmosphere pressure at sea level is 101.325 kPa, and that there are normal barometric conditions, meaning that the distribution of the pressure versus altitude is known, altitude A can be found from the barometric pressure according

to (Webster, 1999)

$$A = 44332.3 - 4947.2 \cdot P^{0.190255} \tag{4.1}$$

where

P ... is the barometric pressure in *Pascals*, and

A ... is the altitude in *metres*.

Figure 4.5 (A) shows the level of error in absolute altitude estimation one can expect with a pressure sensor at Calgary altitudes (about 1100 metres above sea level) that is subject to a 1 kPa pressure error using Equation 4.1. In this case, a 1 kPa pressure error causes approximately a 100-metre error in the altitude estimate. The resolution of such sensors is usually good around 1-2 metres. Therefore, such sensors can be successfully used in differential mode. Once an altitude becomes known (either through GPS or other aiding means), a differential correction with respect to that height using such a pressure sensor can be applied. The results shown on Figure 4.5 (A) illustrate this point using real data. This plot shows the altitude computed from a pressure sensor during a pedestrian walking test on a horizontal street in downtown Calgary. As can be seen from this graph, apart from the large bias of about 180 metres, the resolution of the height provided by the sensor is quite good (2-5 metres). Also, the temporal pressure changes during the unit operation could easily be dealt with by the differential barometer system on one or several base stations in the area of interest. Such a system will also require that the user has access to differential correction data that can be received through AGPS, for example.
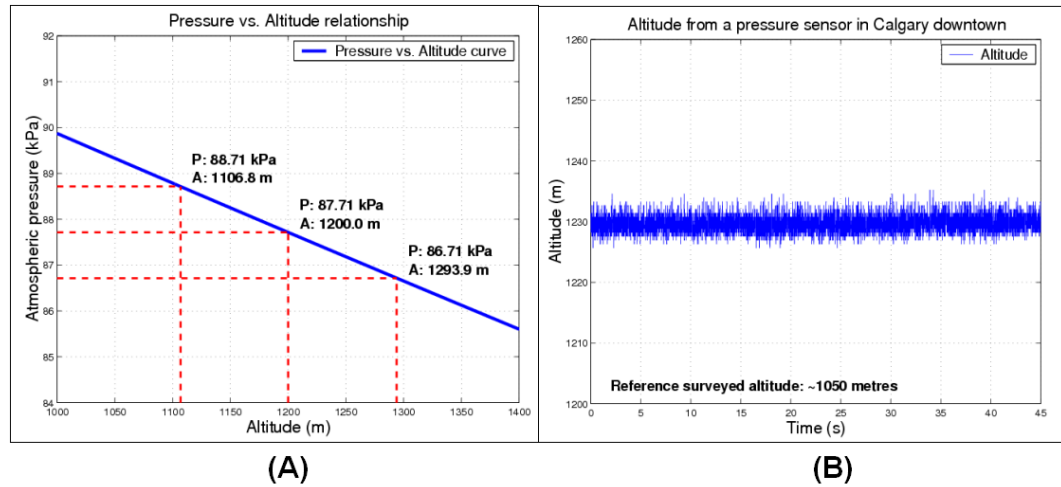
Figure 4.5: **A**: Atmospheric Pressure vs. Altitude Relationship: 1kPa error in pressure can cause around 100 metres of error in the absolute altitude estimate at Calgary altitudes; **B**: Altitude computed with the pressure sensor in Calgary downtown walking test. The surveyed reference altitude is approximately 1050 metres

4.3   SiRF HSGPS Receiver

The HSGPS receiver used in this work is a SiRF Xtrac HSGPS hardware receiver. The receiver uses longer dwell integration times than a standard sensitivity GPS receiver, especially in the acquisition mode. The exact dwell times are not known due to the proprietary structure of the receiver filter. The "Xtrac" stands for extended tracking capability compared to the previous HS GPS receiver Star II. The receiver used is the evaluation kit. It is based, though, on the rather small GPS chip that is, together with currently small RF front ends, well-suited for miniature mobile applications. Table 4.3 gives the main characteristics of the receiver.

Table 4.4:   Main Operating Characteristics of SiRF Xtrac HSGPS Receiver (www.sirf.com)

Characteristic/Parameter	Value
Tracking	L1, C/A code
Channels	12
Protocol	SiRF Binary, NMEA
Tracking Sensitivity	16 dB-Hz
Hot Start Sensitivity	23 dB-Hz
Cold Start Sensitivity	32 dB-Hz

4.4   Time Synchronization

Time synchronization of data is an important issue in any integrated system design. During data collection, the GPS and any other sensor data must be synchronized with accuracy that is sufficient for a given application.

The inertial system and GPS essentially provide two independent navigation solutions. If the data from the two systems at a certain time[1] have different time stamps, the integration results will be useless. The accuracy requirement of the time synchronization for a given application is essentially driven by the speed of the linear and angular motions of the object on which the system is installed. The faster and more maneuverable the object, the better the timing accuracy that must be achieved. Therefore, there are different requirements for time synchronization accuracy for aviation, vehicular or pedestrian navigation applications. For aviation GPS/INS integrated systems, where the speeds are reaching a thousand kilometres per hour, a tenth of a second error in timing between the two systems can cause tens of metres of relative positioning errors between the systems. For the pedestrian navigation application with speeds of 1-2 metres per second such a timing error will cause a centimetre level positioning error in the integrated solution. This magnitude

---

[1]absolute time reference is meant by word "time" here

of error is tolerable considering the individual accuracy of the PDR and HSGPS systems used.

Obviously, the better the time synchronization for any kind of application, the better the accuracy of the integrated system. Unfortunately, the more accurate the time synchronization required by the application, the more hardware and software resources are needed. When aiming for a low-cost solution, this is not always possible. This problem must be addressed on the level of integrated circuit design for the system together with the digital acquisition (DAQ) sampling solution.

In this work, because of research needs and the simultaneous need to sometimes mark certain locations[2] a rather unusual approach to time synchronization is taken. For this purpose a geodetic grade L1/L2 NovAtel OEM4 GPS receiver has been used. This receiver has the capability of recording a GPS time once a voltage input is provided to one of the receiver ports. The sensor data is sampled by a DAQ card. Parallel to all sensor data channels, a separate channel has been dedicated to a trigger that, once pressed, creates a voltage pulse. This trigger analog channel is sampled by the DAQ card as a separate channel which is parallel to all the sensor channels. Once the trigger is pressed, the GPS receiver generates the time-mark that corresponds to that pulse. The time-mark that the receiver records is based on the GPS time inside the receiver, if the receiver is tracking GPS satellites or is based on the receiver internal clock. Then, based on the pulses in the trigger channel and the associated time-marks, the sensor data are linearly interpolated.

There are many factors contributing to the accuracy of time synchronization with this method. Probably the most important one is the accuracy of the DAQ internal base clock. For the DAQ card used (National Instruments Al16XE-50, www.ni.com),

---

[2]In this context, 'to mark a location' means to write a GPS time of the event, such as the time when passing through a certain location or a landmark point

the base clock accuracy is better than 0.01 % (www.ni.com) assuming stable temperature. Assuming one time tagging per minute, the accuracy of time synchronization is expected to be better than 10 ms. If a pedestrian is walking at an average speed of 1.4 m/s, such a timing accuracy can cause an error equivalent to several centimetres at most, which is well below the accuracy required herein.

The system scheme, including a time tagging loop, is shown on Figure 4.6. The designed ISA unit is shown worn on the user's belt. The time tagging trigger is held in the hand, and time tagging is performed approximately every minute.
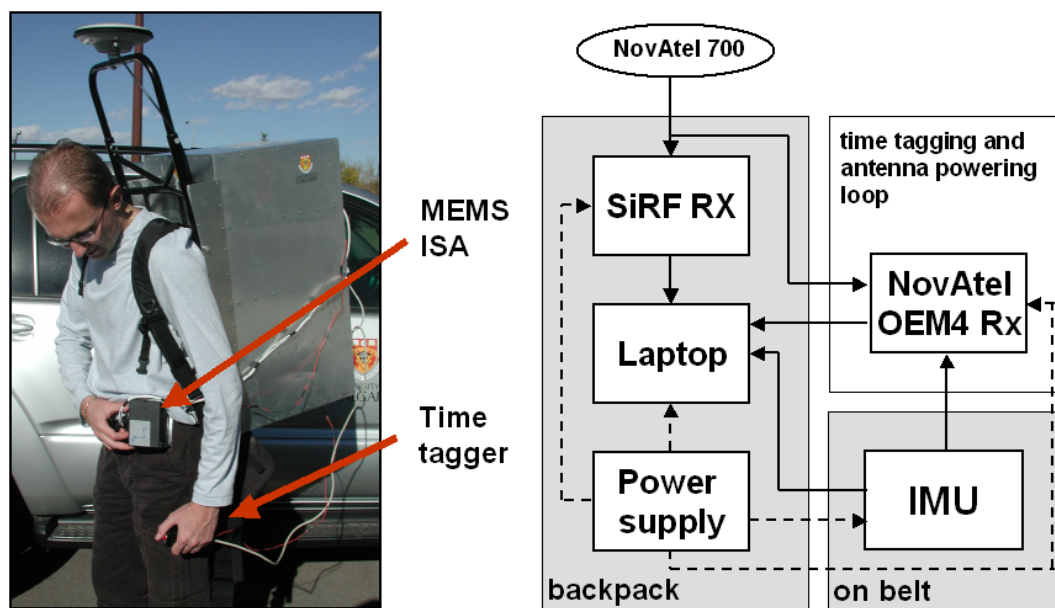
Figure 4.6: The ISA Unit of a Test Person and the System Scheme

4.5 MEMS ISA

The assembled MEMS ISA system developed herein is shown in Figure 4.7. The volume of the unit shown may seem quite bulky, but this is because of custom assembling. In industrial production, the volume of the unit from the same components can be brought down to several cubic centimetres. Due to the ball-grid array (BGA) mounting surface of the ADXRS150 gyros, they are first mounted on a separate board with electronics. Those boards are then fixed to the ISA mounting plates.
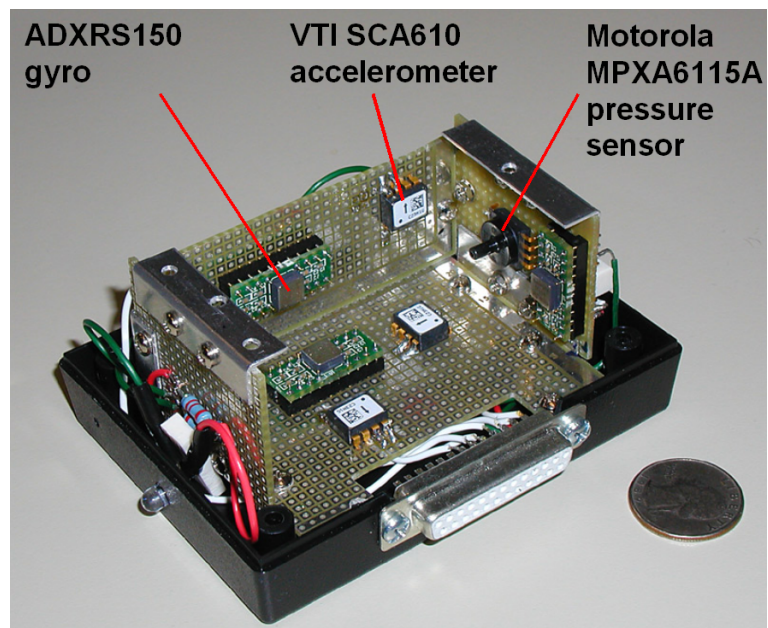
Figure 4.7: MEMS Inertial Sensor Assembly

The resulting ISA is light, at a total weight of about 100 grams. Even in this form-factor, the unit is easy to carry on a belt. The sampling rate of the data is 200 Hz and during the mechanization was decreased to 20, which is sufficient to include the frequencies in the signals induced by the walking of the user.

Chapter 5

Pedestrian Dead Reckoning

This chapter presents the pedestrian dead reckoning mechanization algorithm, followed by a discussion of methods of user step detection and heading determination. The next discussion considers stochastic error modeling of the major errors in the PDR. Finally, position accuracy measures for PDR systems are proposed.

5.1 Pedestrian Dead Reckoning Algorithm

In PDR mechanization, inertial sensors are used differently than in classical inertial mechanization techniques: PDR mechanization exploits the kinematics of human walking to its benefit. The main idea behind the PDR algorithm is the propagation of the user position with user steps rather than by the integration of acceleration (Levi and Judd, 1999).

The main idea of PDR mechanization is to use accelerometer signals to detect steps, estimate step length and propagate position using a measured heading. This mechanization requires that any possible means of transportation other than walking is excluded. The heading can be computed using gyroscopes or a levelled compass. Any magnetic compass will be subject to strong magnetic disturbances such as power lines and various metal/steel objects and structures. In a city's downtown (or anywhere indoors), such disturbances will only be amplified. Those disturbances that are of a sporadic time/space nature are hard to detect and are even harder to correct without external correction signals. Therefore, if accurate navigation in areas such as urban

canyons is required, the system has to rely on other means to get the heading. Even if low-cost MEMS gyros have substantial biases, they are not susceptible to such sporadic disturbances, making them preferable to magnetic compasses when GPS is available to provide an absolute heading.

Figure 5.1 shows a high-level outline of a PDR algorithm. In this figure, a PDR algorithm is divided into four steps. The first three steps of a PDR algorithm will be discussed in detail in the following sections of this chapter.
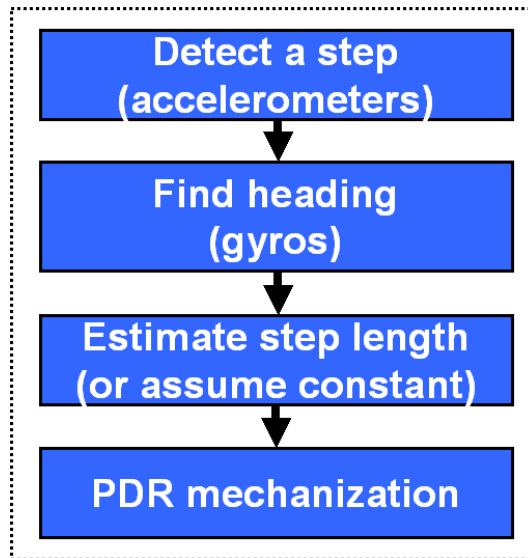
Figure 5.1: PDR Algorithm.

The PDR mechanization equations comprise the fourth step of this algorithm. These equations are rather straightforward and can be written as

$$
\begin{aligned}
\mathbf{E}_k &= \mathbf{E}_{k-1} + \hat{\mathbf{S}}_{(k-1,k)} \cdot \sin\left(\hat{\mathbf{H}}_{(k-1)}\right) \\
\mathbf{N}_k &= \mathbf{N}_{k-1} + \hat{\mathbf{S}}_{(k-1,k)} \cdot \cos\left(\hat{\mathbf{H}}_{(k-1)}\right)
\end{aligned}
\tag{5.1}
$$

where

$\mathbf{E}_k$ ...   is the Easting user coordinate at epoch k, and

$\mathbf{N}_k$ ...   is the Northing user coordinate at epoch k, and

$\hat{\mathbf{S}}_{(k-1,k)}$ ...   is the estimated user step length from epoch $k-1$ to epoch k, and

$\hat{\mathbf{H}}_{(k-1)}$ ...   is the estimated user step heading at epoch $k-1$.

This set of equations represents a 2D navigation scheme. The reason these PDR equations are always composed in a 2D frame is twofold. First, slight uphill or downhill user walking will cause a small horizontal error when the vertical component is not taken into account. Second, this horizontal error, which is caused by not considering the vertical component, can be projected equivalently onto step length error and can be addressed through step length error modeling. Fairly significant changes in user altitude (walking up or down the stairs, for example) can be detected by a low-cost pressure sensor that is part of the system, and the step length estimate can be adjusted accordingly (Lachapelle et al., 2003b).

5.2 User Step Detection

The first part of a PDR algorithm is the detection of user steps with accelerometers. As explained earlier in this thesis, the PDR system (in other words, the low-cost ISA) is attached to the user's belt, and the accelerometers show a specific acceleration pattern when the user is walking. In this case, detection of the step is not problematic because many robust and reliable methods exist. Some methods utilize an algorithm that detects when the acceleration value crosses a certain threshold. Once it is detected, a step made by a user is declared. Other algorithms take advantage of the sinusoidal-type pattern of the acceleration signal when a user is walking. In this case, the acceleration pattern is subjected to frequency analysis, such as FFT. When

walking, such FFT will show a strong frequency peak, usually in the range of 0.5 Hz to 2 Hz (2 or 0.5 steps per second walking frequency).

Figure 5.2 shows a typical acceleration pattern when a user is initially static and then starts walking with an ISA unit attached to the user's belt. In this work, the steps are detected when the acceleration pattern crosses the gravity value, e.g. $9.81 m/s^2$, and the previous step was detected δ seconds ago when the walking stage of the user was detected with FFT

$$\mathbf{S}_{t_k} \quad : \quad a_{t_k} > g \quad \& \quad a_{t_{k-1}} < g \quad \& \quad t(s_{i-1}) - t_k > \delta \tag{5.2}$$

where

$\mathbf{S}_{t_k}$ ... is the detected step at time t_k, and

a_{t_k} ... is the total 3D acceleration at time t_k at k^{th} sample, and

$a_{t_{k-1}}$ ... is the total 3D acceleration at time t_{k-1} at the $(k-1)^{th}$ sample, and

g ... is the local gravity, and

$t(s_{i-1})$ ... is the time of the previous detected step, s_{i-1}, and

δ ... is the time threshold between the detected steps. Depends on the user walking frequency and can adaptively be adjusted by FFT constantly being performed on the interval of the previous 2 to 3 detected user step.

There are two types of errors associated with a step detection algorithm: *step misdetection* and *fault step detection* (Ladetto, 2000). A step misdetection is declared when a step is made by a person but is not detected by the algorithm. A step is declared to be faultily detected when no step is performed, but a step is detected by the algorithm. The step misdetection causes the underestimation of the walking distance, and the fault step detection causes the overestimation of the steps performed, i.e., overestimation of the distance traveled by the user. With the described
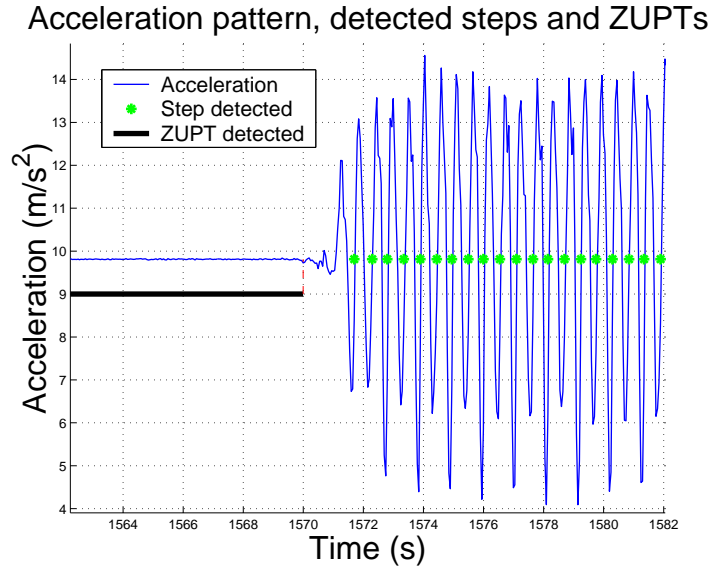
Figure 5.2: Detection of Steps using 3D Acceleration Pattern

algorithm and the PDR unit attached to the body, the rate of misdetection and fault step detection is normally below 2 %, which means that on average one in fifty steps is either not detected or a fault step is detected when a user is not walking.

A more complicated case of detection of user steps is when a PDR unit is in the user's hands, for example in a PDA or a cell-phone. In this case, the acceleration pattern is damped by user hands and the usual methods of step detection described above are not that robust and reliable anymore. This case refers to a more specific topic on the subject of pedestrian navigation called motion state detection. In this case, the unit may freely change orientation with respect to the user's body. In other words, the orientation of the unit body frame is not fixed with respect to the user's body. This introduces an uncertainty in the unit attitude determination which makes the heading bias between the unit body frame and the user body frame unobservable by means of GPS (Collin et al., 2002). Thereafter, it is assumed that the unit is

always attached to the user's belt (to the body, in general) and the detection of steps is performed using the algorithm discussed above. Also, it is assumed that the orientation of the unit does not change with respect to the user's body. The unit body frame thus represents the user body frame.

When a step is not detected, the user is not walking; in other words, he or she is static. For a person on foot, several classifications of a stop can be made:

- **A user is completely static:** The attitude of the IMU can be updated through a zero velocity update (ZUPT);

- **A user is not walking but is not completely static either:** In this case, the position of the user is not propagated, but the attitude must constantly be updated.

In practice, complete motionless stops of a pedestrian rarely happen. For example, compare a pedestrian to a case of vehicular navigation when a vehicle stop at a traffic light means a car is completely motionless. Most of the time the user is not walking, but s/he is not completely static either; for example, the user might be turning. In this case, a zero velocity update cannot be performed, and the attitude of the IMU must constantly be updated. Figure 5.3 shows a case when a user is not walking but is turning on the same spot (area marked as "A"). On the right of Figure 5.3, the attitude of the IMU during this period is shown. As can be seen, the heading of the user has changed almost 360 degrees when no (detectable) walking steps were made. It should be noted that one stop was detected in the accelerometer pattern. This can be treated as faulty step detection, although the user has been turning with slightly moving feet, but without a strong step pattern present.
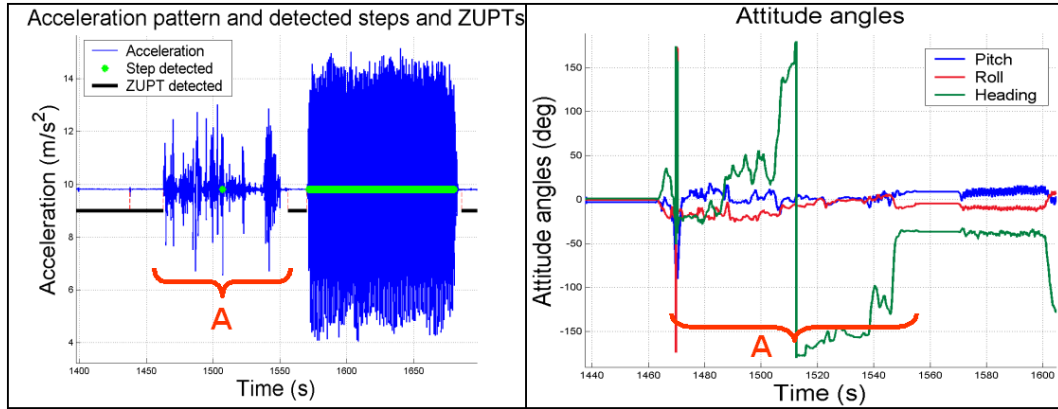
Figure 5.3: Attitude Update During a User Stop When the User is Not Walking But Is Not Completely Static Either

Complete motionless stops made by a pedestrian can be detected through variance analysis of the ISA signals (Collin, 2001). For more reliable stop detection, several gyro and accelerometer channels are subjected to the variance analysis. If the signal variances in the specified channels do not exceed predefined thresholds, a complete user stop is detected when

$$\mathbf{Z}_{(t_1...t_2)} \quad : \quad Var\left(v^i_{(t_1...t_2)}\right) \leq T^i \tag{5.3}$$

where

$\mathbf{Z}_{(t_1...t_2)}$ ... is the detected motionless stop for time period $(t_1 \ldots t_2)$, and

$v^i_{(t_1...t_2)}$ ... is the ith channel ISA signal during time period $(t_1 \ldots t_2)$, and

T^i ... is the pre-calibrated threshold of the variance of the ith ISA channel.

If a motionless stop is detected, the attitude of the user may not be updated and simply be propagated through time $(t_1 \ldots t_2)$ unchanged, or a ZUPT with attitude horizontal alignment may be performed as described in Section 2.2.4. If a motionless user stop is wrongly detected, or the time of the stop is incorrectly found, the

ZUPT procedure can worsen the performance of the PDR system. Both horizontal alignment and gyro bias removal procedures can introduce additional errors to the system. Thus, requirements for the selection of variance thresholds for ISA channels used in stop detection are quite strict.

5.3   Determination of Heading and Heading Error Model

The second step in the PDR mechanization scheme is the determination of the heading. The use of gyros as inertial instruments implies that the initial values of the attitude are provided, or the heading must be included as a state in the Kalman filter of the integrated PDR/GPS system. The heading initialization issue as well as the modeling of heading in the Kalman filter are discussed in Chapter 7 on system integration methodology.

To demonstrate the performance of the low-cost gyros used in the system, assume that the initial attitude (heading) of the system is known in the following examples. Using a full attitude solution, the heading is propagated using gyro measurements as described in Section 2.2.3. Figure 5.4 shows the field test data when a user has walked four loops around a rectangular parking loop and the ISA unit has been carried on the belt.

In this figure, the PDR trajectory is computed according to the above-described PDR algorithm. This test was conducted in an open-sky parking lot, so an accurate carrier-phase DGPS solution could be obtained as a reference. To obtain this reference, data from a geodetic grade NovAtel OEM4 GPS receiver was processed by carrier-phase based DGPS software (FLYKIN+^{TM}). At the start of the test, the initial PDR position was selected as the first DGPS available solution and was set as an origin for an LL coordinate frame. The system was static for about 15 minutes to obtain

Figure 5.4: Field Data PDR Solution and Carrier-Phase DGPS Reference: 4 Loops, Total of 851 Steps Walked in 7 Minutes and 41 Seconds

full ephemeris and to guarantee the convergence of ambiguities in the DGPS solution. The user then walked four loops, with one stop between each loop. The complete user stops were detected using variance analysis and are identified as ZUPTs on the figure. Except for the start and finish marks, the ZUPTs were performed at approximately the same point, so ideally they should be at the same spot on the plot (shown as "true ZUPTs location"). In this computation, a constant step length of 75 cm was used. From the very beginning, no use of GPS for any updates was performed. The total walking time was approximately 8 minutes.

Figure 5.4 clearly demonstrates the superiority of the PDR algorithm when compared to other inertial-based techniques. In 8 minutes of MEMS sensor-only based

navigation, the final 2D position error is less than 15 metres. Such a small error can be achieved with the classical inertial navigation system only when a navigation grade INS is used (El-Sheimy, 2003). The heading drift after each loop is clearly observed. The heading error after 8 minutes of walking is equal to about 20 degrees, which is expected with this quality of MEMS gyros.

Figure 5.5 shows a similar example, where a user walked 4 loops of a trajectory that was slightly larger and of a different shape. In this example, the initial heading was also assumed to be known. The total walking time was equal to approximately 17 minutes. After each loop, a ZUPT was performed by the user. The ZUPTs were performed at the same location, shown on the figure next to the true start of the test. In this test, no GPS updates of any kind were used to update the PDR system. During this slightly longer walking time, the heading error reached approximately 50 degrees, which is, again, expected for this quality of inertial MEMS sensors. The 2D position error after 17 minutes of PDR-only navigation was equal to 125 metres. This position accuracy is superb when compared to classical navigation schemes utilizing the same quality inertial sensors (El-Sheimy, 2003).

These PDR-only navigation results are shown when the initial attitude is provided. In practice, it is one of the largest problems in PDR and any other inertial navigation system and is rarely ever accurately known. In this example, the user maintained a fairly constant step length of approximately 75 cm, the value that was used in the computation. Obviously, a larger or smaller step length value used in the algorithm will produce more stretched or more concise loops. The final error, though, will not be significantly larger because the trajectory loops around over and over. A method to assess the accuracy of the PDR system with different step length error models is proposed in the following section.

From a practical viewpoint, in a PDR mechanization one should be concerned only
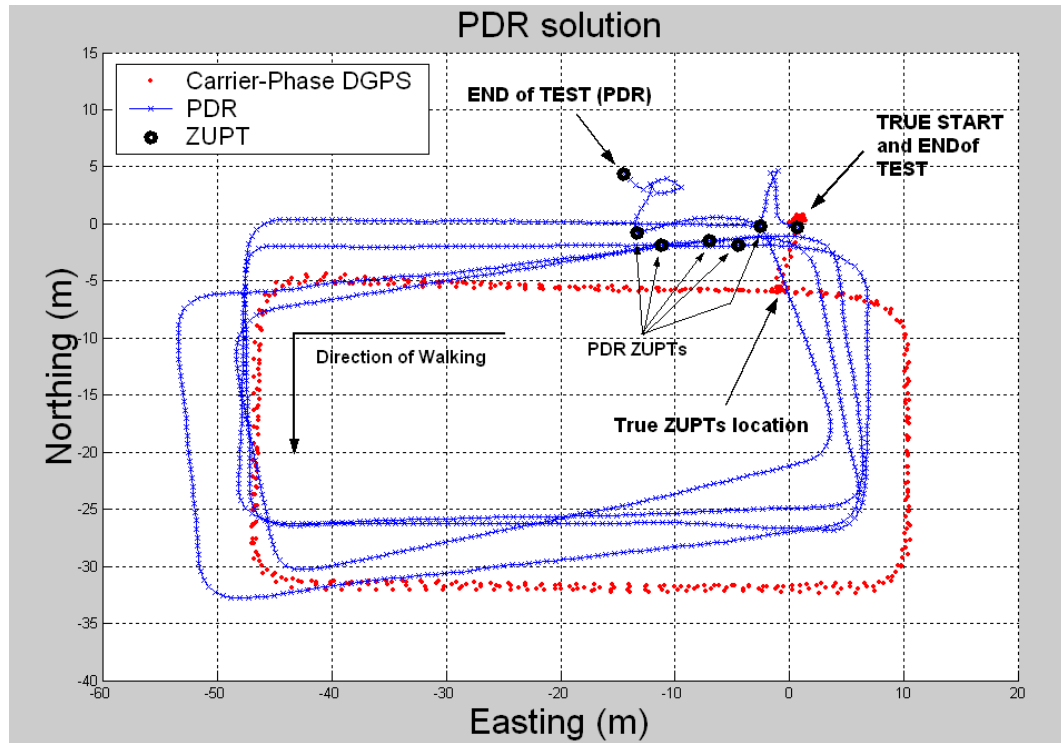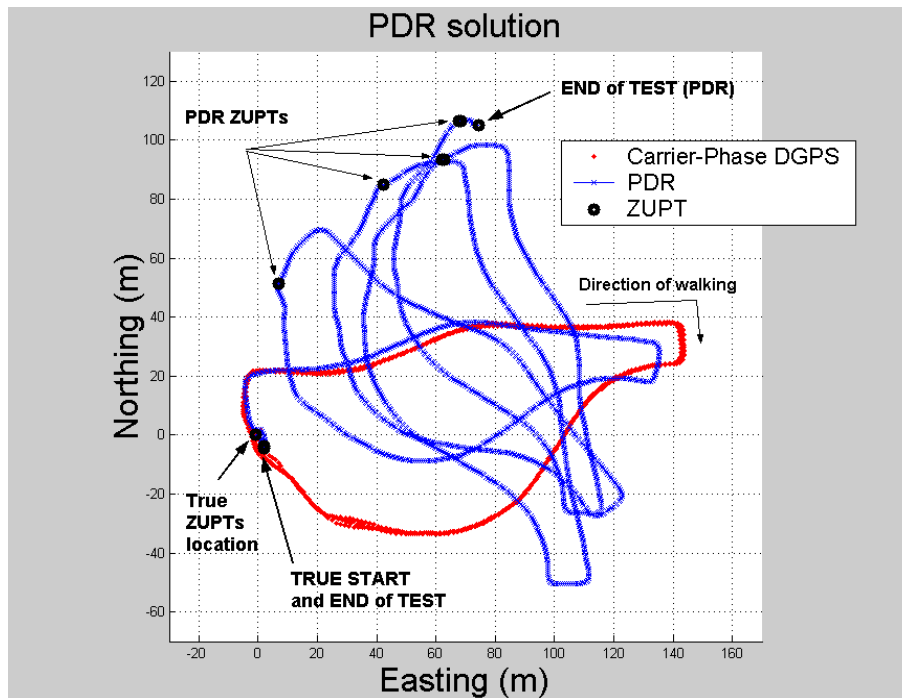
Figure 5.5: Field Data PDR Solution and Carrier-Phase DGPS Reference: 4 Loops, Total of 1890 Steps Walked in 16 Minutes and 34 Seconds

with the heading component of the attitude solution. A very detailed analysis of the performance of low-cost MEMS gyros for pedestrian navigation is given by Mezentsev et al. (2004). In this work, low-cost PDR data is analyzed on the kinematic case, when an accurate reference for the heading has been obtained by carrying a tactical grade IMU with 1 degree per hour bias gyros. When compared to a low-cost MEMS system, such biases can be considered negligible. It has been concluded that the gyro rotation rate biases can successfully be modeled by a random walk process. Thus, in the angular domain, the drift can be modeled as an integrated random walk process. Figure 5.6 shows an angular drift of an Analog Devises ADXRS150 gyro during a static 20-minute period. Along with the real gyro angular drift, a random realization of an integrated random walk process is simulated. The integrated random walk

process is simulated according to the model and parameters given by

$$r_{i+1} = r_i + w_i; \quad w \sim N\left(0, 10^{-6} \ deg^2/s^2\right)$$

$$h_i = \sum_{k=1}^{i} r_k \cdot \Delta t_k \tag{5.4}$$

where

r ... is the random walk process for rotation rate gyro bias, and

w ... is the driving white noise of the random walk process, and

Δt_k ... is the process sampling interval, and

h ... is the integrated random walk process with driving white noise w.

Figure 5.6: Drift of a MEMS ADXRS150 Gyro While Static. Also Shown is Simulated Random Realization of an Integrated Random Walk Process With $w \sim N\left(0, 10^{-6} \ deg^2/s^2\right)$ as the Driving Noise
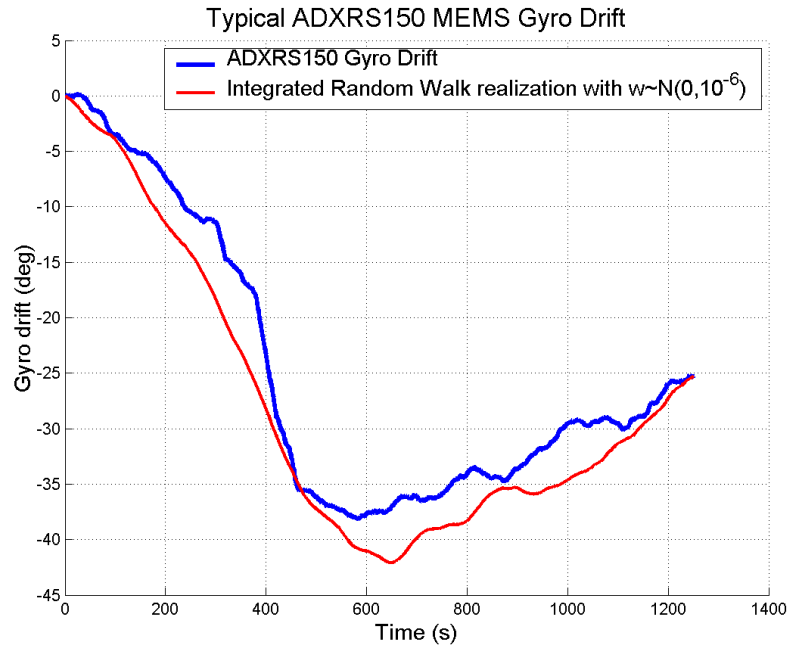
As can be seen from Figure 5.6, the integrated random walk process can realistically represent the angular drift of a low-cost gyroscope. Analysis has also shown that the Gauss-Markov stochastic process does not have an advantage over a random walk process. Sudden changes, as well as long-term substantial gyro biases, can be better modeled and represented by a random walk process rather than by a Gauss-Markov process (ibid). In the integration scheme developed in Chapter 7, a random walk model will be used to represent a gyro bias. Accordingly, an integrated random walk process will represent the heading drift of the PDR system.

5.4   Step Length Error Modeling

As has been previously mentioned, there are two major types of errors in PDR mechanization: step length estimation error and heading estimation error. In this section, a method to analyze step length error, and the effect this error has on traveled distance estimation and on 2D position accuracy, together with heading error, is proposed.

Even with the use of specific shoe mounted RF (Brand and Phillips, 2003) or inertial sensors (Stirling et al., 2005), user step length cannot be estimated perfectly. Some error will still remain. The behaviour of step length error needs to be properly modeled, and the effect of this error on PDR position accuracy needs to be assessed. Step length parameter can be written as

$$s_i^t = \hat{s}_i + \delta s_i \tag{5.5}$$

where

s_i^t . . . is the truth step length at i^{th} epoch or step, and

$\hat{s}_i$ . . . is the estimated (or modeled) step length at i^{th} epoch or step, and

δs_i ... is the remaining step length estimation error at i^{th} epoch or step.

Step length error can be modelled as one of the following common stochastic processes:

Gaussian Noise. Step length error is modeled as random Gaussian uncorrelated error in each step length with variance $\sigma^2_{s,GN}$;

Constant Bias. Step length error is modeled as a constant random error in each step. Variance of the initial constant error is $\sigma^2_{s,CB}$. In this case, the remaining random noise component of the step length error estimate is negligible for long-tern navigation as compared to the constant bias;

Gauss-Markov Process. The step length error in each step is assumed to follow a 1st order Gauss-Markov stochastic process.

Random noise models, that is Gaussian Noise or Gauss-Markov process error models, contribute to small step size variations due to environmental factors and irregularities in walking conditions. In addition, random constant error is due to the initially incorrect assumption of the step size, or to a wrong initialization with poor data. In many applications, stochastic error models are derived using continuous-time processes as the underlying truth, which are then sampled at discrete time. A PDR system is a discrete-time system in nature; therefore, this transformation is not necessary. This is why time is omitted from the following error models and step count is used as a varying parameter.

5.4.1 Gaussian Random Noise Model

If step length error, δs_i, is modeled as a Gaussian random noise error, it can be written as

$$s_i^t = s_i + \delta s_i$$

$$\delta s_i \sim N\left(0, \sigma_{s,GN}^2\right) \qquad (5.6)$$

where

s_i ... is the modeled step length value (modeled or assumed constant) at i^{th} step or epoch, and

$\sigma_{s,GN}^2$ ... is the variance of the Gaussian noise process.

In this case, step errors are uncorrelated during a walk, and the distance error variance after N steps can be found according to

$$\sigma_{N,GN}^2 = Var\left(\sum_{k=1}^{N} \delta s_i\right) = \sum_{k=1}^{N} E\left(\delta s_i^2\right) = N \cdot \sigma_{s,GN}^2 \qquad (5.7)$$

where

N ... is the number of steps, and

$\sigma_{N,GN}^2$ ... is the variance of walking distance error after N steps.

This result means that if the user's step length error model follows random Gaussian noise behaviour, the final uncertainty after N steps will be proportional to the number of steps made. The larger the random spread in the step length the user makes, the larger the final distance uncertainty will be.

Also, it should be noted that no assumptions on the time of step occurrence were made. This again illustrates advantage of PDR mechanization, where the error prop-

agates with the performed steps and not time, as in classical inertial mechanization schemes.

5.4.2 Constant Bias Model

If the step length error, δs_i, is modeled as a Constant random bias, it can be written as

$$s_i^t = s_i + c \tag{5.8}$$

$$c \sim N\left(0, \sigma_{s,CB}^2\right) \tag{5.9}$$

where

s_i ... is the modeled step length value (modeled or assumed constant) at i^{th} step or epoch, and

c ... is the constant step length error, and

$\sigma_{s,CB}^2$ ... is the variance of the initial constant error.

In this case, the remaining step length error after appropriate modeling, or after assuming the step length as a constant, is a constant bias. This error is random over time but is constant for every step length during the analyzed walking path. In this case, the error is constant for all steps; therefore, the distance error variance after N steps can be found according to the following equation

$$\sigma_{N,CB}^2 = Var\left(\sum_{k=1}^{N} c_k\right) = \sum_{k=1}^{N} N \cdot c = N^2 \cdot \sigma_{s,CB}^2 \tag{5.10}$$

where

N ... is the number of steps, and

$\sigma_{N,CN}^2$ ... is the variance of walking distance error after N steps.

In this case, the walked distance error variance is proportional to the square of the step count and the variance of the initial constant error. In this model, also, no assumptions on the time of step occurrence were made.

5.4.3 Gauss-Markov Model

If the step length error, δs_i, is modeled as a Gauss-Markov process of 1st order, it can be written as

$$s_i^t = s_i + \delta s_i = s_i + \delta s_{i-1} \cdot e^{-\beta} + \varepsilon_i \tag{5.11}$$

$$\varepsilon_i \sim N\left(0, \sigma_{s,GM}^2\right) \tag{5.12}$$

where

s_i ... is the modeled step length value (modeled or assumed constant) at i^{th} step or epoch, and

δs_{i-1} ... is the step length error at $(i-1)$ step or epoch, and

$1/\beta$ ... is the Gauss-Markov model correlation coefficient, and

$\sigma_{s,GM}^2$ ... is the variance of the driving Gaussian noise.

In this case, the walked distance error variance after N steps is equal to the variance of the integrated auto-regressive process and can be computed according to

$$\sigma_{N,GM}^2 = \frac{N \cdot \sigma_{s,GM}^2}{1 - e^{-2\beta}} + \frac{2\sigma_{s,GM}^2}{1 - e^{-2\beta}} \sum_{m=1}^{N-1} (N - m) \cdot e^{-\beta m} \tag{5.13}$$

where

N ... is the number of steps, and

$\sigma_{N,GM}^2$ ... is the variance of walking distance error after N steps.

The error growth properties of the above model are between random constant and random noise models. The proper value of the model correlation parameter, β, depends heavily on the step measurement technique used, as well as on many environmental factors. In this thesis, examples of error behaviour with the first two models, random noise and ransom constant bias, will be given as they completely represent two extreme cases of step length error behaviour.

The choice of values for input noise variance for both models, $\sigma^2_{s,RN}$ and $\sigma^2_{s,CB}$, depends on the uncertainty of user motion, in particular, step length consistency during the walk. Such uncertainty can be decreased if additional information about user dynamics is considered in the step length estimation filter (Ladetto, 2000).

5.5   Position Accuracy Measures in PDR Systems

It can be shown that the biggest PDR position errors occur in the case of a *straight walking path*, a *constant step length error* and *continuous walking*. The easiest way to visualize that is to imagine a user making two consecutive steps while walking straight. Suppose that for every step, the step length estimation error is constant and is equal to (δs). After two consecutive steps forward, the walking distance estimation error will be equal to double (δs), that is $(2 \cdot \delta s)$. The position estimation error will also be equal to $(2 \cdot \delta s)$. If, after making one step forward, the user makes one step backward with the same error in step length, the resultant distance walked error will also be $(2 \cdot \delta s)$, but the resultant position error will be nullified! If after the first step, the user turns, no matter what the angle, the distance estimated error will still be equal to $(2 \cdot \delta s)$, but the position error will be somewhere between 0 and $(2 \cdot \delta s)$.

With the proposed stochastic models for heading and step length errors, we will

seek the statistical upper bounds of the 2D position error after the given time for PDR-only navigation. This should provide the means to estimate how long a user can navigate without any updates from GPS and without exceeding the specified position accuracy.

Figure 5.7 shows a geometrical interpretation of the area where a person might end up, assuming the presence of the discussed errors: the step length error and the heading error in the case of actual straight walking. In Figure 5.7, point **O** represents the true user position after N steps walking straight. Points **A** and **B** represent the $1\sigma_S$ along-track uncertainty region due to the step length error modeled as one of the three described stochastic models. In this case, it is assumed no heading error is present. Points $\mathbf{A}^-$, $\mathbf{O}^-$, $\mathbf{B}^-$ represent the above points if, together with the step length error, the heading error is present. In this case, "maximum negative" drift implies the maximum deviation from the straight line in a counterclockwise direction resulting from the worst-case scenario of the integrated random walk heading error model. Points $\mathbf{A}^+$, $\mathbf{O}^+$, $\mathbf{B}^+$ represent the above positions if the maximum positive heading drift error is present.

The $1\sigma_S$ along-track position error is due to the step length error and can be calculated according to Equations 5.7, 5.10 and 5.13 for the three analyzed models. The $1\sigma_G$ error is due to heading drift (gyro drift) and must be estimated in order to estimate the position uncertainty of the user.

To find the upper bound of the across-track error due to heading error, a constant heading drift is assumed that corresponds to the maximum standard deviation of the integrated random walk process for a given walking time. Thus, it is necessary to consider the deflection of points $\mathbf{O}^-$ or $\mathbf{O}^+$, from the truth path as a 1σ error caused by the gyro drift. If we assume that for every step the heading error meets its maximum error expectation, then the $1\sigma_G$ across track error can be approximated
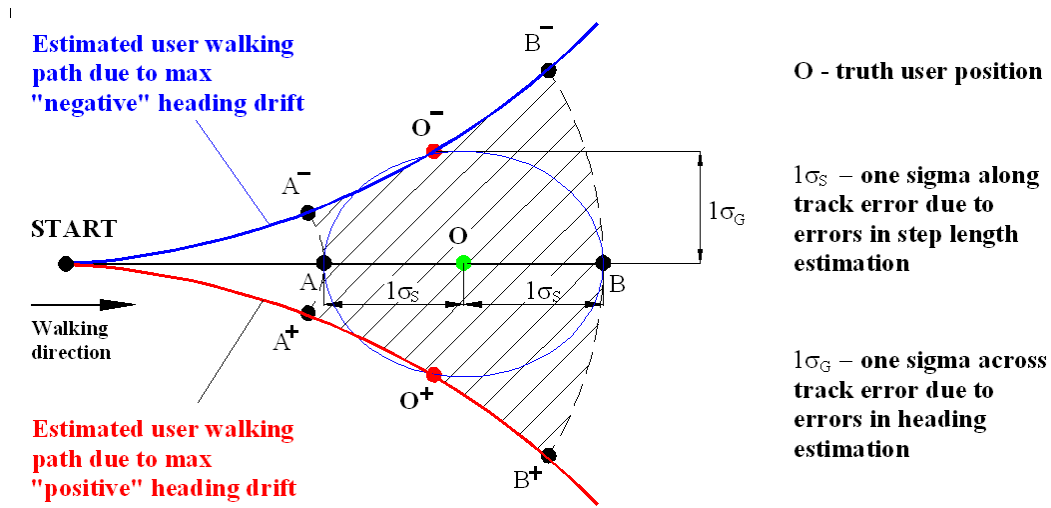
Figure 5.7: Geometry of a Pedestrian Walking Path Error in Presence of Step Length and Heading Errors in the Case of Straight Walking.

as

$$\sigma_G \approx \sum_{k=1}^{N} s_k \cdot \sin\left(\int_{t_1}^{t_k} D^{max} dt\right) \tag{5.14}$$

where

N ... is the number of steps, and

s_k ... is the length of kth step, and

D^{max} ... is the "maximum" constant heading drift in rad/sec.

Then, the corresponding 1σ 2D position error ellipse can be formed from the two estimates of the along-track and across-track errors. In this case, the measure of the horizontal 2D accuracy could be taken as the Distance Root Mean Square (DRMS) value, computed according to

$$DRMS = \sqrt{\sigma_{S,N}^2 + \sigma_{G,N}^2} \tag{5.15}$$

where

$\sigma_{S,N}^2$ ... is the variance of the distance error due to the step length errors after N steps, and

$\sigma_{G,N}^2$ ... is the variance of the across track error due to the heading error after N steps.

To estimate the accuracy of the PDR system by the proposed method, simulations are run. Table 5.1 presents a summary of the parameters used in the simulation. Two step-length error models are considered: Gaussian Noise model and the Constant Bias model. Two cases of the constant bias drift are considered.

Table 5.1: PDR Accuracy Simulation Parameters

Parameter	Value
Walking type	Non-stop, straight
Number of Steps, N	1000
Duration of Step, t_{step} (sec)	0.7
Length of Step, s_i (m)	0.7
Max Heading Bias Drift, D^{max} ($°/hour$)	100 and 300
Step Length Variance, σ_s^2 (m^2)	$(0.1)^2$ and $(0.2)^2$

Figure 5.8 shows the results of the PDR accuracy simulation for the Gaussian Noise step error model. Also, this plot shows the simulated accuracy of the traditional INS mechanization scheme in stand-alone mode, provided it is based on the equivalent accuracy gyros as simulated PDR systems (El-Sheimy, 2003). In this case, when the step length error follows the Gaussian Noise model, heading error is the dominant cause of the positional error in the PDR system. For example, after 1000 steps performed in 700 seconds (Table 5.1), the 1σ alone-track uncertainty caused by the step length error with (0.2^2) m^2 variance is equal to 6.3 metres, while the across-track 1σ uncertainty caused by the $300^{°/hour}$ constant bias drift is equal to 327 metres.

Figure 5.8 shows the results of the PDR accuracy simulation for the Constant Bias
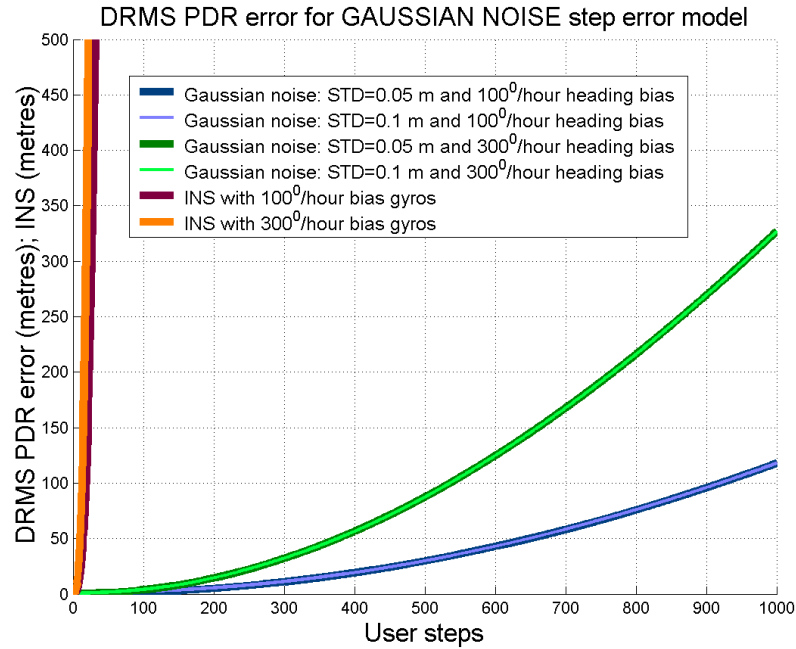
Figure 5.8: DRMS PDR Errors With the Step Length Error Modeled as Gaussian Noise

step error model. In this case, both errors, which are caused by the constant bias in each and every step made by the pedestrian and the maximum heading drift, contribute almost equally to the resultant DRMS PDR position error. For example, after 1000 steps performed in 700 seconds (Table 5.1), the 1σ alone-track uncertainty caused by the step length constant bias error with (0.2^2) m^2 variance is equal to 200 metres, while the across-track 1σ uncertainty caused by the $300^{\circ/hour}$ constant bias drift is equal to 327 metres.

It is clear from the results of Figures 5.8 and 5.9 that PDR navigation mechanization, even in the presence of both heading and step length errors, outperforms the traditional INS positioning for long-term unaided navigation.
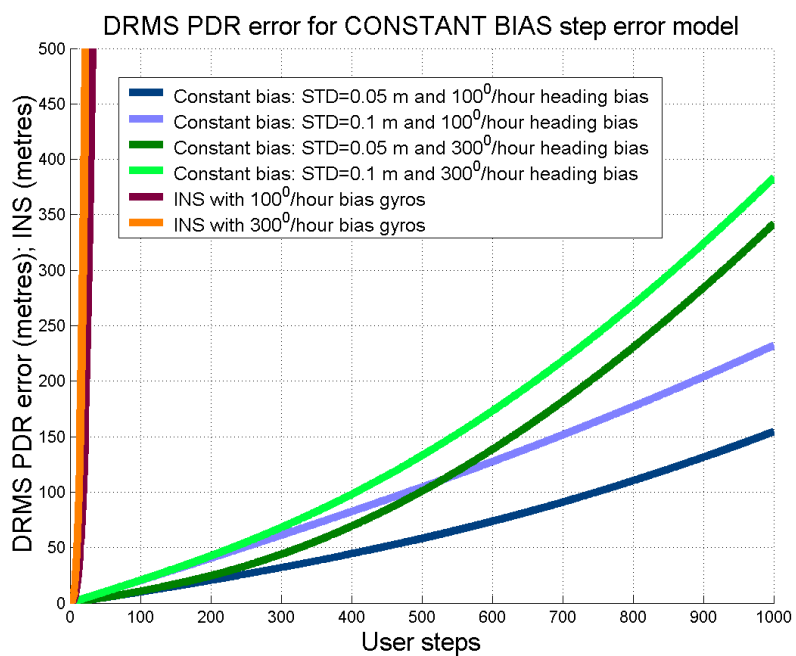
Figure 5.9: DRMS PDR Errors with the Step Length Error Modeled as a Constant Bias

Chapter 6

Performance of HSGPS in Signal-Degraded Environments

This chapter presents the testing results from an HSGPS receiver in a signal-degraded environment, and compares the epoch-to-epoch least-squares results to the receiver filtered solution. The chapter concludes with a presentation and discussion of the results of the RAIM method applied to the epoch-to-epoch LSQ.

6.1   Testing Environment and Test Description

Before moving to the integration of GPS with self-contained MEMS sensors, the results of the HSGPS receiver performance in stand-alone mode in a signal-degraded environment must be analyzed. In order to create a need for the use of any kind of additional sensors or systems, it must clearly be shown that using a stand-alone GPS receiver, in areas such as a downtown core, is a very poor solution and does not satisfy many of the accuracy requirements. For example, it will be shown that this solution, in this harsh signal environment, does not comply with the FCC requirements for the mobile handset-based solutions (FCC, 2001).

Figure 6.1 shows a photo of the Calgary downtown core environment, where the majority of the testing took place. The downtown area is a very dense urban canyon environment with buildings up to 60 stories high and elevation mask angles of up to 80 degrees. In this thesis, numerous tests on various trajectories and with different parameters such as the test start location have been performed. The HSGPS results

in most of the tests were found to be very poor. Results of many tests on pedestrian navigation can be found in, for example, Collin et al. (2003a); Mezentsev (2004); Mezentsev et al. (2004). In this chapter, one statistically representative test has been selected for analysis to demonstrate the quality of the signals, position and velocity solution accuracy as well as the results of integrity testing on the HSGPS data in this environment. The RAIM analysis is applied for two options: the global test only, and the global test together with the sequential rejection test (Chapter 3).

Figure 6.1: Calgary Downtown Environment

The receiver used in the testing is a high sensitivity SiRF Xtrac HSGPS receiver that is capable of outputting raw measurements (pseudoranges and Doppler) as well as receiver-generated position and velocity solutions. This receiver's solution will be referred as the *internal* receiver solution. The internal receiver solution is the result of filtering performed inside the receiver. The structure of the receiver position and

velocity filters is proprietary. It is not known how many observations are used in the solution, how the measurement variances are assigned to observations, and whether information from previous epochs is carried through to the current epoch (the case with Kalman filtering or clock modeling, for example). Also, no accuracy measures, such as the position and velocity variances, are associated with the output solution.

The internal receiver filter, though, sometimes performs extraordinarily well considering the harsh testing environments. Apparently, the quality of the internal receiver solution largely depends on the quality of the initialization of the receiver (Collin et al., 2003a). The receiver's filter can potentially access the receiver tracking loops' data and clock parameters, which can significantly improve the performance of the filter. This makes it extremely hard to design a filter that would outperform the internal receiver filter based on just the raw pseudorange and Doppler measurements. Thus, in this chapter the internal receiver solution will represent the filtered solution that can be achieved in a given environment by "heavy" filtering of the HSGPS data. The receiver filtered output will not be integrated with the MEMS ISA and is shown only for comparison purposes. The PDR/HSGPS integration will be performed with the raw HSGPS measurements as this allows more control and analysis of the data.

The raw HSGPS measurements, the pseudoranges and Doppler, are processed in the LSQ mode that is described in Section 2.1.3. For every test, the important processing parameters are summarized in a table. To display the position results, a digital map of downtown Calgary is used. This map is provided by the City of Calgary and is accurate to the metre level (Basnayake, 2004). In the map database, the streets are stored as straight lines that were surveyed by centre street points.

Any accuracy analysis of a positioning or navigation system requires a reference. In such a signal-degraded downtown environment, it is extremely hard to obtain a very accurate reference, especially in the position domain. It was mentioned that

due to very frequently interrupted carrier-phase measurements, an accurate carrier-phase based solution cannot be obtained. This has motivated some researchers to perform testing in an open-sky environment and then simulate various measurement outliers and measurement gaps in order to obtain very accurate position and velocity references. However, the simulation of outliers and data gaps in order to simulate downtown signal conditions is not an optimal approach. Multipath behaviour in a downtown core, along with longer integration times for the HSGPS receiver (the manufacturer's proprietary information that is not publicly available), makes the whole situation truly unpredictable and very hard to statistically represent through simulations.

Another way to obtain a precise reference is to have an extremely accurate inertial system onboard; however, this method also has several limitations. First, this system is extremely heavy and, together with the power supply and all the other equipment, is practically impossible to carry. Second, this method requires very precise initialization. Many tests are performed when the system is initialized in a downtown environment where no accurate initialization (carrier-phase based initialization) is available. Third, only a position reference can be obtained. The low-cost PDR unit used in the system is carried on a belt, while an accurate (but heavy) INS system must be carried in a specially-designed backpack. This introduces an attitude bias between the two coordinate body frames that is not observable during walking considering the substantial drift in sensors of the low-cost ISA unit (Collin et al., 2003b).

In this work, no simulation of outliers or data gaps of any kind is made. All the analyzed data is collected in a real downtown environment to fully represent the quality of the data a user experiences in this environment. Given the above observations, we can conclude that the only practical way to obtain a reference is to use the

available digital map. For this purpose, manual time tagging to mark certain locations (street intersections) is frequently performed during testing. At these points, a 2D accuracy assessment can be performed, since the location of the user on the map is known. Such accuracy analysis, though, is performed with high precision but limited accuracy. As has been mentioned, a digital map is produced by surveying the street's centre lines while a pedestrian walks on the sidewalks. This, by itself, introduces about 10 metres relative error when a user locates himself at an intersection and compares his position to this intersection's coordinates (which are based on the street's centre lines) on the map. Thus, position errors will be assessed at the marked points, and the numbers will be rounded to metres, keeping in mind this map's limited accuracy precision. During the rest of the test, the errors are vaguely assessed in across-track error domain.

The test trajectory, the photos of the test person and the urban canyon environment for this test are shown in Figure 6.2. This testing loop is around 1.5 km in length and is walked by a test person in approximately 30 minutes. In all intersections (shown on the figure as black markers with associated numbers), the data is manually time-tagged for accuracy assessment and for the more accurate time synchronization of the sensor data with GPS.

6.2 HSGPS Least Squares and Receiver Internal Results

This test was begun in a downtown environment, so no accurate position initialization was performed. It represents a practical situation when a user decides to use a handheld navigation device as she/he exits a downtown building or parking area. In this test the receiver was started in the *cold* start-up mode, which means that no ephemeris data was loaded into the receiver prior to testing. Instead, the receiver
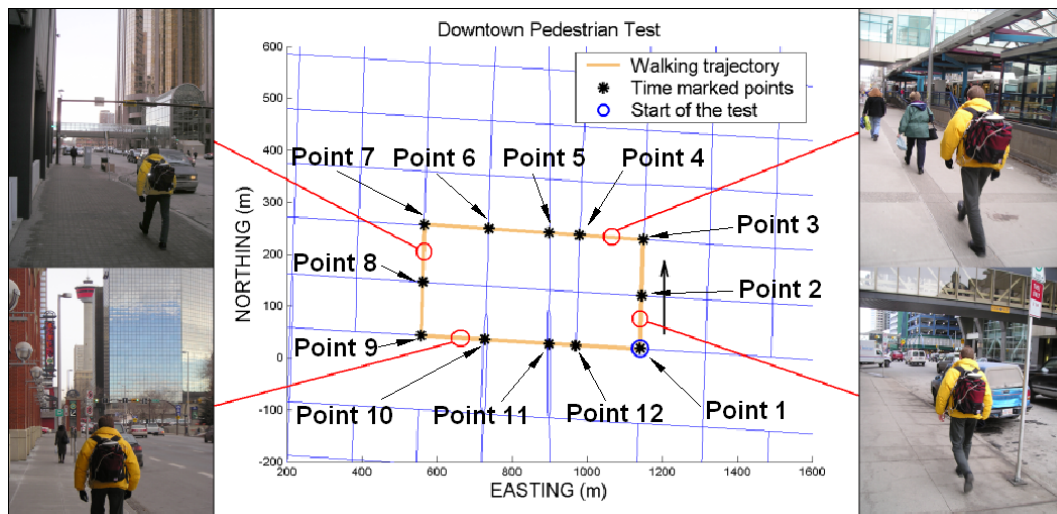
Figure 6.2: Calgary Downtown Pedestrian Walking Test Trajectory

(the antenna, essentially) was kept static for about 15 minutes. The raw data was processed in single point epoch-to-epoch LSQ mode. The motivation for using an epoch-by-epoch least-squares solution is to analyze more precisely the impact of low signal strength and high signal reflection on the accuracy of the measurements and positions, without the influence of a smoothing filter. It is understood that the use of such a technique is only for analysis purpose and would not be used in practice. In the latter case, a filter must be used to smooth these large errors and increase position accuracy and continuity. A summary of the test and the LSQ processing options are given in Table 6.2. Figure 6.3 shows the LSQ and the receiver internal position results plotted on the digital Calgary map in a local level coordinate frame. For comparison purposes, an LSQ solution obtained with a geodetic grade NovAtel OEM4 receiver is also plotted on this figure. This receiver is a standard sensitivity GPS receiver and its results are plotted to demonstrate the availability differences provided by the high sensitivity and the standard sensitivity GPS receivers in such environments. The accuracy of the OEM4 receiver solution will not be analyzed in

detail and is only shown to demonstrate its poor availability in such an environment.

Table 6.1: Downtown Walking Test Summary and LSQ Processing Options

Location:	Calgary DT
Test Length:	30 minutes; $\approx$1.5 km loop
Equipment:	SiRF HSGPS Xtrac receiver, NovAtel 700 antenna
Processing Mode:	LSQ, single point
Elevation cutoff:	0 degrees
Corrections:	Troposphere delay correction
RAIM:	Global Test; Global test + Local Test

The outstanding solution availability provided by the high sensitivity GPS receiver must be noted. The availability of the LSQ epoch-by-epoch solution with no RAIM algorithm implemented is 96%, and the availability of the internal receiver solution is 93%. The availability of the solution for the NovAtel OEM4 receiver is only 27%. Most of the solution epochs for this type of receiver happened during the initial stage of the experiment, when the receiver was static. In the walking part of the test, the availability is even less. As can be seen from the results of Figure 6.3, the errors in both the LSQ and the internal receiver solutions are very large. About 50 epochs of the LSQ solution are off the displayed map. One epoch of the internal solution is also off the map. The largest LSQ position error exceeds 9 km. The accuracy of the solutions is compared to the digital map at the marked points (Figure 6.2) and is summarized in Table 6.2.

From the results of Figure 6.3 and Table 6.2, it is obvious that the internal filtered receiver solution outperforms the LSQ solution as expected even if, at one point during the test, this internal solution started drifting away from the reference trajectory for about 30 consecutive seconds. The across-track position error reaches almost 600 metres. The LSQ solution, though, is scattered around the reference trajectory. The errors are frequently correlated from epoch to epoch. This can be explained by
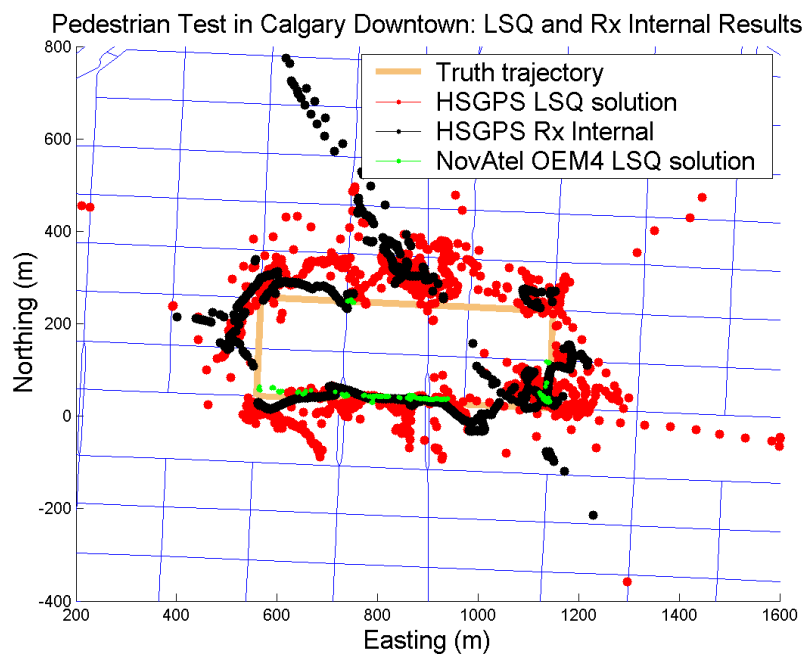
Figure 6.3: Downtown Pedestrian Walking Test: Single Point LSQ (no RAIM) and Receiver Internal Position Solutions for HSGPS receiver and LSQ solution for the OEM4 NovAtel Receiver

frequent correlated errors in the pseudorange domain, where errors such as multipath or echo-only signal tracking can "fool" the receiver loops for several consecutive epochs.

Figure 6.4 shows the LSQ and receiver internal velocity solutions for this test. It is known that multipath affects Doppler measurements less than the code measurements (Ray, 2002). The velocity solution is thus always expected to be of better quality than the position solution. It can also be seen that the receiver-filtered solution is much better than the LSQ velocity solution in such an environment. The error in the LSQ velocity reaches one kilometre per second error values for several epochs. For the reasons described above, a reference for velocity is also hard to obtain in

Table 6.2: Downtown Walking Test: Horizontal Position Errors at the Marked Points

Marked Point:	LSQ (m)	Rx Internal (m)
Point 1:	20	50
Start 2:	492	34
Start 3:	191	129
Start 4:	150	136
Start 5:	54	50
Start 6:	130	192
Start 7:	61	27
Start 8:	115	89
Start 9:	32	200
Start 10:	80	25
Start 11:	13	14
Start 11:	8447	41
AVERAGE:	**815**	**82**

this environment. In pedestrian navigation, to roughly estimate the accuracy of the obtained velocity we can limit the velocity to pedestrian walking speeds, usually less that 2 m/s. Such bounds are also shown on Figure 6.4. The internal receiver solution almost always stays in those bounds, showing remarkable performance.

The primary goal of pedestrian navigation systems is to provide estimates of position rather than estimates of velocity. This is mainly because velocity information is of little interest to the user himself. Velocity data can very effectively be used, though, to provide better estimates of the user's heading. As will be shown in the next chapter, GPS velocity will not be directly taken as an updating measurement into the Kalman filter. Instead, the heading will be computed using the GPS velocities while the user is walking, and this measurement will be used as an update in the filter. For that matter, the internal receiver velocity can also be used. In the experimental results section, it will be noted whether the LSQ velocity or the receiver internal velocity solution is used.
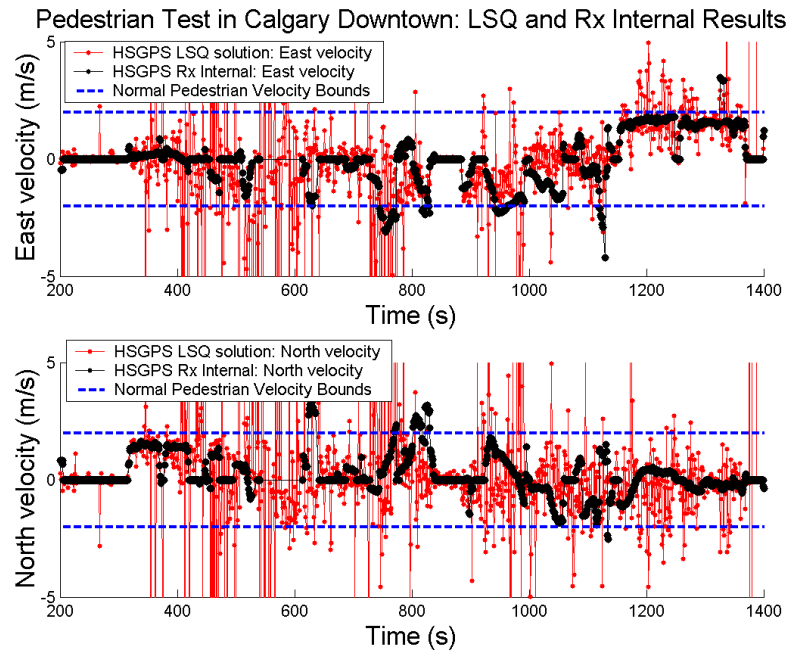
Figure 6.4: Downtown Pedestrian Walking Test Results: LSQ and Receiver Internal Velocity Solutions

6.3 RAIM Results

Let us now analyze the performance of the RAIM algorithm on the HSGPS data. First, the RAIM algorithm with global testing only is applied. The parameters of the RAIM algorithm are set as $\alpha = 0.1\%$ and $\beta = 10\%$. These parameters have been shown to be the most appropriate in such signal-degraded environments (Kuusniemi et al., 2004). Figure 6.5 shows the results of the global test RAIM procedure applied to HSGPS data. The parameters of the LSQ processing are the same and are summarized in Table 6.2.

As may be seen from Figure 6.5, the RAIM results are not overly successful when applied to HSGPS data in a downtown environment. In the north part of the trajec-
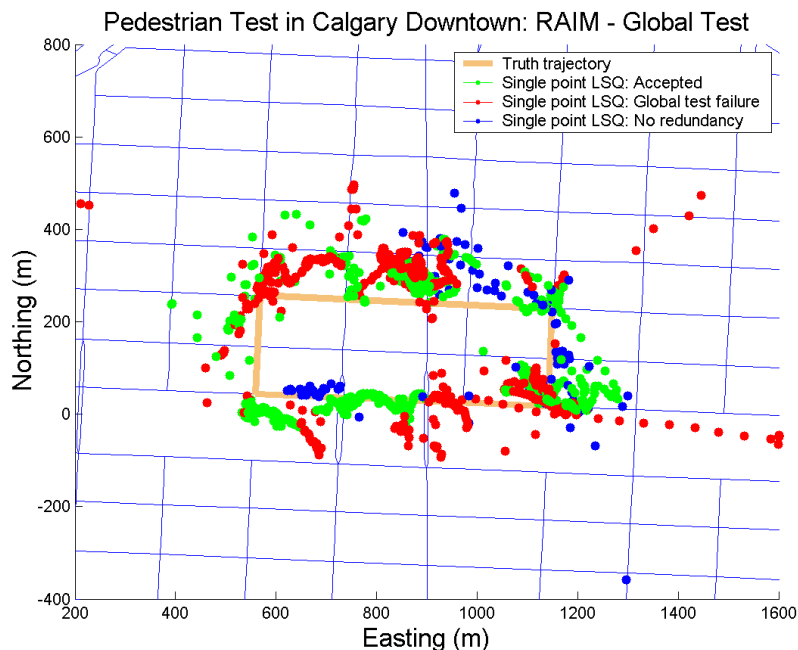
Figure 6.5: Downtown Pedestrian Walking Test Results: LSQ RAIM Results, Global Consistency Test is Applied

tory, many epochs of the solution are treated as ones that passed the RAIM global test (marked on the map in green). For many of these epochs, the across-track errors reach hundreds of metres. The epochs that did not pass the global test checking are colored on the map in red. Some of the epochs were not subjected to global test checking due to the lack of redundancy. In the case of 3D positioning, 5 or more measurements are required to perform such RAIM analysis.

For this test, 43% of the total solution epochs are considered as *accepted* (Global test passed), 40% of epochs failed the global consistency test and 17% of the epochs did not have enough redundancy for the RAIM to be performed. For the epochs, at which the global test failure is detected, the sequential residual testing sequence may be initiated. Figure 6.6 shows the results of this downtown pedestrian test with
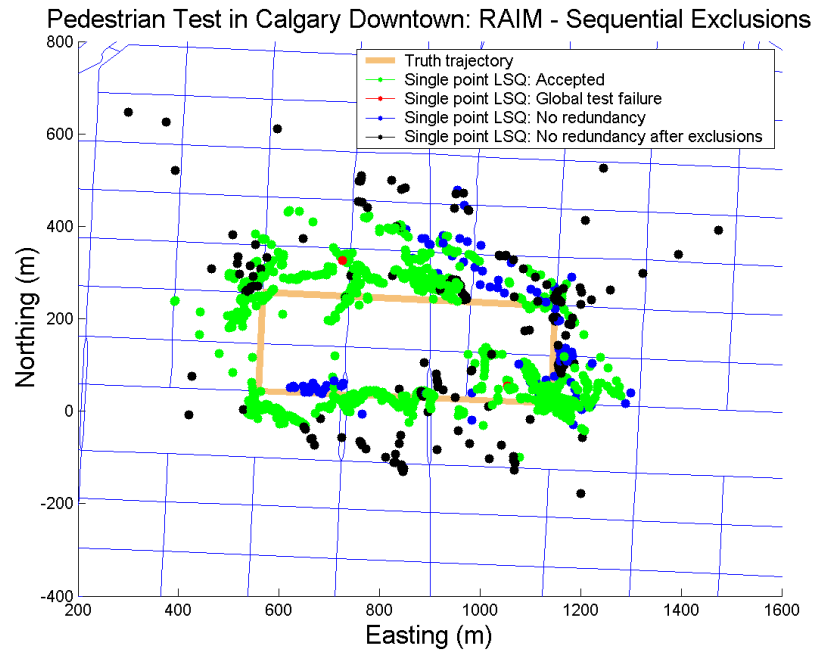
the sequential RAIM algorithm applied.

Figure 6.6: Downtown Pedestrian Walking Test Results: Sequential Rejection Test is Applied

In this method, only epochs that did not pass the global test are subjected to the test of individual residuals. First, if the global test detects an inconsistency in the measurements (global test failure) and the local detects the measurement with the largest residual that exceeds the threshold, it rejects it. If the redundancy after the exclusion permits, the global test and the local test sequence is repeated. If the redundancy does not allow us to perform the global test (providing the number of observations has been brought down to 4 for 3D positioning, or 3 for 2D), this solution is marked as *no redundancy after exclusions*. Second, there is a possibility that after the global test failure (the inconsistency is detected), the local test will not be able to find an observation with the largest residual that exceeds the threshold.

Table 6.3: Downtown Walking Test: Horizontal position errors at the marked points, LSQ sequential RAIM

Marked Point:	LSQ (m)	Marked Point:	LSQ (m)
Point 1:	20	Point 7:	115
Point 2:	40	Point 8:	100
Point 3:	191	Point 9:	32
Point 4:	150	Point 10:	42
Point 5:	54	Point 11:	13
Point 6:	20	Point 12:	62
AVERAGE:	70		

This case is referred to as an inconsistency between the global and the local tests themselves. There are not many cases of such inconsistencies occurring in real data. This type of inconsistency between the RAIM testing procedures has been addressed in some fashion by Kuusniemi and Lachapelle (2004).

After the local residual testing procedure is applied, the number of epochs that are considered as *accepted* is now 70%. The number of epochs for which the global test failed but the local test could not reject any observation is equal to 4, that is 0.25% of the total epochs during almost 30 minutes navigation. The same 17% of the solution epochs that are marked *no enough redundancy* to perform a global test are not subjected to the local test procedure. After the exclusions, 13% of the solutions are treated as *not enough redundancy after exclusions are made*. In the case of 3D positioning, this is when 5 observations at an epoch are subjected to the global test. The global test has indicated an inconsistency in these measurements. The local test has excluded one observation from the solution. The remaining 4 observations are not enough to perform further global tests; therefore, the testing stops here. The accuracy of the LSQ solution with the sequential RAIM algorithm applied at the marked points is summarized in Table 6.3. Here, only *accepted* solutions are considered for accuracy analysis.

As has been mentioned in Chapter 2, the height fixing method can increase the availability of the solution by increasing redundancy by one. Figure 6.7 shows the results of LSQ processing when height fixing is applied. The height can be fixed to a value that has been obtained with the first reliable 3D GPS solution. If the barometric measurements are available, which is the case with the PDR system, the height in the integrated system can be propagated in differential mode with respect to to the "reliable" GPS height solution. The tricky part here is to select a reliable solution. Essentially, all the approaches to the selection of that reliable solution epoch are ad-hoc. In this thesis, it is proposed to use an epoch that has a VDOP parameter of less than 2 to obtain an absolute user altitude estimate. After this epoch, the solution switches to a 2D navigation mode; that is, the height component in the LSQ algorithm becomes fixed, increasing the redundancy of the solution by one. Figure 6.8 shows how the height is propagated with the barometer differential measurement after a GPS epoch with a good vertical solution geometry is chosen. This method of height aiding with a barometer is known as baro-altimeter aiding.

Figure 6.7 shows the results of the test when a height fixing constraint has been applied. In this case, the availability of the solution has become 100%. As can be seen, far more epochs are now treated as global test failures: 90% of all epochs. 9.7% are treated as *accepted*. And only 5 epochs have redundancy to perform a global test procedure. This increase in the percentage of the global test failure can be explained by the increased number of diverse, multipath-affected measurements in a single epoch. More multipath-affected signals increase the chances of detecting an inconsistent situation in the solution. Overall, the quality of the solution does not improve. The maximum position error remains as a kilometre value. The 10% of the accepted solution epochs also have substantial position errors of hundreds of metres across-track. Table 6.3 summarizes the horizontal position errors at the
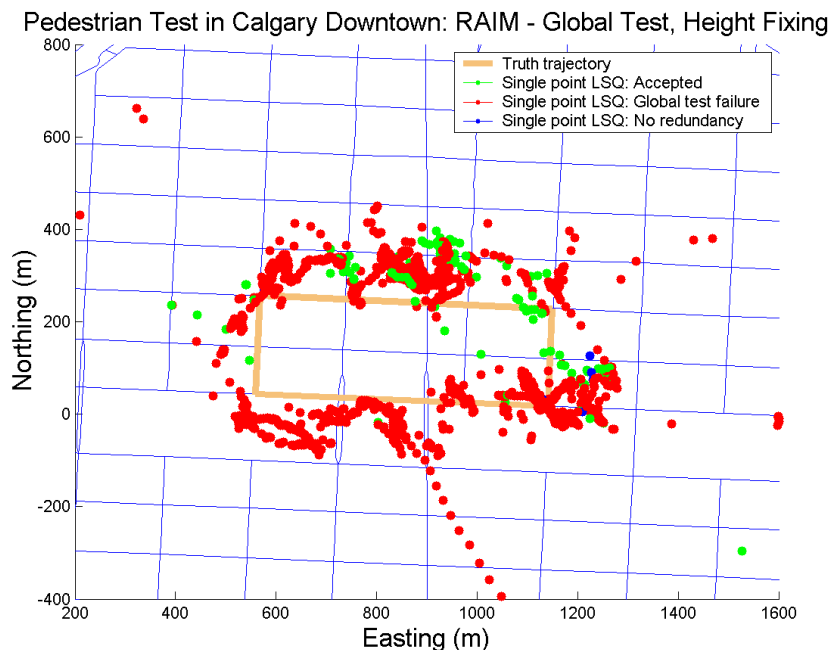
Figure 6.7: Downtown Pedestrian Walking Test Results: RAIM LSQ results, Global Inconsistency Test is Applied when Height Fixing is Used

marked points for this case.

Figure 6.9 shows the results of this test when the sequential testing RAIM procedure has been applied together with height fixing. This also does not improve position accuracy, and most importantly solution accuracy estimation, by much. The majority of the solution epochs are now treated as ones that passed the global test after a certain number of rejections were performed. In this sequential observation rejection procedure, 84% of the solution epochs are now treated as ones that passed the global test, 1.3% of the total epochs are ones that failed the global test, the same 5 epochs are marked as not having enough redundancy to perform any RAIM analysis, and 14.4% of the epochs are treated as not having enough redundancy to perform any future analysis after observation rejections have been made. Table 6.3 summarizes
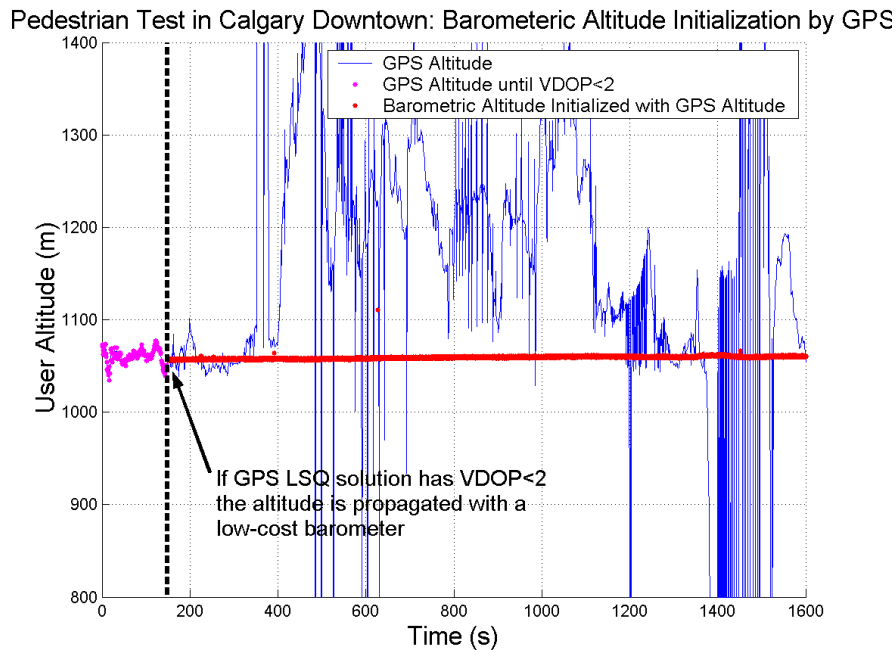
Figure 6.8: Downtown Pedestrian Walking Test Results: Barometric Altitude is Initialized by GPS altitude if VDOP factor < 2

horizontal position accuracy at the marked points considering only *accepted* solution epochs.

All this analysis shows that the applicability of the RAIM techniques is very limited to HSGPS data in signal-degraded environments when using an epoch-by-epoch least-squares solution approach. The biggest assumption in the RAIM algorithm is the occurrence of *only* one blunder at a time, meaning one blunder in one epoch. In this environment, such an assumption clearly does not hold. Chances are that all the measurements are affected by multipath to some extent, which practically nullifies this assumption. Some pseudoranges are affected more than others, and when RAIM analysis is applied it is hoped that the inconsistency will be detected and the largest errors will be sequentially removed. Unfortunately, this is not always the case, as

Table 6.4: Downtown Walking Test: Horizontal Height Constrained LSQ Position Errors at the Marked Points

Marked Point:	LSQ (m)	Marked Point:	LSQ (m)
Point 1:	6	Point 7:	66
Point 2:	480	Point 8:	127
Point 3:	176	Point 9:	67
Point 4:	119	Point 10:	87
Point 5:	60	Point 11:	72
Point 6:	131	Point 12:	8074
AVERAGE:	789		

Table 6.5: Downtown Walking Test: Horizontal Height-Constrained LSQ With Sequential RAIM Position Errors at the Marked Points

Marked Point:	LSQ (m)	Marked Point:	LSQ (m)
Point 1:	420	Point 7:	22
Point 2:	136	Point 8:	176
Point 3:	590	Point 9:	67
Point 4:	119	Point 10:	90
Point 5:	100	Point 11:	70
Point 6:	88	Point 12:	63
AVERAGE:	161		

has been shown in several works, for example, in Kuusniemi and Lachapelle (2004); Collin et al. (2003a).

One of the major conclusions that this thesis attempts to support after very extensive real world testing is that there is no reliable way to detect a reliable position solution obtained with HSGPS in a signal degraded environment. A truly unpredictable multipath environment and very large signal degradation make all approaches to the selection of "reliable" solutions **ad-hoc**.
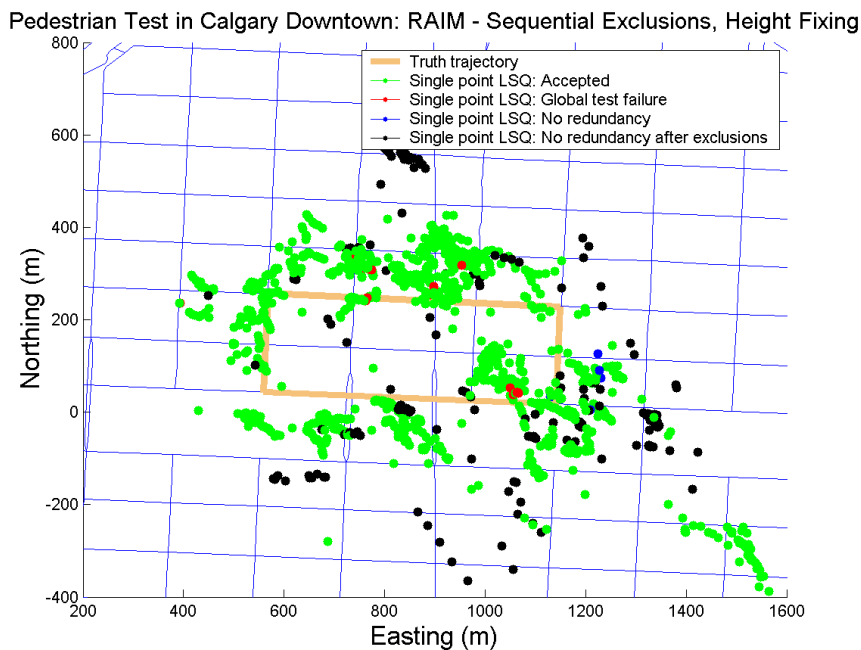
Figure 6.9: Downtown Pedestrian Walking Test Results: Sequential Rejection Test is Applied when Height Fixing is Used

6.4 Signal Quality in a City Downtown Environment

The signal characteristics of HSGPS in signal-degraded environments, such as a downtown area, have already been extensively studied (MacGougan, 2003). The C/N_0 value is not fully representative of the signal quality because, most importantly, it depends on the antenna vertical gain pattern. If the antenna is equally sensitive in the horizontal plane, the C/No will indeed be due to attenuation due to blockage and reflection at low elevations nearly 100% of the time. The way the signal's quality is represented in a signal environment is *fading* rather than C/N_0. Fading is defined as the difference in signal strength received by a GPS receiver in an open-sky environment and by the receiver in a signal-degraded environment. The receivers

must be of the same type, although signal strength can be demonstrated without a base station. Nominal C/N_0 values for signals from high elevations satellites (from 45^0 to 90^0 elevation angles) are normally higher than 45 dB-Hz. At lower elevation angles (less than 45^0 degrees), the C/N_0 values gradually decrease to approximately 35 dB-Hz due to a longer propagation path. These number depend on the type of the antenna used and are given as examples for a NovAtel 700 antenna. Figure 6.10 shows the C/N_0 values for the analyzed test for all tracked satellites. There are also reference lines showing regions of signal strength for a given elevation. The regions are shown in 10 dB-Hz bins. It can be seen that for lower elevation satellites, the signals are more attenuated than for the high elevation satellites. Also, it can be seen that there are more satellites tracked by the receiver with lower elevation than with the higher elevation.
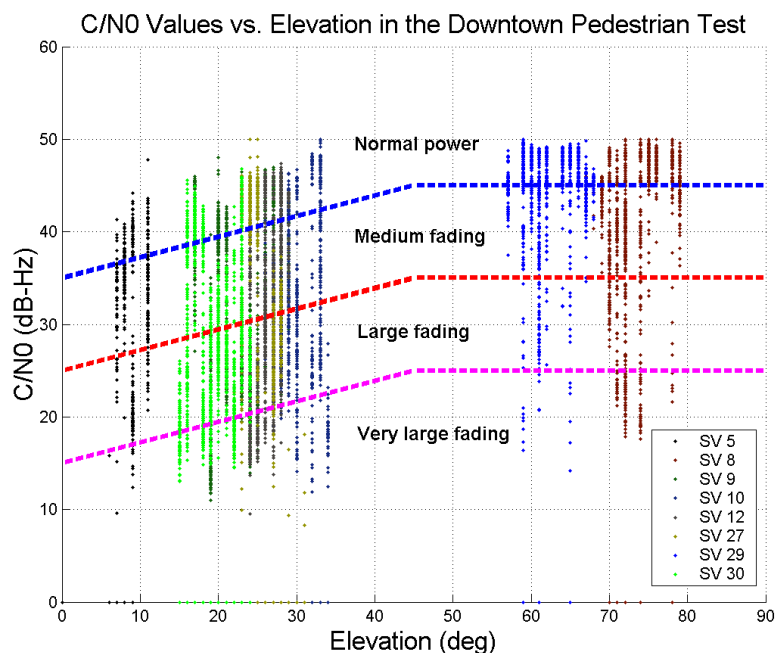

Figure 6.10: Downtown Pedestrian Walking Test Results: C/N0 values vs. Elevation

In reality, this demonstrates something quite opposite from the common assumption that in dense urban environments only high elevation satellites are tracked by the receiver. On street intersections, the visibility of the sky stretches along two (usually) perpendicular streets that may allow us to acquire low-elevation satellite signals. During the whole test, only 2 high-elevation satellite signals were tracked. This also demonstrates that the methods of de-weighting the observations with lower elevations (and as a result with lower C/N_0) in the LSQ processing is not an optimal approach. Also, elevation masks must be applied with great care. If an elevation mask of 10 degrees is applied, one satellite in this test becomes cut-off. An extreme elevation mask angle of 30 degrees will remove nearly all 6 low-elevation tracked satellites from the solution. In this case, 2 high-elevation satellites simply won't be enough even for a 2D solution.

Typically, in this environment, a UERE for pseudorange observations due to fading and multipath effects can be taken as 30-60 metres 1σ (MacGougan, 2003). This is a fairly significant increase from about 1-10 metres $1\ \sigma$ in the open-sky environment. This UERE, coupled with the dilution of precision factors, can produce position-accuracy estimates according to Equations 2.5.

Figure 6.11 shows the plot of HDOP, VDOP and the number of visible satellites during this test. During the whole test period, 24 epoch solutions have HDOP values larger than 10, and 20 epochs have VDOP parameters larger than 10.

Taking an average HDOP as 1.7 and 1σ UERE as 60 metres, a 1σ horizontal position solution error can be estimated as shown in Figure 6.12. Here, 0% of epochs complies with the FCC handset requirements of 50 metres error 67% of the time, and 83% of the solution epochs have horizontal errors of less that 150 metres, which also does not comply with the figure required by FCC of 95%. This simulation analysis is based on field data DOP factors and simulated UERE. As has been shown above, a precise

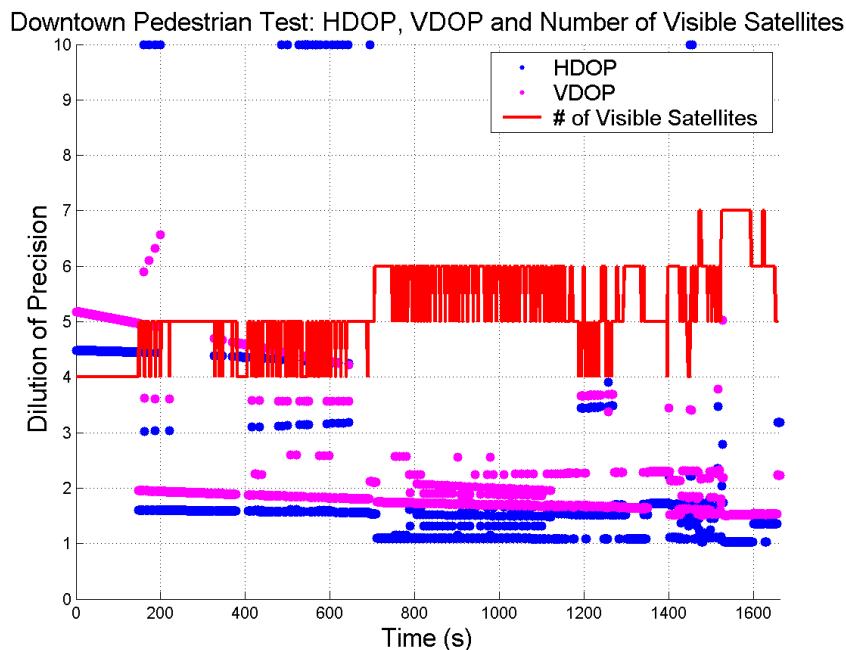Downtown Pedestrian Test: HDOP, VDOP and Number of Visible Satellites

Figure 6.11: Downtown Pedestrian Walking Test Results: HDOP, VDOP and the Number Of Visible Satellites

experimental accuracy assessment is very hard to perform in this environment during *kinematic* testing because it is so difficult to obtain a reference.

From the results presented in Figures 6.3 - 6.9, the position errors are a lot larger than the estimated ones with the assumed UERE and calculated DOP parameters. Obviously, this is due to an unpredictable multipath environment, and possible cross-correlation tracking or tracking echo only signal effects for which DOP is not the best accuracy measure. In this case, the UERE value needs to be adaptively increased according to the environment. In the design of an autonomous system, it is possible to detect the signal degraded environment and adjust the UERE value accordingly. For example, a signal degraded environment can autonomously be detected from the analysis of the variances of the C/N_0 values (Mezentsev et al., 2003). In the
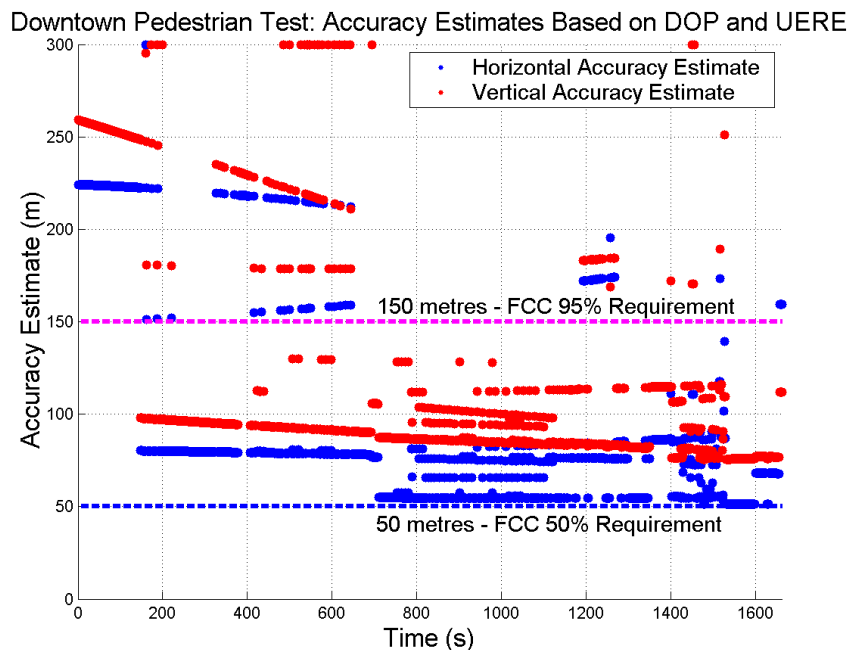
Figure 6.12: Downtown Pedestrian Walking Test Results: Horizontal and Vertical Position Accuracy Estimates based on HDOP, VDOP and UERE parameters

downtown area, the C/N_0 values will be varying very significantly, practically, for each tracked satellite. This is not characteristic to an open sky areas. Such variation can be seen in Figure 6.10.

This chapter clearly shows that there are no means available to improve the performance of GPS while increasing its sensitivity. Increasing the sensitivity makes the receiver "welcome" all possible multipath, cross-correlation and echo-only signals that only have signal strength above the threshold of the receiver. The filtering of GPS-only data is truly a challenge, and with the current state of the receiver tracking loop algorithms, they cannot be made as accurately as we would like them to be.

Chapter 7

Sensor Aiding Methodology of HSGPS

This chapter presents a proposed methodology for HSGPS aiding using a low-cost PDR system in signal-degraded environments. A detailed development of the Kalman filter model is given, followed by a discussion of aspects of reliability testing of the integrated solution. Finally, a simulation analysis is carried out to demonstrate the functionality of the proposed method.

7.1 Filtering and State Modeling Approach

As seen in the previous chapter, the quality of HSGPS data in a signal-degraded environment is extremely poor. The integrity analysis of the solution (RAIM) makes it possible to remove most of the large position outliers (kilometre level errors), but it does not improve the overall performance by much. In this chapter, a method to aid the HSGPS receiver using a set of low-cost sensors is proposed. The main goal of this chapter is to develop a Kalman filter that will tolerate, to some extent, large measurement outliers that may become the filter updates. This is essentially a difficult task considering the quality of both systems' data.

Even though there is poor data on both ends of the integration scheme, both HSGPS and MEMS PDR, the Kalman filter still needs to be properly and accurately tuned. One of the major issues in the development of a Kalman filter for the PDR/HSGPS system is *timing*. In classical INS/GPS integration schemes, the filter normally runs at the INS data rate and the available GPS epochs are the filter updates. The

data-sampling rate on the inertial systems is high (usually, more than 50 Hz); thus, the interpolation or extrapolation of the data required to synchronize the INS and GPS data to input into the filter is not difficult. The nature of the PDR systems is to propagate the position when user steps are detected. Normally, steps do not occur at the times of GPS updates, unless by chance. Therefore, the timing issue in a PDR/GPS integrated system needs to be carefully resolved. The next two sections discusses the timing issue for different filter modes and defines the filter modes depending on the user motion state.

7.1.1 Timing in the Integrated PDR/HSGPS Systems

In existing works on PDR integrated systems, user-step frequency is commonly used for the time base of the PDR/HSGPS filter. One reason for this is that only "good" quality DGPS data is normally used for the measurement updates of the system filter. However, when using HSGPS data (usually of poor quality) the situation is not quite the same. Let us first analyze the timing of both PDR and GPS systems.

A pedestrian walking timing diagram can be pictured as shown in Figure 7.1. Suppose the user has made a step. The times of the steps are denoted as t_{PDR}^j and t_{PDR}^{j+1} respectively. Also, the times of 3 GPS updates are shown in the diagram, that is t_{GPS}^i, t_{GPS}^{i+1} and t_{GPS}^{i+2}. These steps and GPS times will be referred to as PDR and GPS epochs respectively. Let us assume that these PDR and GPS epochs do not coincide in time. During normal walking, step frequency is normally less than 2 Hz. With this step frequency, the user can make nearly 2 full steps between the possible GPS epochs. Considering the situation shown in Figure 7.1, which of the 3 times, that is t_{PDR}^j, t_{GPS}^{i+1} or t_{PDR}^{j+1}, should be taken as a filter time, that is to provide the position (and other available) output. The term *filter time* will thereafter refer to the time when the integrated system will provide the output.
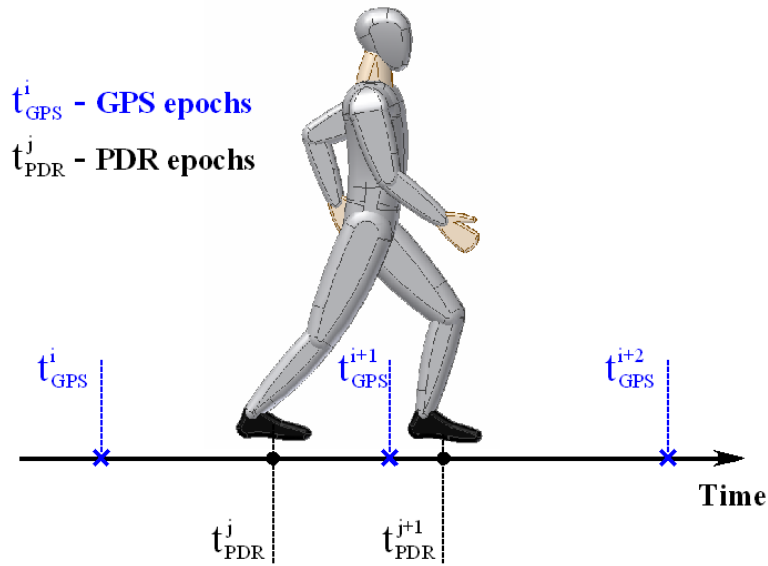
Figure 7.1: Pedestrian Walking Time Diagram

The HSGPS errors might be large in all three consecutive GPS epochs shown in the figure. Therefore, the GPS epoch times must be taken as the filter times, since it is impossible to interpolate such HSGPS data to fit the PDR epoch times. Therefore, time t_{GPS}^{i+1} must be taken as the filter update time. For this filter epoch, the PDR data must be extrapolated from time t_{PDR}^{j} to time t_{GPS}^{i+1}, since the time of the next step, t_{PDR}^{j+1}, is not yet known. If no GPS epoch exists between the PDR epochs t_{PDR}^{j} and t_{PDR}^{j+1}, the step user epoch t_{PDR}^{j+1} must be taken as the filter time. In this case, the filter propagates in the prediction mode, with no GPS updates yet available. This method of filter time base selection potentially allows the system to run in real time[1], since no future information is used.

However, this method may frequently result in an unnecessarily high solution output rate, especially when the user has a high step frequency. If the user makes more than

[1]Term "real time" here refers to a theoretical concept and does not take into account the computational load which is hard to assess for various mobile hardware implementations

one full step between GPS epochs (that is during one second) the filter does not wait for the GPS update in this mechanization, and it will output the solution at the time of the last detected user. If the GPS update becomes available a fraction of a second later, the filter will run once again. Essentially, an output position rate higher than 1 Hz is not required for a pedestrian user. The filter can therefore run with a small time lag according to the following proposed algorithm.
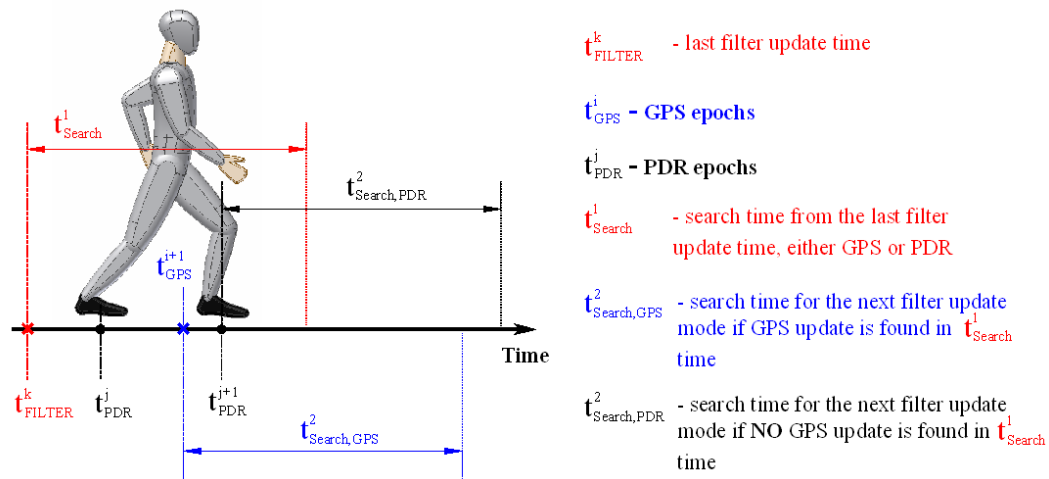

Figure 7.2: Filter Update Time Search Algorithm

After the last filter epoch time, whether it was a PDR epoch (step time) or a GPS epoch, the filter algorithm waits t^1_{Search} seconds for a GPS epoch. If the GPS solution becomes available during this time period, then the GPS epoch, t^{i+1}_{GPS}, is taken as the filter time. After that, the search for the next GPS update with respect to this detected GPS epoch is carried out. This search time is shown in Figure 7.2 as $t^2_{Search,GPS}$. If no GPS update becomes available during the initial search time t^1_{Search}, the algorithm goes back in time to the last detected step, that is t^{j+1}_{PDR} in this case, and runs the filter in prediction mode from the last filter epoch to this PDR epoch. The search time i$t^2_{Search,PDR}$ is then carried forward with respect to this last

PDR filter time.

In this algorithm, if GPS updates are available every second, the filter runs on the GPS epoch times. In this case, the PDR data must be extrapolated to be input into the filter. When the GPS data is not available, the filter cannot find any GPS updates and runs in PDR-only mode, that is in prediction mode. In this mechanization, when GPS data is always available, the filter runs in real time. When the filter runs in prediction mode, a small time lag is introduced by allowing the filter to search longer for a possible GPS update after a step is detected. The time lag in this case is small, and for the situation pictured in Figure 7.2 it can be found according to

$$T_{lag} = t_{Search}^1 - \left(t_{PDR}^{j+1} - t_{Filter}^k\right) \tag{7.1}$$

where

T_{lag} ... is the filter lag time when in prediction mode, and

t_{Search}^1 ... is the filter search time for a GPS update, and

t_{PDR}^{j+1} ... is the time of the $(j+1)$ detected step, and

t_{Filter}^k ... is the previous filter epoch time.

With the highest data rate of 1 Hz HSGPS, the search time t_{search} can be given as slightly larger than 1 second, as 1.1 seconds. For a user step frequency of 2 Hz, the longest filter time lag in this case is approximately 0.6 seconds. It should be noted that this time lag is just a computational delay from the real-time application and has nothing to do with the timing synchronization of the PDR and GPS data. This method introduces a small computational time lag that is not crucial for this application, but it makes it possible to optimize the filter solution output rate and run the filter at the correct times.

7.1.2 Integrated System Filter Modes

All possible pedestrian signal scenarios for which the integration filter should be run in slightly different mechanizations are shown in Figure 7.3.
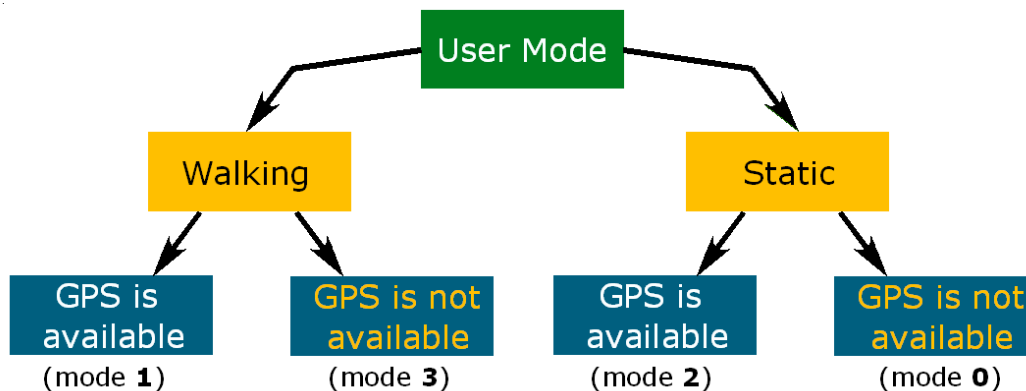

Figure 7.3: Pedestrian Motion States and GPS Availability Scenarios

In each of these scenarios, the mechanization strategy of the PDR/HSGPS integration filter must be different. The important parameters and the filter timing strategy for each of the scenarios are the following[2]):

Walking, GPS is available (mode 1). The filter time is based on the GPS epoch times. The PDR data is used to propagate the solution forward (filter prediction mode) and the HSGPS data is used for the filter updates (measurement update mode). The solution is obtained in real-time.

Walking, GPS is not available (mode 3). The filter time is based on user step times. The sensor data is used to propagate the solution forward in pure prediction mode. In this mode, a small time lag due to the search of GPS updates is introduced.

---

[2]Modes are numbered for easier reference to them in figures

Static, GPS is available (mode 2). In this mode, several processing options exist. Since, the PDR algorithm detects that the user is static, the position may not be propagated forward. This is essentially one of the biggest advantages of the PDR mechanization. Also, since GPS data is available, the filter may continue running. In this case, the filter will not be propagated in the prediction mode since the user is detected to be static. Also, the batch processing techniques can be applied to the GPS data for this case (Mezentsev, 2004).

Static, GPS is not available (mode 0). When the user is static and no GPS data is available, the filter does not run and maintains the last computed state vector. Only the attitude of the PDR system may be updated depending on the status of the detected step (Section 5.2).

Considering the harsh signal environment, when the user is static it is best not to update the position in mode 2 with the available HSGPS data. With GPS data of such poor quality, one should attempt to limit the influence of the outliers as much as possible. The detection of static user condition is one of the biggest advantages of using self-contained sensors and should be used to the user's benefit. Therefore, the integration filter must run only in modes 1 or 3 when the user is walking. The filter step time between epochs (i) and $(i + 1)$ will be different for different modes and can be computed as

$$
\begin{aligned}
\textbf{Mode 1:} \quad \Delta t &= t_{GPS}^{i+1} - t_{GPS}^{i} \\
\textbf{Mode 3:} \quad \Delta t &= t_{PDR}^{i+1} - t_{PDR}^{i} \\
\textbf{Modes 1 and 3 transition:} \quad \Delta t &= \left| t_{GPS|PDR}^{i+1} - t_{GPS|PDR}^{i} \right|
\end{aligned}
\tag{7.2}
$$

where

Δt ... is the filter step time.

7.1.3 State Vector Modeling

As has been discussed earlier in this thesis, we are only concerned with the horizontal position coordinates in the integrated system. The height component of the solution is propagated with the low-cost barometer in differential mode after it is initialized by a reliable 3D coordinate fix from GPS. Therefore, only two coordinate variables must be present in the state vector: Easting and Northing. Among the user attitude parameters, the user heading is of only practical interest. The ISA gyro and accelerometer biases cannot be estimated without good quality HSGPS data in an environment such as a downtown area (Mezentsev et al., 2004).

In the PDR mechanization, the step-length parameter essentially represents the speed of the user since the time between the user steps is known. For the discrete Kalman filter, the discrete parameter of the step length is thus an optimal choice. Generally speaking, it should be noted that the step-length parameter refers to the distance walked by a user between the filter epochs. In mode 1, when GPS epoch times are chosen as the filter time base, the user may make more than one step. In this case, the step-length variable can be called epoch-to-epoch walking distance. In mode 1, it is assumed that during one second, the user walking path is straight, which is a reasonable assumption considering the small filter step time. Besides, the heading is propagated without any approximations, so this assumption may slightly affect only the distance traveled by a user. Therefore, it is best to include the following parameters in the state vector: Easting - $\mathbf{E}$, Northing - $\mathbf{N}$, Step length (or epoch to epoch distance) - $\mathbf{S}$, Heading - $\mathbf{H}$ and Heading rate - $\mathbf{HR}$. The state vector can therefore be written as

$$[\mathbf{x}] = \begin{bmatrix} \mathbf{E} & \mathbf{N} & \mathbf{S} & \mathbf{H} & \mathbf{HR} \end{bmatrix}^T \tag{7.3}$$

The PDR measurements are essentially the detected steps and the measured user-

heading rate. Provided you have the step length (carried from the previous filter epoch), the position and the heading of the user may be propagated. The PDR mechanization equations are non-linear; therefore, the linearized Kalman filter must be used. It is best to use the filter mechanization scheme shown in Figure 7.4.
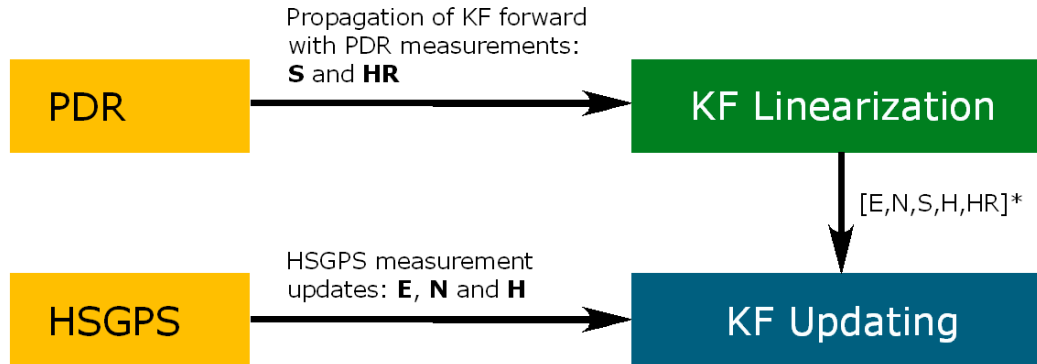

Figure 7.4: PDR/HSGPS Linearized Kalman Filter Scheme

In this scheme, the propagation of the filter forward (linearization point) is computed based on the PDR measurements, meaning the number of user steps detected between the filter epochs and the measured heading rate. GPS Easting, Northing and Heading are taken as the filter update measurements whenever they are available. Only three states of the state vector are thus directly observable. As will be shown later in this chapter, the overall system is still observable.

In navigation, one of the common methods to determine the heading is the use of GPS velocities and is given by

$$\mathbf{H}_{t_k} = \arctan\left(\frac{V_{E,t_k}}{V_{N,t_k}}\right) \tag{7.4}$$

where

$\mathbf{H}_{t_k}$ ... is the estimated heading at time t_k, and

V_{E,t_k} ... is the East GPS velocity at time t_k, and

V_{N,t_k} ... is the North GPS velocity at time t_k.

An important limitation that comes into play when this method is applied to pedestrian navigation is low-pedestrian velocity. Normally, pedestrian velocity almost never exceeds 2 m/s. Let us suppose accurate open-sky GPS velocity measurements are available with a standard deviation of 3 cm/sec. Now, suppose a user is walking east with a velocity of 1.4 m/s. The heading determined using the simulated GPS measurements with the above statistical parameters is shown in Figure 7.5. As can be seen from this figure, this heading has a standard deviation error of about 7 degrees! If the heading is estimated using a Kalman filter, the estimate will eventually converge to the true value if you have good-quality unbiased GPS measurements. Obviously, this method won't work when the user is static. The heading derived from the GPS velocities is still far more accurate than the heading derived from consecutive GPS position estimates since the multipath affects Doppler measurements less than the code measurements.

In a signal-degraded environment, the accuracy of the GPS velocity determination is additionally degraded. However, for an independent system that does not rely on many assumptions, this is practically the only means available for the heading updates. In this work, the initial heading of the user is obtained by using this method after the first available GPS solution when walking. The appropriate variance must be associated with the heading-derived value. In an open-sky environment, this variance can therefore be taken as 7^2 deg^2. Based on the experimental data, in a downtown area this value needs to be increased to about 30^2 deg^2.
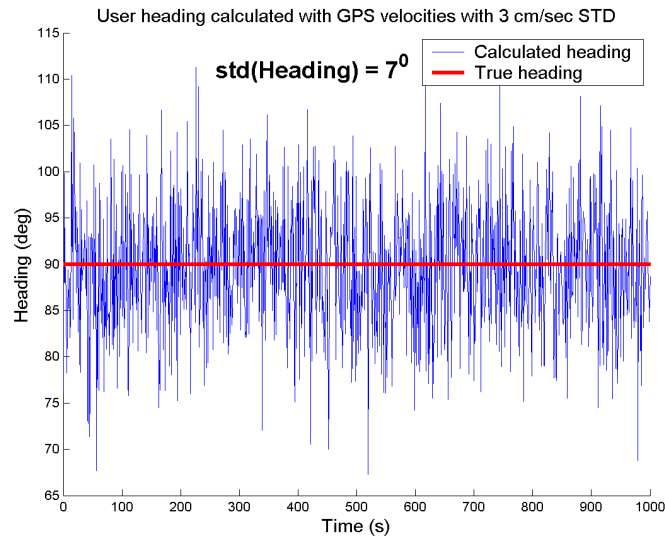
Figure 7.5: User Heading Determined Using GPS Velocities. The Data Is Simulated for User Speed of 1.4 m/s, Direction of Walking: East, STD of GPS Velocities = 3 cm/sec

7.2   Kalman Filter Design

For the chosen state vector, the discrete kinematic PDR equations can thus be written as

$$
\begin{aligned}
\mathbf{E}_{i+1} &= \mathbf{E}_i + \mathbf{S}_i \cdot \sin\left(\mathbf{H}_i\right) \\
\mathbf{N}_{i+1} &= \mathbf{N}_i + \mathbf{S}_i \cdot \cos\left(\mathbf{H}_i\right) \\
\mathbf{H}_{i+1} &= \mathbf{H}_i + \bar{\mathbf{HR}}_{i,i+1} \cdot \Delta t
\end{aligned}
\tag{7.5}
$$

where

$\bar{\mathbf{HR}}_{i,i+1}$ ... is the average heading rate over the filter step size.

The step length, $\mathbf{S}$, and the heading rate, $\mathbf{HR}$ variables are random processes and

are thus modeled stochastically. Modeling of these stochastic variables for MEMS ISA and pedestrian navigation has been discussed in Chapter 5. The heading rate is modeled as a random walk process, thus the heading will be an integrated random walk process that accurately represents the real PDR heading drift. The step length is also modeled here as a random walk process. The chosen random walk stochastic models for the step length and the heading rate variables are given by

$$
\begin{aligned}
\mathbf{S}_{i+1} &= \mathbf{S}_i + \mathbf{w}_s; \qquad \mathbf{w}_s \sim N(0, \sigma_s) \\
\bar{\mathbf{HR}}_{i+1} &= \bar{\mathbf{HR}}_i + \mathbf{w}_{HR}; \qquad \mathbf{w}_s \sim N(0, \sigma_{HR})
\end{aligned}
\tag{7.6}
$$

One important note must be made here. In the system equations, the average heading rate during the step time of the filter is taken. Modeling of this variable by a random walk process is still perfectly valid since the integration time is not very significant. This system of equations is nonlinear with respect to the system variables; therefore, the linearized Kalman filter mechanization is used.

The linearized transition matrix, $\mathbf{\Phi}^*_{t_k, t_{k+1}}$, for the time interval $[t_k; t_{k+1}]$, can be computed according to

$$
\mathbf{\Phi}^*_{t_k, t_{k+1}} =
\begin{bmatrix}
1 & 0 & \sin\left(\mathbf{H}_{t_k}\right) \cdot \Delta t & \mathbf{S}_{t_k} \cdot \cos\left(\mathbf{H}_{t_k}\right) \cdot \bar{\mathbf{HR}}_{t_k, t_{k+1}} \cdot \Delta t & 0 \\
0 & 1 & \cos\left(\mathbf{H}_{t_k}\right) \cdot \Delta t & -\mathbf{S}_{t_k} \cdot \sin\left(\mathbf{H}_{t_k}\right) \cdot \bar{\mathbf{HR}}_{t_k, t_{k+1}} \cdot \Delta t & 0 \\
0 & 0 & 1 & 0 & 0 \\
0 & 0 & 0 & 1 & \Delta t \\
0 & 0 & 0 & 0 & 1
\end{bmatrix}
\tag{7.7}
$$

The state transition matrix is calculated every epoch based on what the state vector values are in the previous epoch. The process noise matrix, $\mathbf{Q}_{t_k, t_{k+1}}$, is discrete since it is defined for the discrete stochastic variables. The value of the step-length variance is assigned according to the uncertainty in the pedestrian walking model.

The heading rate variance is assigned according to the heading rate drift model for a given accuracy ISA. The process noise matrix can thus be composed as shown

$$\mathbf{Q}_{t_k, t_{k+1}} = \mathbf{diag}\left(\begin{bmatrix} 0 & 0 & \sigma^2_{s,t_k} & 0 & \sigma^2_{HR,\Delta t} \end{bmatrix}\right) \tag{7.8}$$

where

σ^2_{s,t_k} ... is the variance of the step length at t_k, and

$\sigma^2_{HR,\Delta t}$ ... is the variance of the heading rate PDR measurement for Δt filter step time.

The filter propagates forward from the previous optimal state vector values (prediction) based on the PDR measurements. Therefore, the linearized values of the state vector can be computed according to

$$[\mathbf{x}]^*_{t_{k+1}} = \mathbf{\Phi}^*_{t_k, t_{k+1}} \cdot \begin{bmatrix} 0 & 0 & \mathbf{S}_{t_k} & 0 & \bar{\mathbf{HR}}_{t_k, t_{k+1}} \end{bmatrix}^T \tag{7.9}$$

In the proposed mechanization, the HSGPS measurements need to be taken with respect to the state vector values at time t_k. The measurement vector can thus be computed as

$$[\mathbf{z}]_{t_{k+1}} = \begin{bmatrix} \mathbf{E}_{GPS, t_{k+1}} - \mathbf{x}^+_{t_k}(1) \\ \mathbf{N}_{GPS, t_{k+1}} - \mathbf{x}^+_{t_k}(2) \\ \mathbf{H}_{GPS, t_{k+1}} - \mathbf{x}^+_{t_k}(4) \end{bmatrix}^T \tag{7.10}$$

where

$\mathbf{E}_{GPS, t_{k+1}}$ ... is the HSGPS Easting at time t_{k+1} in a LL coordinate frame, and

$\mathbf{N}_{GPS, t_{k+1}}$ ... is the HSGPS Northing at time t_{k+1} in a LL coordinate frame, and

$\mathbf{H}_{GPS, t_{k+1}}$ ... is the HSGPS derived heading at time t_{k+1}, and

$\mathbf{x}^+_{t_k}$ ... is the optimal state vector estimate at the previous epoch.

The design matrix in this case can be written as

$$\mathbf{H} = \begin{bmatrix} 1 & 0 & 0 & 0 & 0 \\ 0 & 1 & 0 & 0 & 0 \\ 0 & 0 & 0 & 1 & 0 \end{bmatrix} \tag{7.11}$$

With this design matrix, $\mathbf{H}$, and the state transition matrix, $\mathbf{\Phi}^*_{t_k,t_{k+1}}$, the observability matrix (Equation 3.20) has full rank, which assures the observability of the system. The step length, $\mathbf{S}$, and the heading rate, $\mathbf{HR}$, are not directly observable states. The theoretical convergence of these states is achieved after the directly-observed states, that is $\mathbf{E}$, $\mathbf{N}$ and $\mathbf{H}$, are converged. A note must be made on the convergence of the heading rate. The heading rate is input to the filter from the PDR measurements and is averaged over the time of the filter step time, Δt. During this time, the actual heading rate may change a fair amount. Therefore, the convergence of the heading rate implies the convergence of the heading rate estimate averaged over the filter step time.

The measurement covariance matrix in traditional integration schemes is formed by the variances of the GPS measurements. The Easting and Northing coordinate variances are taken from the GPS LSQ adjustment. The heading variance is taken as the variance of the heading derived with the GPS velocities. Thus, the measurement covariance matrix can be formed according to

$$\mathbf{R} = \begin{bmatrix} Var\left(\mathbf{E}_{GPS,t_{k+1}}\right) & 0 & 0 \\ 0 & Var\left(\mathbf{N}_{GPS,t_{k+1}}\right) & 0 \\ 0 & 0 & Var\left(\mathbf{H}_{GPS,t_{k+1}}\right) \end{bmatrix} \tag{7.12}$$

Even in a signal-degraded environment, the estimated variances of the position solution after the LSQ adjustment may be quite small due to the lack of redundancy and possible multiple (correlated) blunders in a single epoch. The proper modeling of

the covariance of the measurements is essentially the key to a successful navigation solution in such environments. As will be shown in Chapter 8, such modeling of the measurement error covariance matrix as given by Equation 7.12 is not optimal in the real signal degraded environment.

It is proposed to use an alternative approach to modeling the measurement error covariance matrix based on the UERE parameter for a given environment and measured DOP parameters. As has been discussed in Chapter 6, UERE values can potentially be adjusted autonomously for a given environment and together with DOP values can represent the HSGPS errors better that the least squares residuals. The heading is not represented by the UERE value, since in this case it will be very large and the heading measurement will be largely de-weighted during the filtering. In this case, the $\mathbf{R}$ matrix can be formed as

$$\mathbf{R} = \mathbf{diag}\left(\begin{bmatrix} (UERE \cdot EDOP)^2 & (UERE \cdot NDOP)^2 & Var\left(\mathbf{H}\right) \end{bmatrix}\right) \qquad (7.13)$$

where

$UERE$ ... is the user equivalent range error for a given environment, and

$EDOP$ ... is the Easting dilution of precision, and

$NDOP$ ... is the Northing dilution of precision, and

$Var\left(\mathbf{H}\right)$ ... is the variance of the derived heading measurement.

The parameters of the measurements' covariance matrix will be discussed for every experimental result presented in the next chapter.

Once the state vector and all necessary matrices are modeled, the measurement update to the linearized state vector is computed according to

$$\Delta\left[\mathbf{x}\right]_{t_{k+1}} = \mathbf{K}_{t_{k+1}}\left(\left[\mathbf{z}\right]_{t_{k+1}} - \mathbf{H}\left[\mathbf{x}\right]^*_{t_{k+1}}\right) \qquad (7.14)$$

where

$\mathbf{K}_{t_{k+1}}$ ... is the Kalman gain matrix at the epoch of GPS update at time t_{k+1} and is computed according to Equation 3.11.

The final optimal estimate of the state vector at time t_{k+1} is computed as

$$[\mathbf{x}]_{t_{k+1}}^{+} = [\mathbf{x}]_{t_k}^{+} + [\mathbf{x}]_{t_{k+1}}^{*} + \Delta [\mathbf{x}]_{t_{k+1}} \tag{7.15}$$

The horizontal position accuracy of the filtered solution can be estimated from the error covariance matrix of the estimates, $\mathbf{P}$. The two first components of the state vector are estimated Easting and Northing user coordinates. Therefore, the distance root mean square (DRMS) error can be computed from the error covariance matrix and is given by

$$DRMS = \sqrt{\mathbf{P}_{t_k}^{+}(1,1) + \mathbf{P}_{t_k}^{+}(2,2)} \tag{7.16}$$

where

$\mathbf{P}_{t_k}^{+}$ ... is the updated error covariance matrix of the estimates at time t_k.

7.2.1 Pedestrian Trajectory Constraint

For pedestrian navigation, some additional constraints can be applied. In the experimental results chapter, it will be shown that the step-length estimates may reach significant values for several consecutive epochs. The step length is observed in the filter through the position variables and thus is also affected by the blunderous HSGPS measurements. The step-length values for an average person during normal walking hardly ever exceed 1 metre. In the designed filter, the step-length value to propagate the PDR position forward at epoch t_{k+1} is taken as the optimal estimate of the step-length estimate at the previous epoch, that is as $\mathbf{S}_{t_k}^{+}$. The following

(truly pedestrian) constraint can then be applied. If the estimated step-length value exceeds a certain threshold, then it is reset to the predefined constant value. This step-length bounding condition can be written as

$$\textbf{if} \quad \left| \mathbf{S}^+_{t_k} - \mathbf{S}_{thr} \right| > \delta_s; \quad \textbf{then,} \quad \mathbf{S}^-_{t_{t+1}} = \mathbf{S}_{thr} \qquad (7.17)$$

where

$\mathbf{S}^+_{t_k}$ ... is the step length estimate at epoch t_k, and

$\mathbf{S}_{thr}$ ... ia a constant step length, and

δ_s ... is the step length threshold value.

The value of $\mathbf{S}_{thr}$ can be seen as the assumed average step-length value, which can be calibrated in the area with good GPS visibility or simply assumed constant. In the step-length calibration in the open sky environment is not available, for an average person walking normally, this parameter can be taken as 0.7 metres (Collin et al., 2003b). The value of the threshold, δ_s, can be seen as the 1σ deviation of the averaged step length from the true step-length values for a given stochastic error model. This approach of bounding the step length is later referred to as step-length limiting. This is a valid constraint to apply considering the poor quality of the GPS data and the proposed random-walk model for step-length error.

The next section will discuss the reliability testing issues of the integrated solution and its applicability to the real environment.

7.3   Reliability Testing of the Integrated Solution

Similar to the RAIM algorithm that is applicable to GPS data, a statistical test can be performed on the Kalman innovation sequence to detect an inconsistency between

the model prediction and the measurement update. The normalized sum of the squared innovations (SSI) affected by a blunder should belong to the χ^2 distribution with the non-centrality parameter mean (Ryan, 2002) and can be written as

$$\mathbf{SSI} = \nabla^T \cdot \mathbf{P}_{t_{k+1}}^+ \cdot \nabla \tag{7.18}$$

where

$\mathbf{P}_{t_{k+1}}^+$ ...   is the updated covariance matrix of the estimate vector, and

∇ ...   is the vector containing a blunder.

This is similar to RAIM algorithm testing and can then be applied to SSI with the chosen parameters of α and β for the false alarm and false rejection rates. The same assumption here must hold, that is the presence of only one blunder component in the ∇ vector at a time. Considering the signal environment, such an assumption clearly will not hold, as has been seen in the case of the RAIM applied directly to the HSGPS data. The largest measurement blunder in the measurement update vector cannot be rejected because, in this case, the system will become unobservable. If the inconsistency is detected, the whole vector of measurements must then be rejected.

This brings up another significant problem with the application of this method to the integrated solution. If numerous consecutive measurements are rejected based on the testing of the SSI, the system will propagate the solution only in the PDR mode. In this case, the error covariance matrix of the estimated state vector will grow. This may eventually force such integrity testing to accept a blunderous measurement that will decrease the error covariance matrix of the solution. This, in turn, will increase the probability that later an accurate solution will not be accepted, as the solution will be affected by a significant blunder that "dragged" the solution vector away from the true values.

In other words, this method may in fact be more dangerous when compared to the RAIM method applied directly to the HSGPS data. When two systems are used in the integrated solution, it is simply not known which of the individual system solutions, that is either the propagation or the measurement update, contains an error. This uncertainty only grows when numerous rejections are made based on the statistical testing of the SSI parameters.

Therefore, one should perform statistical testing on the HSGPS data only, as has been described in the previous chapter. In chapter 8), it will be noted in each case what type of RAIM algorithm has been applied to the HSGPS data before it is input into the Kalman filter in the form of measurement updates.

7.4   Practical Considerations

Initialization of any integrated navigation system is a major concern which frequently forces us to introduce and rely on various assumptions. For an independent (and, most importantly, practical) system, any assumption is a nuisance that frequently diminishes the advantages gained by the proposed algorithm. Imagine a pedestrian navigation system manual instructing us to first find a spot with a clear view of the sky, and then remain there for 10 minutes in order to navigate. Clearly, it is highly unlikely that this product will be of much interest to anyone.

When it is first turned on, any dead reckoning system operation first has to obtain an initial absolute position (and attitude) fix from GPS. If the system is started in a very harsh signal environment (or even indoors) and no GPS is available, then no output can be provided. Potentially, the only output the PDR system can provide is the step count, and nothing more. Once a reliable (after RAIM algorithm) HSGPS solution becomes available, the filter must be initialized to these values since no other means

of initialization is available. If this position fix happens to be an undetected outlier, it may take a long time to recover the integrated solution before it returns to the true position proximity. In fact, poor position initialization is another negative aspect for the application of the reliability analysis to the integrated solution. The user heading is calculated from the HSGPS velocities only when the PDR system detects that the user is walking. The initial covariance matrix can therefore be directly assigned from the HSGPS data and the uncertainty in the PDR model parameters, step length and heading rate.

7.4.1 PDR Data Interpolation

In filter **mode 1** (walking, GPS is available), the GPS epoch times are chosen as the filter epochs, with, essentially, 1 second intervals. Since the user may make more than 1 full step during this second, the PDR data-heading rate needs to be averaged. The heading rate measurement, $\bar{\mathbf{HR}}_{t_k,t_{k+1}}$, used to propagate the filter forward can be computed as

$$\bar{\mathbf{HR}}_{t_k,t_{k+1}} = \frac{\int_{t_k}^{t_{k+1}} \mathbf{HR}\left(t\right) dt}{t_{k+1} - t_k} \tag{7.19}$$

where

$\mathbf{HR}\left(t\right)$ ... is the heading rate of the user computed with higher rate from the PDR data, usually, with 20 Hz or higher.

Also, in **mode 1**, a portion of the step length that the user has made before the filter epoch time needs to be taken into account (Section 7.1.1). Between the update epochs the user is assumed to be walking with a constant step length. The assumption of the random walk step-length model implies that without measurement updates the best estimate is the previous step-length value. This portion of the step

can be approximated as (Figure 7.1)

$$\Delta \mathbf{S} = \frac{t_{GPS}^{i+1} - t_{PDR}^{j}}{t_{PDR}^{j} - t_{PDR}^{j-1}} \cdot \mathbf{S}_{t_k} \tag{7.20}$$

All partial and whole user step-lengths need to be summed up to be input into the filter propagation loop. The assumption of a constant step-length model during one epoch length does not introduce significant error, due to the small filter step size in this mode, which is one second. If some additional step-length measuring techniques were available, such as shoe-mounted inertial (Stirling et al., 2005) or RF (Brand and Phillips, 2003) sensors, step-length modeling and estimation could be made more accurate.

7.5 Simulation Analysis

In order to verify and demonstrate the performance of the developed PDR/GPS Kalman filter, a simulation analysis needs to be carried out. A simulated true pedestrian trajectory with respect to this analysis is performed as shown in Figure 7.6. The trajectory consists of eight straight segments with 600 full steps performed by the user. Also, a 35-second stop is simulated and is shown in the upper left corner of the trajectory. Figure 7.6 also shows the number of steps performed by the user in every straight portion of the trajectory. While the user is walking, two simulated GPS date gaps are shown in two different colours along the trajectory. The total walking time is equal to 455 seconds. The parameters of the simulated PDR and GPS data are summarized in Table 7.5.

The simulation of the data gaps is performed to demonstrate the PDR solution drift over the time intervals when GPS is unavailable. In reality, the GPS outage is usually preceded by the sudden or gradual degradation of DOP and increased

noise and multipath effects. All these effects can cause the last GPS update before the data gap to be erroneous that accordingly affects the errors of the PDR-only solution. Such situations will be better shown on the real field data rather than the simulations.

Figure 7.6: Simulated Test Trajectory

The simulated PDR and GPS trajectories and position estimated by the PDR/GPS filter when no GPS data gaps and no GPS outliers are simulated, are shown in Figure 7.7. The simulated PDR trajectory is computed assuming the known initial heading to demonstrate how the PDR-only solution drifts over time without any GPS updates. As can be seen from the results of this figure, the estimated trajectory is fairly accurate and follows the true simulated trajectory very well. This is due to the fact that accurate GPS data is available along the entirety of the walking path.

Table 7.1: Summary of Simulated PDR and GPS data for The Simulation Analysis

Test Length:	600 steps; ≈400 metres loop; 455 seconds
PDR Step Length:	0.7 metres
PDR Step Length Error:	0.1 metres (1σ)
PDR Heading:	Integrated Random Walk with 300 deg/h bias
GPS Positions Errors:	2.2 metres (1σ)
GPS Velocity Errors:	3 cm/sec (1σ)
GPS Positions Outliers:	during [300; 330], 30 metres Easting bias
GPS Data Gaps:	between [55; 155] and [330; 420] seconds

Figure 7.8 shows the true, simulated and estimated step lengths, heading and heading rate parameters of the user. The root-mean square (RMS) errors of the estimated parameters with respect to the true simulated values for the whole test are given in Table 7.5. The poor estimates of the step length and, especially, the heading rate are mostly due to the fact that these parameters are not directly observable. The GPS data is fairly accurate (2.2 m 1σ), but it still represents a code solution and thus is quite scattered around the true path. Therefore, the position updates frequently occur "behind" the propagated position based on the PDR data. This makes the convergence of the step-length parameter to a centimetre value practically impossible. During the sharp user turns, the heading rate estimate is poor due to the averaging of the heading rate measurement (section 7.4.1) and due to the estimated time lag of the Kalman filter.

Table 7.2: RMS Errors of the Estimated Results for Test 1

DRMS Position Error:	**1.2 metres**
RMS Step Length Error:	0.35 metres
RMS Heading Error:	**0.15 rad**
RMS Heading Rate Error:	0.4 rad/sec

The Kalman filter modes are shown in Figure 7.8. In this simulation, the filter operates only in Mode 1 (Walking, GPS Available) and Mode 2 (Static, GPS Avail-
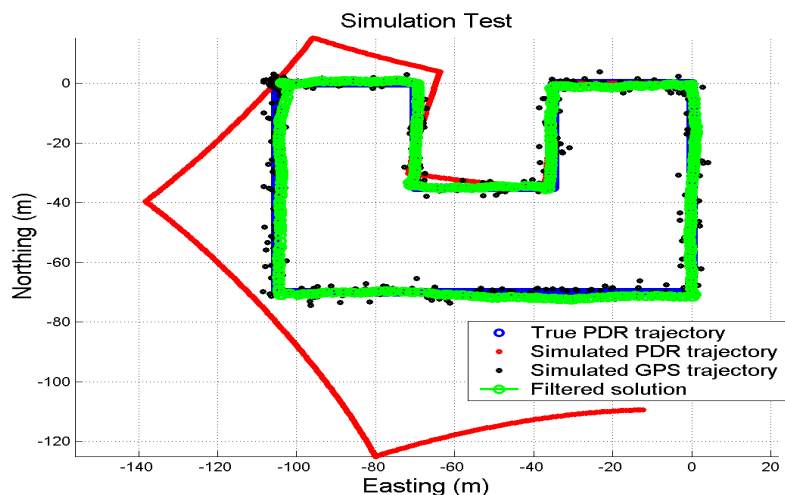
Figure 7.7: Test1. Simulated PDR and GPS Trajectories and the PDR/GPS Filtered Solution: No GPS Data Gaps and No GPS Outliers

able). During the whole simulation, the filter runs on GPS time, since GPS is always available.

In the next simulation, two GPS data gaps are simulated. The time periods of these GPS data gaps are given in Table 7.5. The filter switches to mode 3 (Walking, No GPS) during the GPS gaps. In this mode, the solution is propagated in a pure PDR mode. This prediction is based on the last estimated step length and heading parameters when GPS was available. The heading rate and the step count are the only measurements available from the PDR system during this time. Figure 7.9 shows the simulated PDR trajectory, the simulated GPS trajectory and the result of PDR/GPS filtering when two GPS data gaps are simulated. Figure 7.10 shows the true, simulated and estimated step lengths, heading and heading rate parameters of the system for this simulation.

In this simulation, the estimation accuracy is poorer than in the previous case where
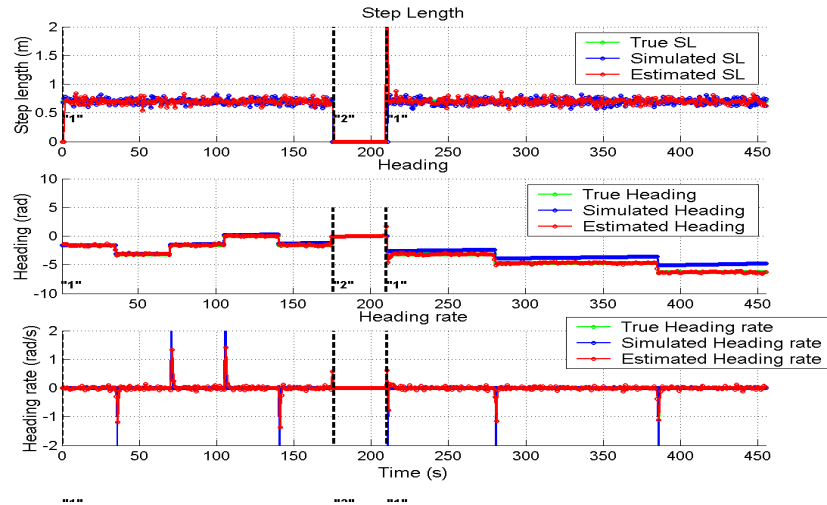
Figure 7.8: Test 1. Simulated and Estimated Step Length, Heading and Heading Rate Parameters: No GPS Data Gaps and No GPS Outliers

there were no GPS gaps. The DRMS errors in the estimated parameters with respect to the true simulated values are given in Table 7.5. In this case, the position DRMS error is equal to 10 metres. The largest 2D error is equal to 30.8 metres and happens at the end of the second data gap. Considering the time of the gap, almost 100 seconds, this error is still very small considering the quality of the simulated gyros (300 deg/hour equivalent biases). In this test, the filter runs in a total of 3 modes, that is Mode 1 (Walking, GPS Available), Mode 2 (Static, GPS Available), and Mode 3 (Walking, No GPS).

Table 7.3: RMS Errors of the Estimated Results for Test 2: Two GPS Data Gaps are Simulated

DRMS Position Error:	**10.2 metres**
RMS Step Length Error:	0.33 metres
RMS Heading Error:	**0.6 rad**
RMS Heading Rate Error:	0.43 rad/sec
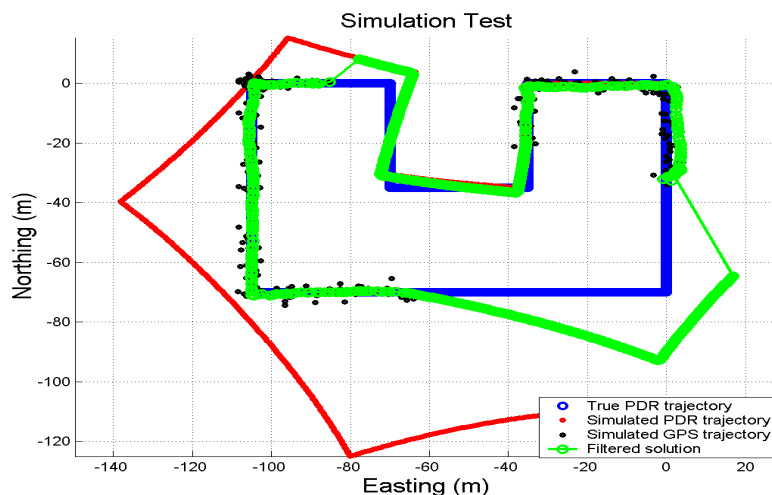
Figure 7.9: Test 2. Simulated PDR and GPS Trajectories and the PDR/GPS Filtered Solution: Two GPS Data Gaps are Simulated

In the next simulation (Test 3), the presence of several consecutive GPS position outliers is simulated (Table 7.5). The position accuracy of these outliers remains the same for all other position GPS solutions, that is 2.2 m 1σ. This demonstrates how the filter reacts to the presence of blunders with poor accuracy estimates. Figure 7.11 shows the simulated PDR trajectory, the simulated GPS trajectory and the results of PDR/GPS filtering when 30 consecutive outliers are present in the GPS data. Figure 7.12 shows the true, simulated and estimated step length, heading and the heading rate parameters of the system for this simulation. The RMS errors of the estimated parameters with respect to the true simulated values are given in Table 7.5.

In this case, the effect of these outliers on the filter estimates is not very significant. This is due mostly to the fact that the outliers occur after a relatively long period of time when good GPS data is available. In this case, the covariance matrix of
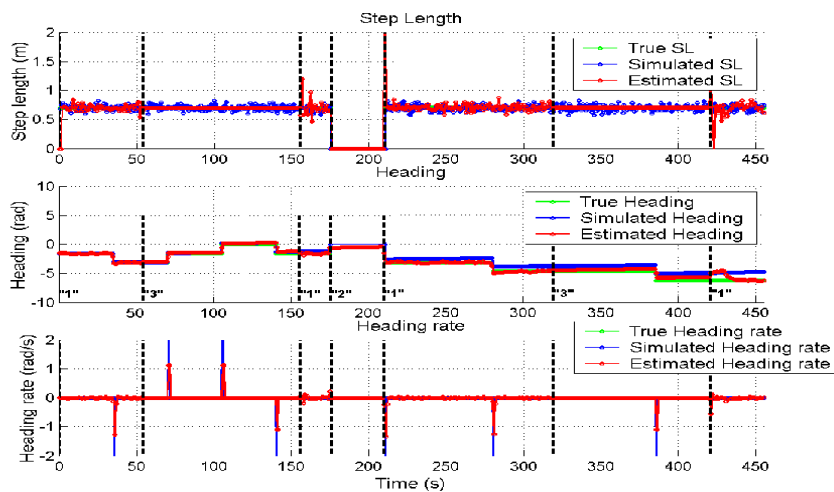
Figure 7.10: Test 2. Simulated and Estimated Step Length, Heading and Heading Rate Parameters: Two GPS Data Gaps are Simulated

Table 7.4: RMS Errors of the Estimated Results: GPS Outliers are Simulated

DRMS Position Error:	**2.1 metres**
RMS Step Length Error:	0.36 metres
RMS Heading Error:	**0.21 rad**
RMS Heading Rate Error:	0.46 rad/sec

the estimates is small, and these GPS blunderous position updates do not affect the Kalman gain matrix much. This situation is very different from the situation in Test 2, when GPS data gaps are simulated. In Test 2, when the system navigates in PDR (prediction) mode during the data gap, the PDR errors grow with the estimation covariance matrix, and when the GPS update becomes available, the states rather quickly converge to the GPS values (as can be seen in Figure 7.9 when the position quickly jumps to the first available GPS update).

The outliers, even consecutive, do not affect the steady filter performance much. On the contrary, outliers present a great challenge when they take place at the end
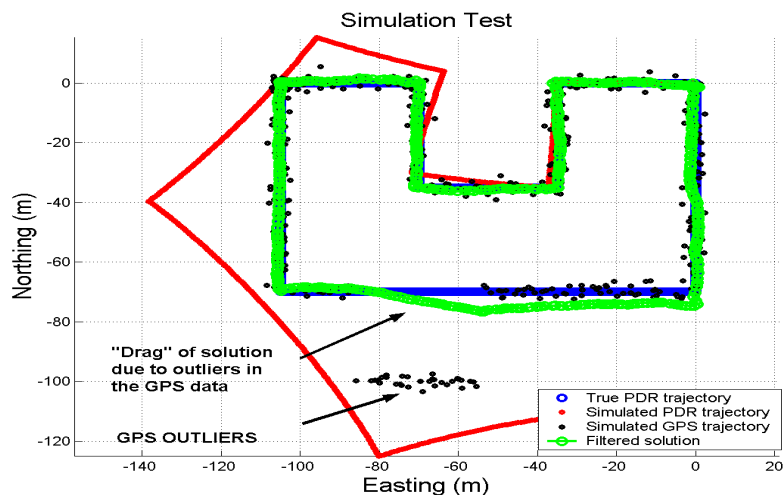
Figure 7.11: Test 3. Simulated PDR and GPS Trajectories and the PDR/GPS Filtered Solution: GPS Outliers are Simulated

of the PDR-only navigation period. The longer this period, the larger the effect of a potential outlier on the estimated parameters. This situation (a possible GPS outlier after a certain PDR-only navigation) presents one of the biggest challenges in PDR/HSGPS Kalman filtering in downtown areas. The largest problem lies in the proper covariance modeling. If the designed model and filter do not rely on many assumptions, this situation is nearly impossible to resolve. After a long PDR-only navigation, a GPS position update may be nowhere near the current PDR estimate. The fact is, one cannot know whether it is a good GPS update or a blunder due to the large element of uncertainty after PDR-only navigation.

7.5.1 Experimental Results in Open Sky Environment

In order to show the functionality of the filter on the field data, the filtering is applied to the data collected in an open sky environment. The test has been performed in an
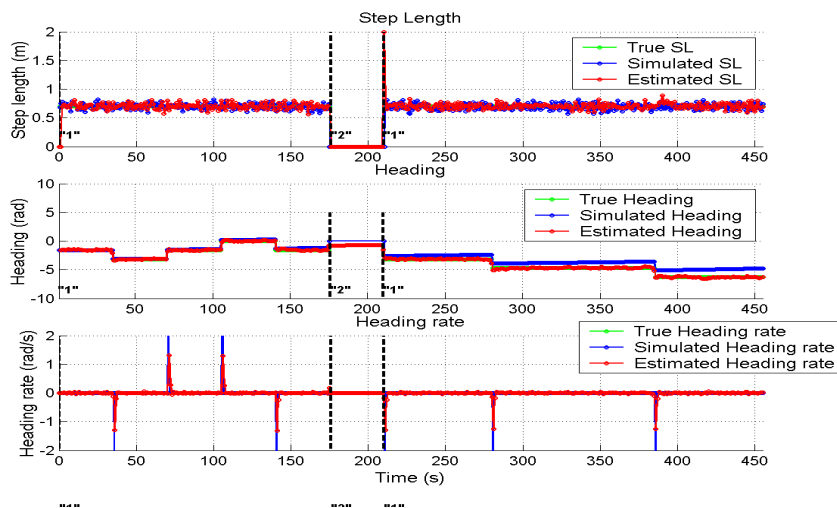
Figure 7.12: Test 3. Simulated and Estimated Step Length, Heading and Heading Rate Parameters: GPS Outliers are Simulated

open sky parking lot. In this environment, no GPS data gaps and no large outliers are present in both position and velocity domains. The test description and the PDR data of this test have been described and demonstrated in Section 5.3. Figure 7.13 shows the LSQ HSGPS data and the Kalman filtered solution of this test.

In this case, the HSGPS measurement covariance matrix is formed based on the variances of the LSQ solution. As can be seen from the results of this figure, the filtered solution is smoother and well approximates the truth trajectory that has been walked by a test person. In such good GPS signal environment, filtering of the GPS data is not problematic and a smooth trajectory can be obtained with the proposed filter.
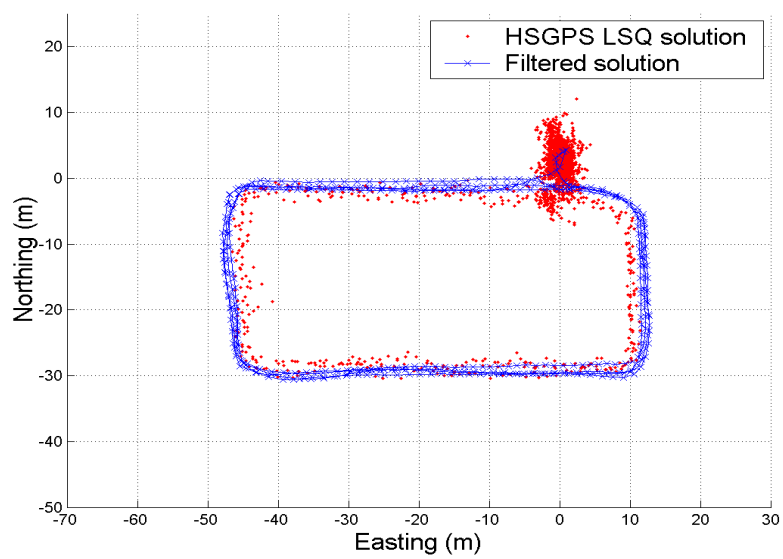
Figure 7.13: Results of Kalman Filtering of the Open Sky HSGPS Data

Chapter 8

Experimental Results

In this chapter, the experimental results of the sensor-aided HSGPS pedestrian navigation system in signal-degraded, downtown areas are presented.

8.1 Experimental Analysis Approach

To analyze the performance of the proposed PDR/HSGPS integration algorithm, numerous field tests have been conducted. In this chapter, an analysis is carried out on four statistically representative pedestrian walking tests. All tests have been performed in the Calgary downtown core environment. A description of downtown Calgary is given in Chapter 6 on the analysis of stand-alone HSGPS performance.

It seems that the PDR system provides many advantages in filtering the HSGPS data. In a good GPS-signal environment, such as an open sky, this is certainly true. The GPS-obtained trajectory can be smoothed through the process of integration with the PDR system, as has been shown in the simulation analysis section of the previous chapter. Rarely (or never) occurring GPS outliers or GPS data gaps make the situation practically problem-free for the PDR/GPS filter. Essentially, in a good GPS-signal environment, sensor aiding is not needed at all since it cannot improve the absolute accuracy of the system; it can only improve the relative precision of the results. Data from a self-contained sensor unit is truly needed in signal-degraded areas, where this unit can aid in filtering out large position blunders that may not be detected by autonomous GPS integrity-monitoring algorithms such as RAIM.

Throughout this thesis, it has been shown that the pedestrian dead reckoning algorithm provides a great advantage for people navigating on foot. However, it is important to remember that this system is a relative navigation system like any other inertial-based navigation system. Also, a PDR system based on low-cost MEMS inertial sensors has very large gyro bias drift rates ($\sim 300 \ deg/h$) that without accurate GPS updates simply cannot be estimated. The proposed methodology and the analysis presented in this thesis, and the results shown in this chapter, do not rely on many assumptions that would make the system ad-hoc and the results quite useless. In research analysis, a fine-tuning of Kalman filter parameters for every testing scenario is frequently performed in order to obtain better results in post-mission analysis. This approach can certainly improve the results on a test-to-test basis, but it cannot really be considered practical and worth investigating. In this chapter, no particular assumptions or filter tuning for each test are used that would jeopardize the applicability of this system for a real-world application. Even though the analysis is performed in post-mission mode, no future information of any kind is used. In addition, no assumptions, such as *we know it is an outlier because we see it on the map as an outlier*, or fine-tuning of the filter using apriori information about the environment will be used. Some constraints still need to be introduced; they will be discussed below.

Two of the goals of this thesis are as follows: first, to demonstrate what degree of accuracy can be achieved in the very poor signal conditions of a downtown area; and second, to show how well the accuracy of the solution can be estimated using two very low-cost and low-maintenance independent systems. By low-maintenance it is meant that the HSGPS solution is obtained in a single-point mode without any differential corrections. The low-cost and low-maintenance sensor unit implies a small sensor unit that can be attached to the user's belt and transmit data via IR

or Bluetooth link to a mobile computing device such as a PDA or a cell-phone.

For each test, four processing scenarios are considered. The four scenarios are different in how they model the measurement error covariance matrix and how they use the RAIM algorithm in LSQ GPS processing. It has been shown in Chapter 6 that the global test applied to HSGPS data provides reasonable results. The major position outliers, with hundreds of metres and kilometre-level errors, are almost always reliably detected. However, the local testing, that is the attempt to remove the measurements with the largest LSQ residuals, provides somewhat unreliable estimates of position accuracy. The solution at many epochs frequently becomes even more scattered around the true trajectory. Therefore, it is advisable to analyze only the global test RAIM applied to the HSGPS data. The four processing scenario strategies are summarized below.

8.1.1   Scenario A

In the first processing scenario, all HSGPS LSQ single-point position and velocity fixes are taken as the measurements in the Kalman filter. The measurement error covariance matrix is formed according to Equation 7.12 from the variances of the solution accuracy after the LSQ adjustment procedure. The variance of the heading measurement derived from GPS velocities is taken as a constant value of 30 deg 1σ value.

The PDR system errors are modeled according to the random walk stochastic models described and analyzed in Chapter 5. The parameter of the step-length error is taken as 0.1 m 1σ value. The heading rate error is modeled as a random walk with noise of 10^{-3} deg/sec (1σ) value. This model for the PDR system accurately represents the behaviour of the system. For all the scenarios analysed, the same parameters for

the process noise of the PDR system will be used.

8.1.2   Scenario B

In this scenario the measurement error covariance matrix, $\mathbf{R}$, is modeled adaptively to the geometry of the solution and the modeled UERE for a certain environment. It has already been seen that proper modeling of the measurement error covariance matrix is the key to successful Kalman filtering. As will be shown below, the forming of the measurement covariance matrix based on the LSQ solution variances (Scenario A) provides very poor estimates of the HSGPS solution accuracy. This approach in modeling the HSGPS measurement error covariance matrix is referred as UERE-based. In this analysis, the UERE value is empirically taken as 70 metres.

Also, in this scenario the step limiting constraint is applied. In the results of Scenario A, it will be shown that the step-length estimates may reach very significant values for several consecutive epochs. Since no accurate initialization is available in the considered test scenarios, the step length must be assumed constant and the error estimated in the Kalman filter. The average step length is taken as 0.7 metres. The limiting step length threshold value is taken as 0.1 metres as a 1σ value of the random walk process.

8.1.3   Scenario C

In this processing scenario, only the HSGPS solutions that passed the global test and are considered *accepted* for Kalman filter updating should be used. This will avoid having very large position and velocity outliers from slipping through as measurement updates into the Kalman filter. The availability of the filter updates in this case is decreased, leaving the filter to operate more in the prediction mode.

The measurement error covariance matrix used in this scenario is the proposed UERE-based. Also, the step-length limiting constraint will be applied.

8.1.4 Scenario D

In such environment as a downtown area, there are quite few HSGPS solution epochs that do not have redundancy in observations for the RAIM analysis to be performed. In this scenario, the HSGPS solutions that passed the global test and the solutions that did not have redundancy in observations are considered for Kalman filter updating. The UERE-based HSGPS covariance matrix is used and the step-length limiting constraint is applied.

A summary of the important differences and the processing parameters is given in Table 8.1.4.

Table 8.1: Summary of the Considered Integration Scenarios

	PDR	HSGPS RAIM	HSGPS R matrix
Scenario A:	No constraints	No RAIM	LSQ-based
Scenario B:	Step length constraint	No RAIM	UERE-based
Scenario C:	Step length constraint	GT^1	UERE-based
Scenario D:	Step length constraint	GT^1 and NR^2	UERE-based

GT^1 - RAIM Global Test passed epochs are accepted
NR^2 - RAIM No redundancy epochs are accepted

8.2 Accuracy Assessment of The Estimated Solution

For all tests, the estimated DRMS errors are computed and plotted along with the calculated 2D horizontal errors of the solution computed at the marked trajectory points with respect to the digital map as has been discussed in Chapter 6. It will be shown that for some scenarios, the estimated DRMS accuracy estimates give a

decent representation of the actual 2D accuracy of the solution at the control points.

For the step length, heading and heading rate parameters, no accurate reference is available. These parameters will therefore be plotted only for some cases to demonstrate the step-length limiting constraint. The position solution for the proposed system is of primary interest anyhow.

Also, for all tests, a PDR-only solution is plotted to demonstrate the performance of this low-cost PDR system. In calculating these PDR solutions, the PDR data is processed in a pure PDR mechanization mode assuming a known initial heading. In every test, the drift of this solution will obviously be seen.

In the following sections the results of the four tests are analyzed for every considered processing scenario.

8.3   Test 1

The first analyzed test is the test that was discussed in Chapter 6. The testing trajectory is plotted on the digital map of Calgary and is shown in Figure 8.1. The total test time is approximately 30 minutes.

The position results for Scenario A are shown in Figure 8.2. The step length, heading and heading rate parameters are shown in Figure 8.3. The horizontal accuracy of the solution is computed at the marked points along the trajectory. The estimated kinematic DRMS position error and the accuracy of the solution at the marked points is shown in Figure 8.4.

As can be seen from these results, the integrated solution is very inaccurate. It can hardly be called an improvement when compared to the stand-alone HSGPS solution. The very poor HSGPS accuracy estimates obtained in the LSQ adjustment
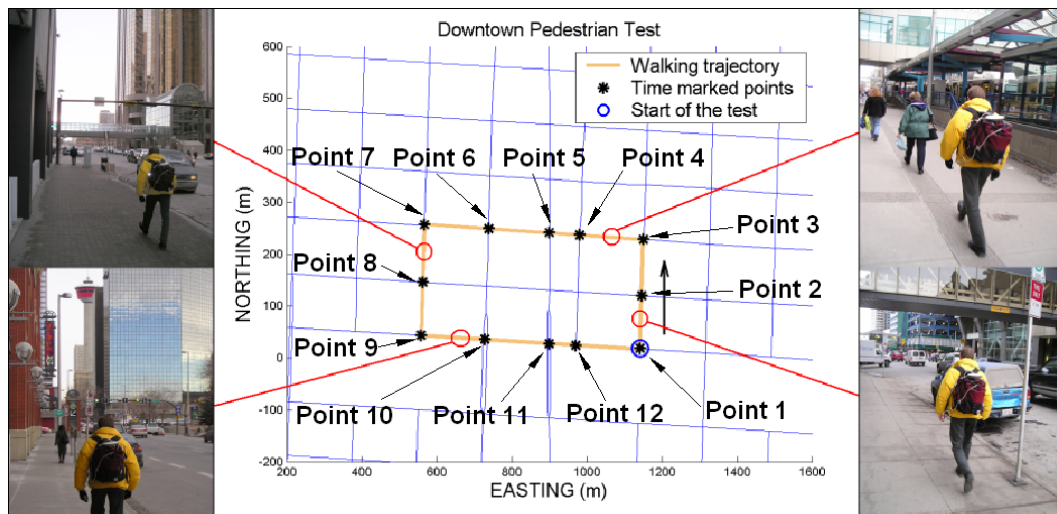
Figure 8.1: Test 1. Downtown Walking Trajectory

procedure account for this poorly integrated inaccurate result. The Easting and Northing HSGPS variances obtained in the LSQ adjustment procedure clearly give an inaccurate representation.
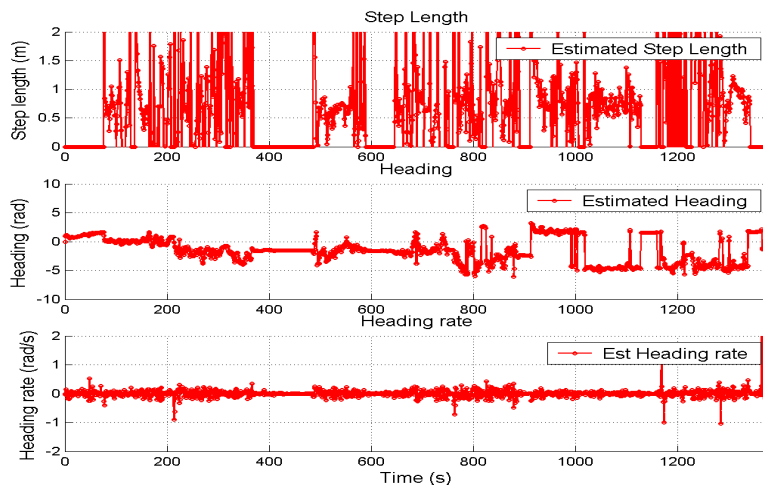
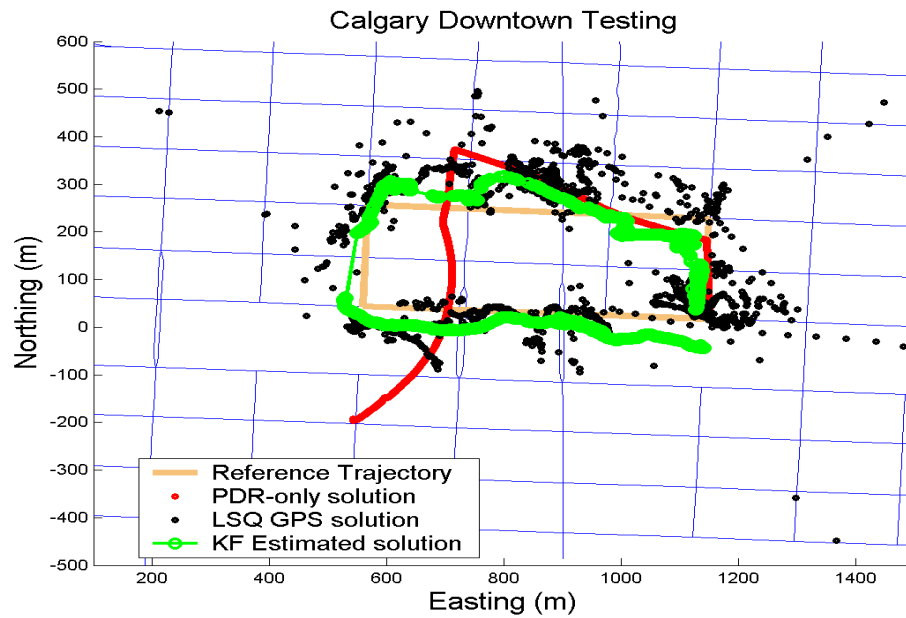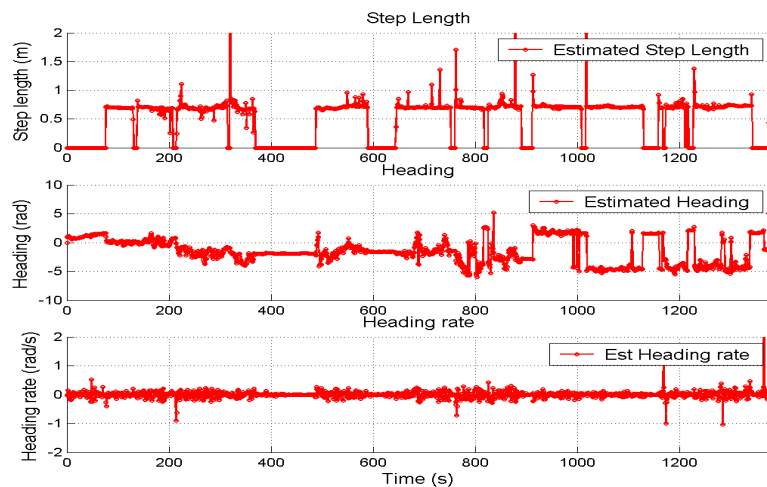Figure 8.3: Test 1, Scenario A. The Estimated Step length, Heading and Heading Rate Parameters
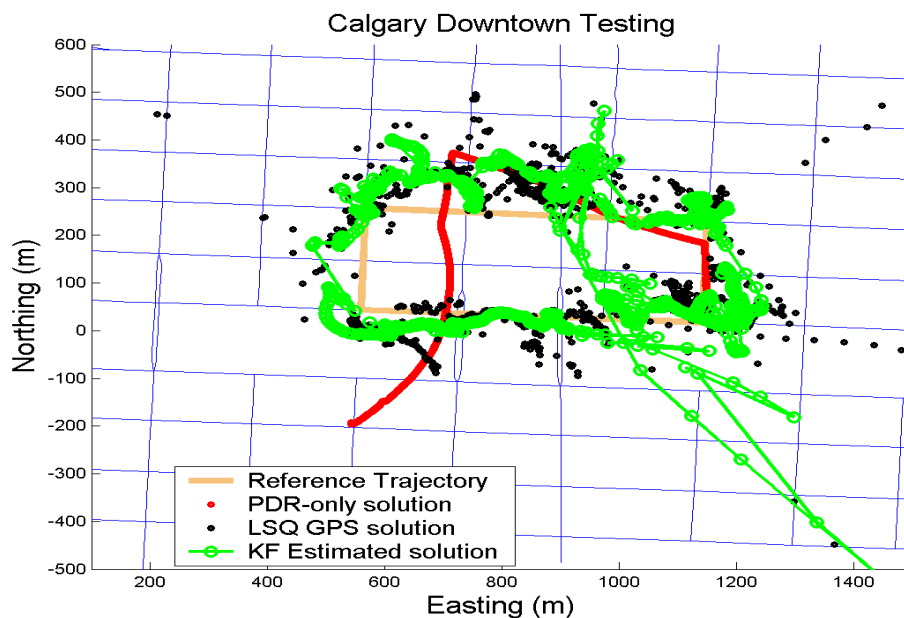
Figure 8.2: Test 1, Scenario A. The Reference, HSGPS, PDR-only and Estimated Position Solutions

In this scenario, the step-length parameter is also poorly estimated. When no additional constraints are applied to the step length, it is significantly affected by position blunders. The propagation of the filter at the following epoch is also erroneous. The average 2D-position accuracy computed at the marked points is approximately 115 metres. The estimated accuracy, though, is much smaller. This contributes to improper modeling of the HSGPS measurement covariance matrix by the LSQ solution variances. The availability of the HSGPS solution in this test scenario is 94%, and the availability of the integrated solution is obviously 100%.

DRMS Position Errors of the Estimated Solution
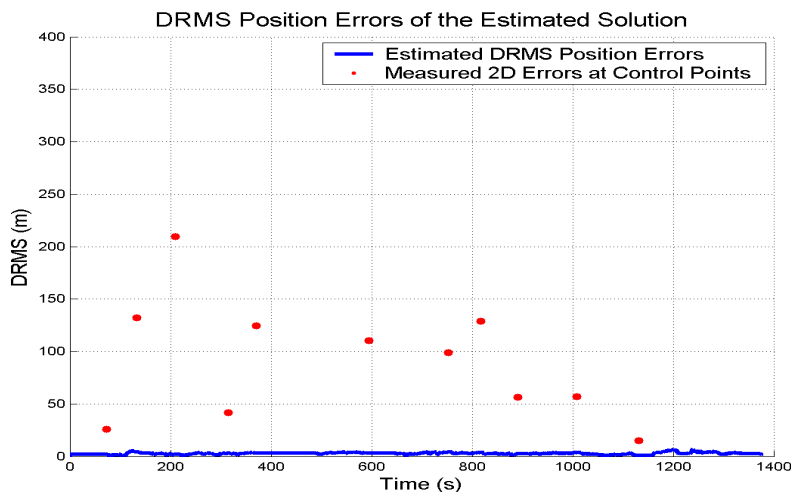
Figure 8.4: Test 1, Scenario A. Estimated DRMS Kinematic Errors and Measured 2D Errors at Marked Points

The performance of the PDR-only position solution should also be noted (shown in Figure 8.2 in red), where a constant step length of 0.7 metres is assumed. In a test taking almost 30 minutes, the final 2D error is approximately equal to 700 metres. This result still outperforms the classical inertial mechanization schemes by a large margin. Also, this PDR-only navigation accuracy follows the accuracy analysis of the PDR systems for the constant step-length bias quite well (Chapter 5).

In the next processing scenario, Scenario B, the HSGPS covariance matrix is formed based on the modeled UERE value for the downtown (taken as 70 metres) and DOP parameters. Also, the step-length limiting constraint is applied to limit the filter errors in the prediction mode. The position results for Scenario B are shown in Figure 8.5. The step length, heading and heading rate parameters are shown in Figure 8.6. The horizontal accuracy of the solution computed at the marked trajectory points is plotted versus the estimated kinematic DRMS position error and is shown in Figure 8.7.

Figure 8.5: Test 1, Scenario B. The Reference, HSGPS, PDR only and Estimated Position Solutions

Figure 8.6: Test 1, Scenario B. The Estimated Step length, Heading and Heading Rate parameters
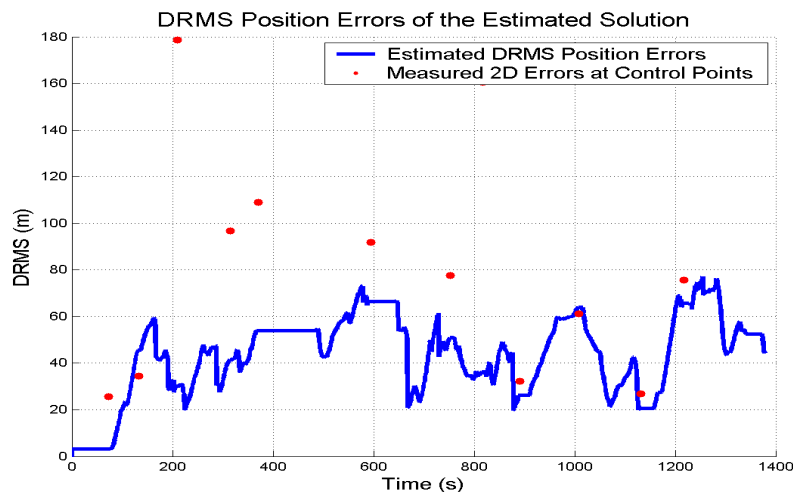
Figure 8.7: Test 1, Scenario B. The Estimated DRMS Error and Measured 2D Errors at Marked Points

The results of this scenario are much better than in Scenario A. The estimated trajectory more closely approaches the true reference trajectory the user has walked. By modeling the measurement covariance matrix, the effects of very large HSGPS position blunders are significantly decreased on filter performance. In this way, the weighting is more optimally distributed between the PDR and HSGPS measurements than in test scenario A. The step-length estimate is limited by a predefined threshold value for more than one epoch. This also contributes significantly to the overall accuracy improvement of the estimation. The DRMS results shown in Figure 8.7 now more closely match the surveyed 2D position accuracy at the marked points.

In the next processing scenario, Scenario C, only the HSGPS solutions that pass the RAIM global test are accepted as measurement updates into the filter. This decreases the overall availability of the HSGPS solution from 96% to 43%. Figure 8.8 shows the position results achieved in this processing scenario. The DRMS estimated position error during the whole test is plotted in Figure 8.9 along with the 2D position errors
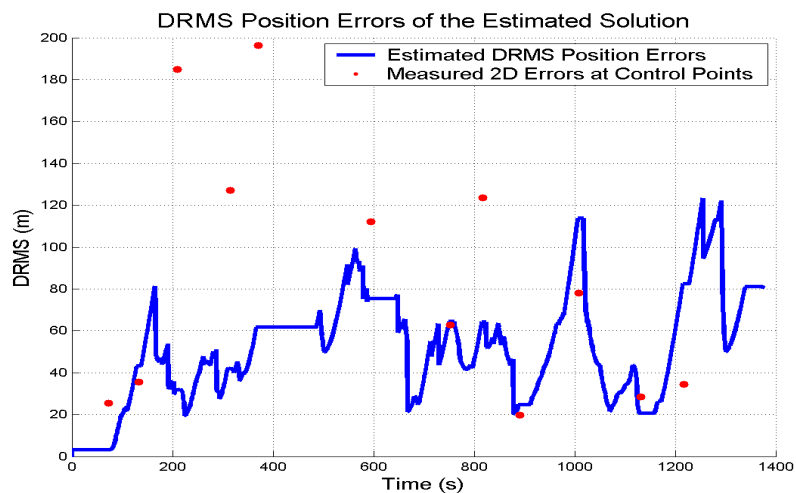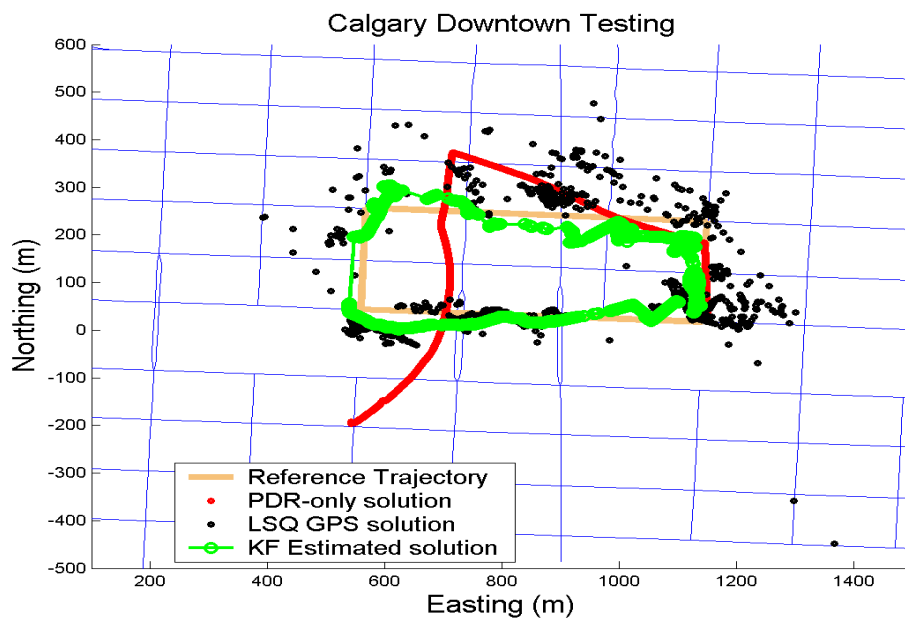
at the marked points.
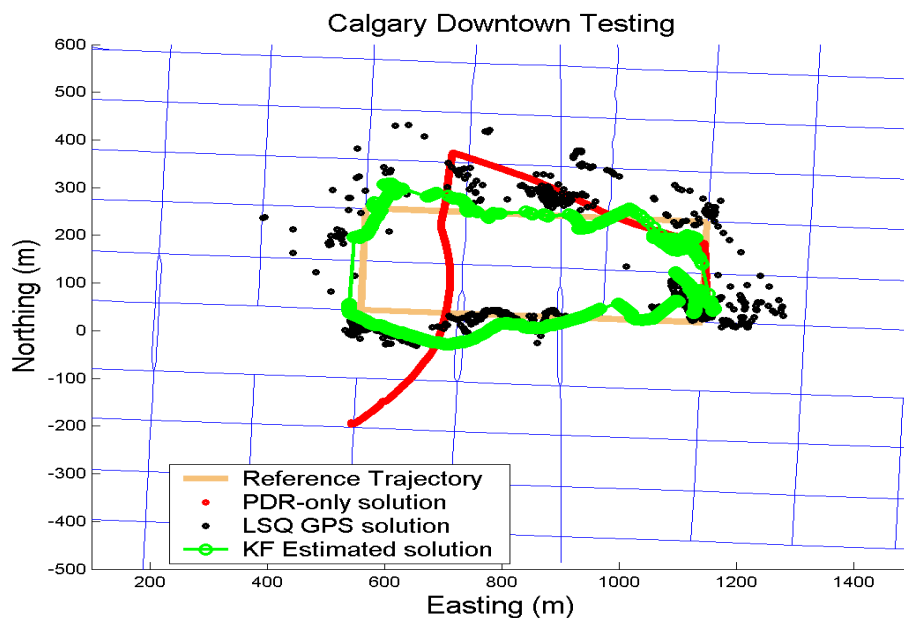
Figure 8.8: Test 1, Scenario C. The Reference, HSGPS, PDR only and Estimated Position Solutions

The results of this scenario are comparable to the results from Scenario B. Here, the filter operates longer in the prediction mode, since the availability of the updated HSGPS drops down almost twice. Several PDR-like stretches of the position solution can be seen in this case. Also, a few more position jumps can be observed. This is due to the fact that longer navigation in PDR mode causes the filter to accept the position and velocity solution rather quickly due to the growing covariance matrix of the estimates.

The position results of the last scenario considered (D) are plotted on Figures 8.10. The DRMS estimated position error during the whole test is plotted in Figure 8.11 along with the 2D position errors at the marked points.

Figure 8.9: Test 1, Scenario C. The Estimated DRMS Error and Measured 2D Errors at Marked Points

Figure 8.10: Test 1, Scenario D. The Reference, HSGPS, PDR only and Estimated Position Solutions
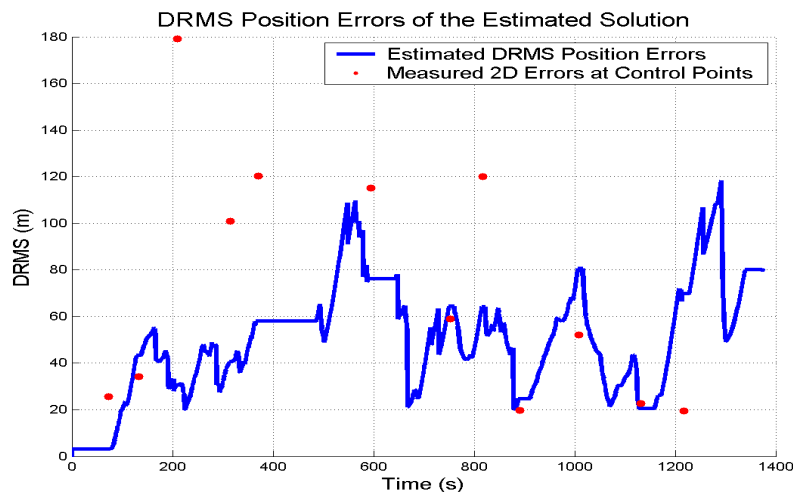
Figure 8.11: Test 1, Scenario D. The Estimated DRMS Error and Measured 2D Errors at Marked Points

In Scenario D, the availability of the HSGPS solution has been increased by 17% when compared to Scenario C, where only epochs accepted after RAIM are taken as measurement updates. The overall HSGPS solution availability is 60%. The overall position accuracy has not been improved by much, but some improvement is still observed. The average 2D position accuracy computed at the marked points is 75 metres, the smallest among the considered scenarios. This difference is not very statistically significant.

The summary of DRMS position errors at the marked points for all four processing scenarios is given in Table 8.3.

From the results of this test and the four considered processing scenarios, Scenarios B, C and D are nearly equivalent in their estimated position accuracy. This demonstrates that the HSGPS measurement error covariance matrix is better represented by the UERE-based approach than by variances in the solution after the LSQ ad-

Table 8.2: Test 1: Horizontal Position Errors of the Estimated Solution at Marked Points (in metres)

Marked Point:	Scenario A	Scenario B	Scenario C	Scenario D
Point 1:	25	25	25	25
Start 2:	132	34	35	34
Start 3:	209	178	184	179
Start 4:	41	96	127	100
Start 5:	124	109	196	120
Start 6:	110	91	112	115
Start 7:	98	77	62	59
Start 8:	129	160	123	119
Start 9:	56	32	19	19
Start 10:	56	61	78	52
Start 11:	14	26	28	22
Start 12:	383	75	34	19
AVERAGE:	115	80	85	**75**

justment. Also, the step-limiting constraint is beneficial in this signal environment, since it allows the filter to more accurately perform in prediction mode.

8.4 Test 2

The second test trajectory is shown in Figure 8.12. The test time is around 40 minutes. Along the trajectory, 10 points at the street intersections have been manually time-marked for horizontal position accuracy analysis.

The position results for Scenario A are shown in Figure 8.13. The step length, heading and heading rate parameters are shown in Figure 8.14. The horizontal accuracy of the solution is computed at the marked points along the trajectory. The estimated kinematic DRMS position error and the accuracy of the solution at the marked points is shown in Figure 8.15.
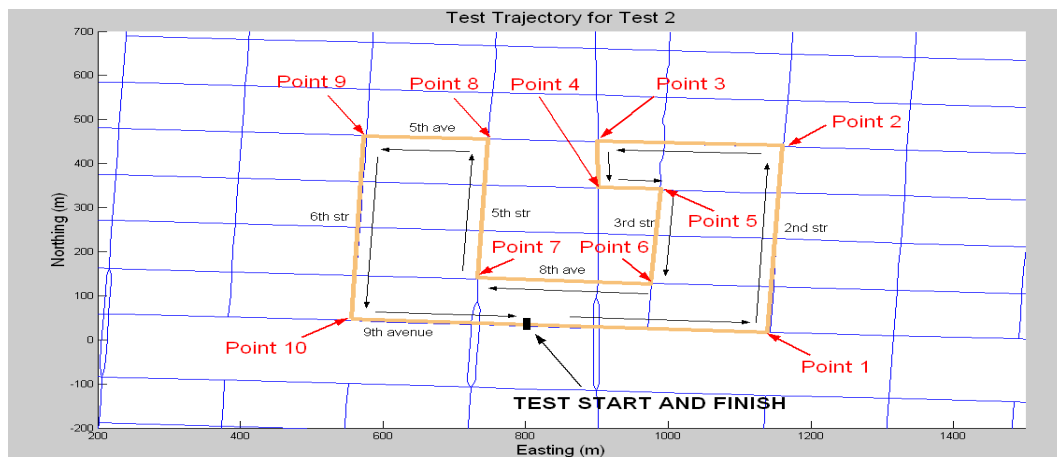
Figure 8.12: Test 2. Downtown Walking Trajectory

Similar to Test 1, the accuracy of the integrated solution is very poor. Barely any improvement can be observed in the integrated solution. The Easting and Northing HSGPS variances obtained in the LSQ adjustment procedure in this case also do not represent the accuracy of the HSGPS measurements very well.
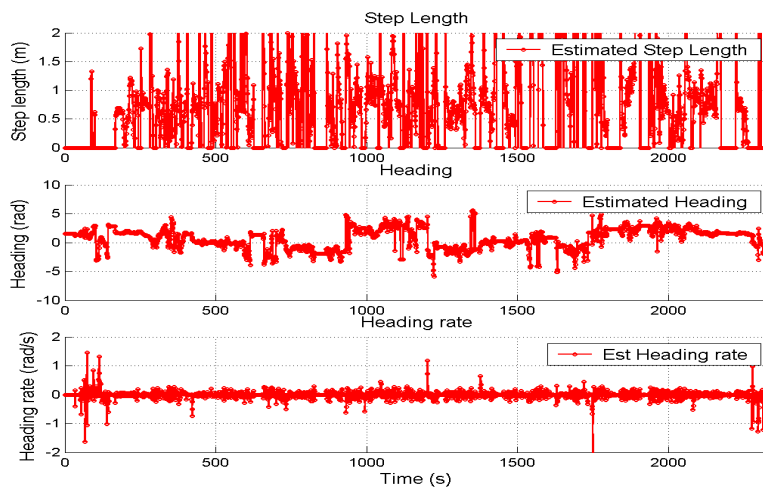

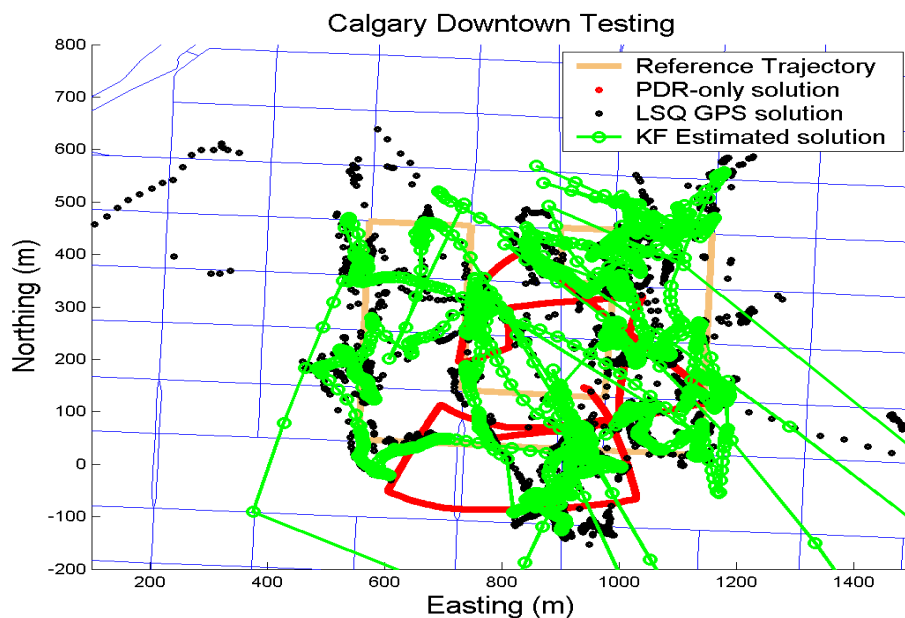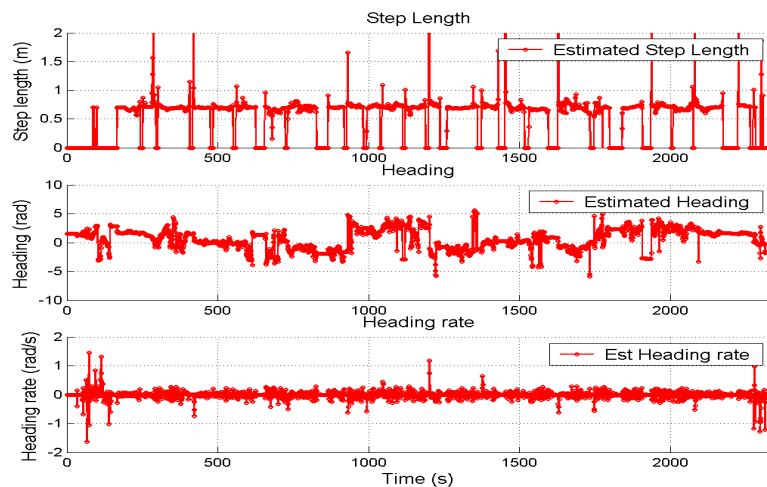Figure 8.14: Test 2, Scenario A. The Estimated Step length, Heading and Heading Rate Parameters

Figure 8.13: Test 2, Scenario A. The Reference, HSGPS, PDR-only and Estimated Position Solutions

Since no step-length constraint is applied in this scenario, step-length estimates are also very poor. The average 2D position accuracy computed at the marked points is 350 metres and is affected by several very large solution blunders. The estimated accuracy, though, is again much smaller due to improper modeling of the **R** matrix. The availability of the HSGPS solution in this test scenario is 95%, and the availability of the integrated solution is 100%.
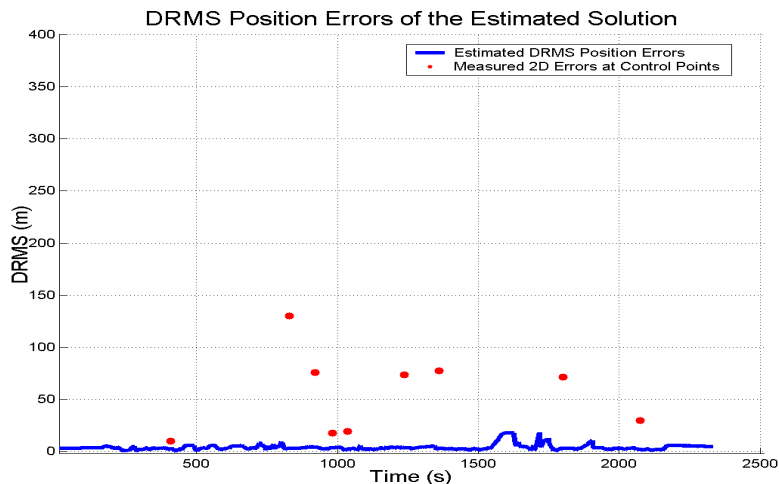
Figure 8.15: Test 2, Scenario A. The Estimated DRMS Kinematic Errors and Measured 2D Errors at Marked Points

The performance of the PDR-only position solution is also very poor. The trajectory is somewhat similar to the true trajectory, but the heading drift and the approximate assumption of the constant step length cause an accumulation of errors. The final PDR-only 2D position error is approximately 200 metres, and the heading drift is about 100 degrees.

As in the first test, the results of Scenario B are also better than the results of Scenario A. The position results for scenario B are shown in Figure 8.16. The step length, heading and heading rate parameters are shown in Figure 8.17. The horizontal accuracy of the solution computed at the marked trajectory points is plotted versus the estimated kinematic DRMS position error and is shown in Figure 8.18.
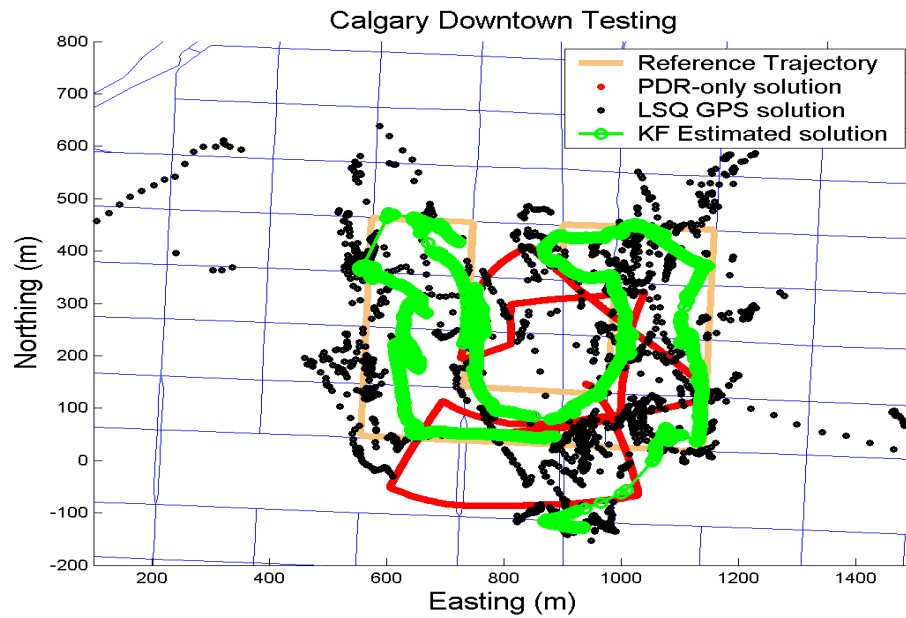
Figure 8.16: Test 2, Scenario B. The Reference, HSGPS, PDR only and Estimated Position Solutions

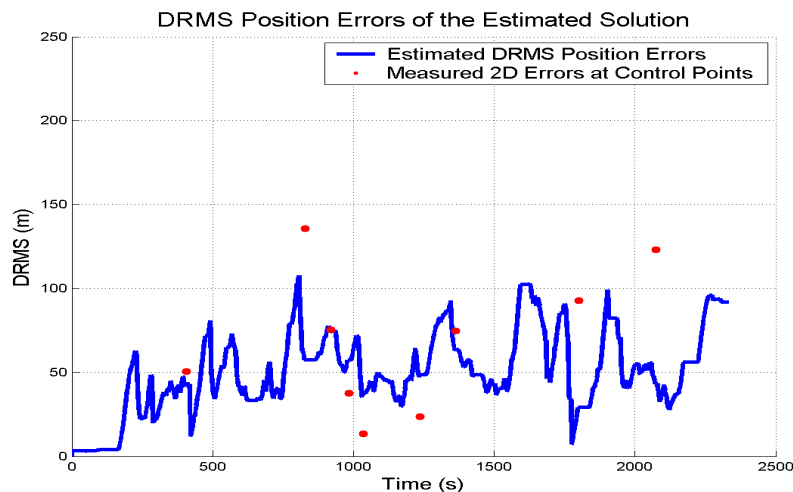Figure 8.17: Test 2, Scenario B. The Estimated Step length, Heading and Heading Rate parameters

Figure 8.18: Test 2, Scenario B. The Estimated DRMS Error and Measured 2D Errors at Marked Points

In this case, the estimated trajectory more closely resembles the reference trajectory. The DRMS results shown in Figure 8.18 also more closely match the surveyed 2D position accuracy at the ten marked points.

In Scenario C, only the HSGPS solutions that pass the RAIM global test are accepted as measurement updates into the filter. This availability of the HSGPS solution becomes 30%. Figure 8.19 shows the position results achieved in this processing scenario. The DRMS estimated position error during the whole test is plotted in Figure 8.20 along with the 2D position errors at the marked points.

In this scenario, the filter operates most of the time in the prediction mode (PDR navigation). This can be seen as several long stretches of the estimated trajectory, which are very similar to the PDR-only solution. In this case, the accuracy of the solution does not increase by much, even though by applying RAIM testing, major outliers were removed from the measurement updates. Two things contribute to
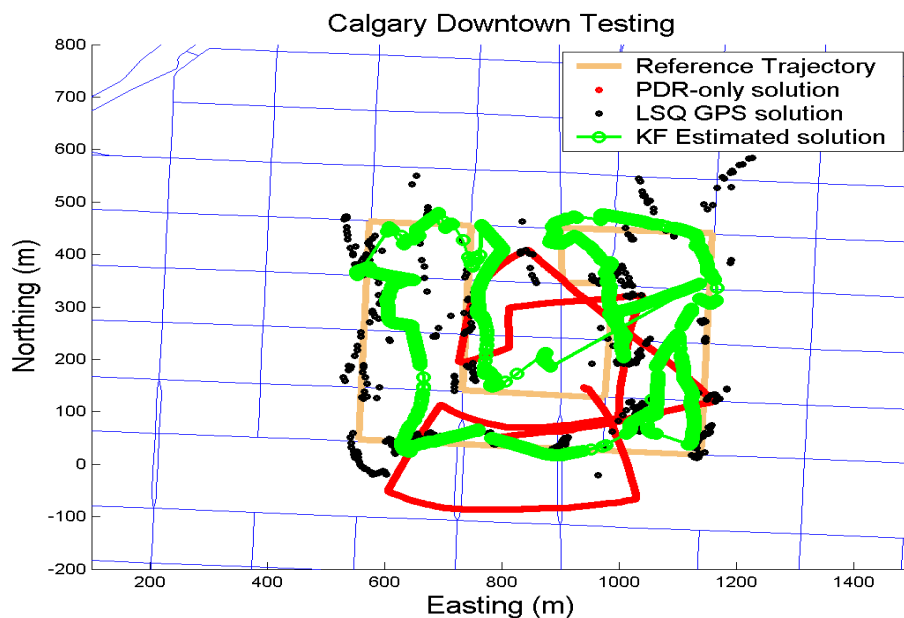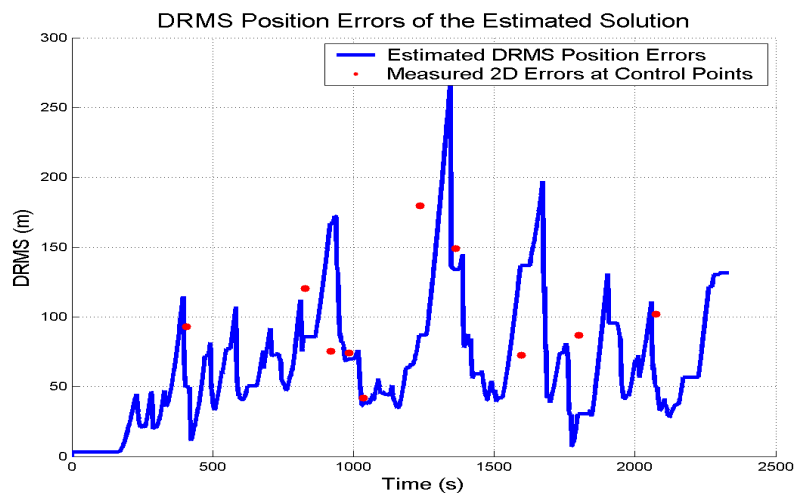
Figure 8.19: Test 2, Scenario C. The Reference, HSGPS, PDR only and Estimated Position Solutions

the poor estimation results in this case: one is the long-term navigation in the prediction mode, and the other is the erroneous estimation of the heading prior to the filter prediction mode. Once the filter starts navigating in the prediction mode, it simply propagates the last optimal heading estimate with the PDR heading rate measurements. In this situation, the PDR errors are minor compared to the large heading bias of the filter from the previous epoch.

The position results of the last scenario, Scenario D, are plotted on Figure 8.21. The DRMS estimated position error during the whole test is plotted in Figure 8.22 along with the 2D position errors at the marked points.

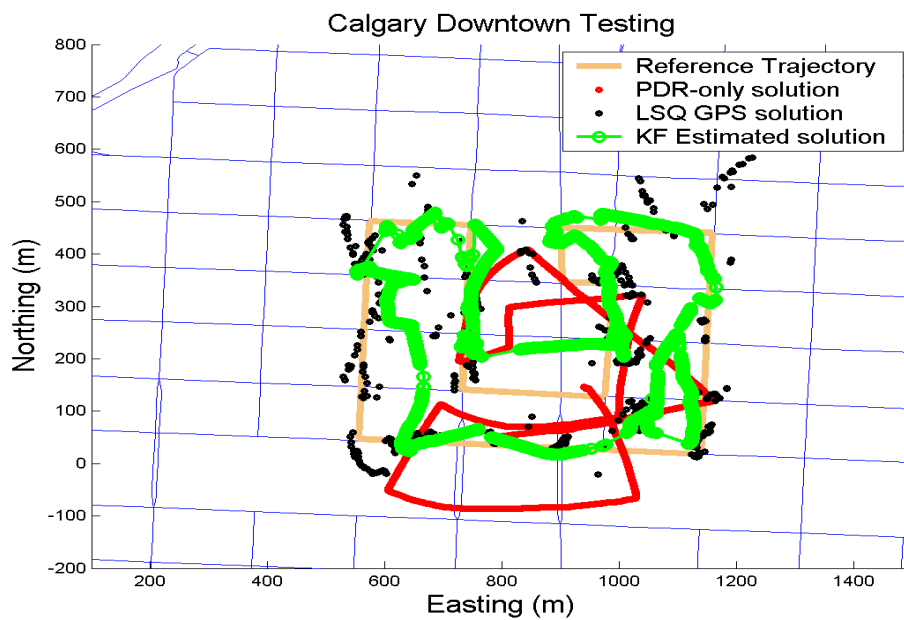Figure 8.20: Test 2, Scenario C. The Estimated DRMS Error and Measured 2D Errors at Marked Points

Figure 8.21: Test 2, Scenario D. The Reference, HSGPS, PDR only and Estimated Position Solutions
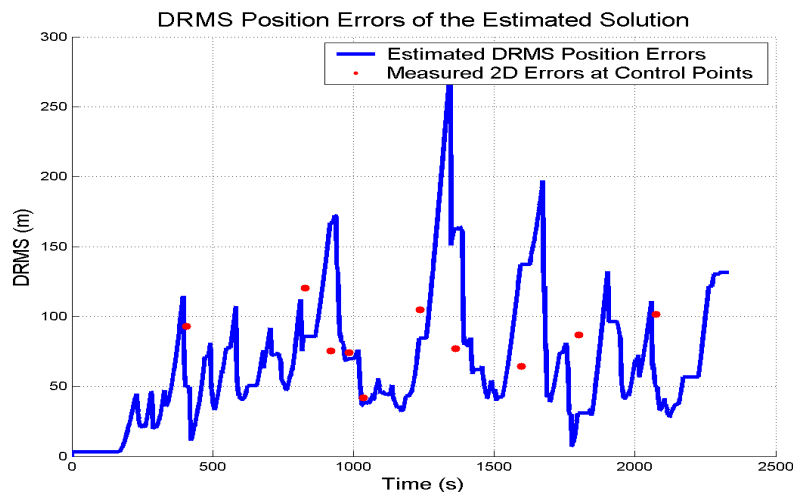
Figure 8.22: Test 2, Scenario D. The Estimated DRMS Error and Measured 2D Errors at Marked Points

By allowing the filter updates to accept the solutions that are marked "no redundancy", availability in this case is increased by only 3 epochs. The position results are thus very similar along the whole trajectory path except for the middle portion, where these 3 updates slightly improve the estimated results.

A summary of the DRMS position errors at the marked points for all four processing scenarios for Test 2 is given in Table 8.4.

Three scenarios are again very equivalent in the estimation results accuracy, and they are Scenarios B, C and D. In this test, though, preference should be given to Scenario B, even though Scenario D shows slightly better accuracy at the control points.

Table 8.3: Test 2: Horizontal Position Errors of the Estimated Solution at Marked Points (in metres)

Marked Point:	Scenario A	Scenario B	Scenario C	Scenario D
Point 1:	9	50	92	92
Start 2:	129	135	120	120
Start 3:	76	75	75	75
Start 4:	17	37	74	74
Start 5:	19	13	42	42
Start 6:	73	23	179	104
Start 7:	77	74	148	76
Start 8:	3066	230	72	64
Start 9:	71	92	87	86
Start 10:	29	123	101	101
AVERAGE:	357	85	99	**83**

8.5 Test 3

The third test trajectory is shown in Figure 8.23. The test time is a bit shorter than the first two, lasting around 20 minutes. Also, 10 control points at street intersections have been manually time-marked along the trajectory for horizontal position accuracy analysis. In this test, only position domain results will be shown and discussed for every processing scenario.

The position results for Scenario A are shown in Figure 8.24. The estimated kinematic DRMS position error and the accuracy of the solution at the marked points is shown in Figure 8.25.

Similar to Tests 1 and 2, these integration results can hardly be seen as an improvement. Due to improper modeling of the measurement error covariance matrix, this processing strategy essentially does not provide any improvement to the HSGPS stand-alone solution.
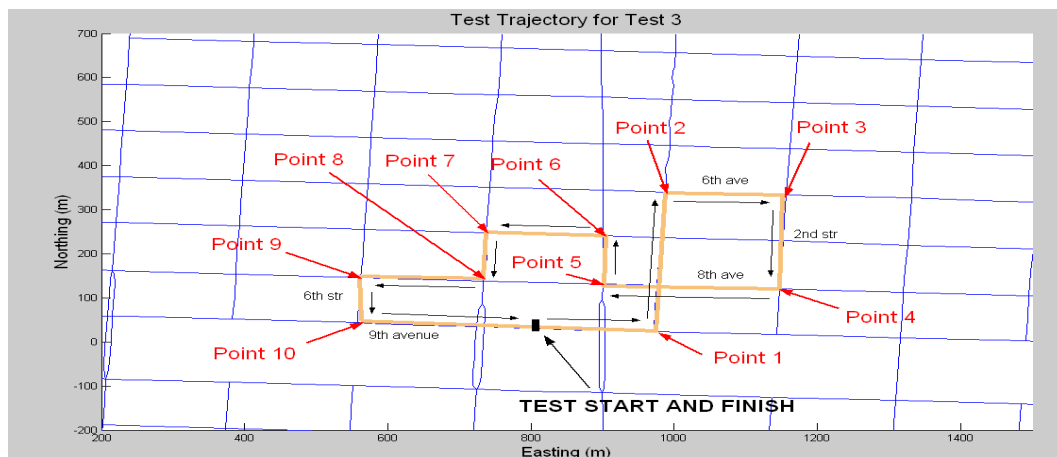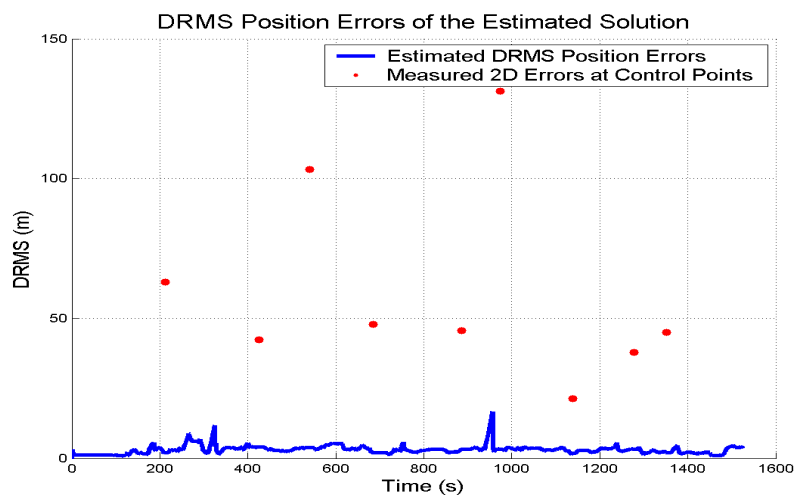
Figure 8.23: Test 3. Downtown Walking Trajectory

Figure 8.25: Test 3, Scenario A. The Estimated DRMS Kinematic Errors and Measured 2D Errors at Marked Points

The performance of the PDR-only position solution is also very poor. The trajectory is only vaguely similar to the true walked trajectory. The final 2D position error in the PDR-only solution is nearly 600 metres. The heading error is almost 150 degrees
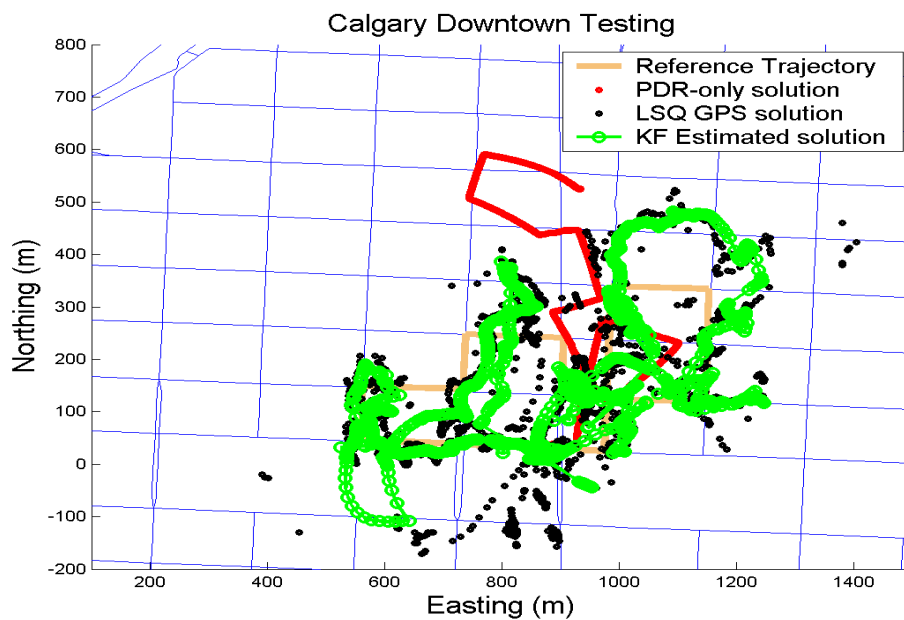
Figure 8.24: Test 3, Scenario A. The Reference, HSGPS, PDR-only and Estimated Position Solutions

after 20 minutes of navigation.

The results of Scenario B show significant position accuracy improvements, which are shown in Figure 8.26. The horizontal accuracy of the solution computed at the marked trajectory points is plotted versus the estimated kinematic DRMS position error and is shown in Figure 8.27.
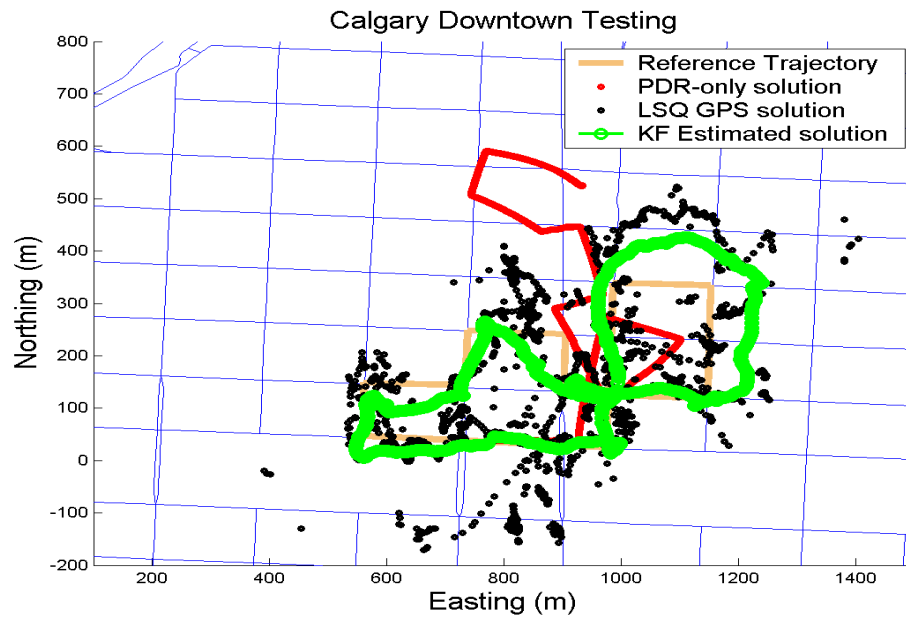
Figure 8.26: Test 3, Scenario B. The Reference, HSGPS, PDR only and Estimated Position Solutions
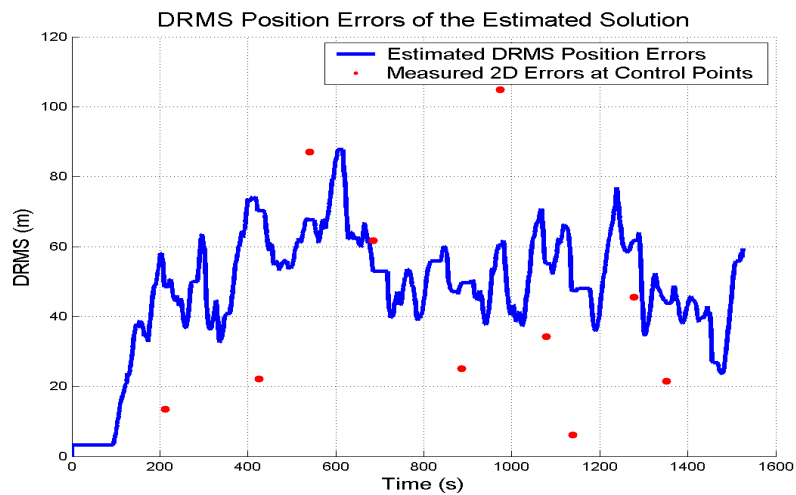

Figure 8.27: Test 3, Scenario B. The Estimated DRMS Error and Measured 2D Errors at Marked Points

In this scenario, the estimated trajectory shape is very close to the true one. In the northeast corner of the trajectory, the solution is still dragged away by a series of consecutive outliers. The average 2D accuracy of the estimated position solution computed with respect to the marked points is only 42 metres. Considering the environment and the PDR data, this result can be considered very good.

In Scenario C, only the HSGPS solutions that pass the RAIM global test are accepted as measurement updates into the filter. This availability of the HSGPS solution becomes very small, less than 30%. Figure 8.28 shows the position results achieved in this processing scenario. The DRMS estimated position error during the whole test is plotted in Figure 8.29 along with the 2D position errors at the marked points.
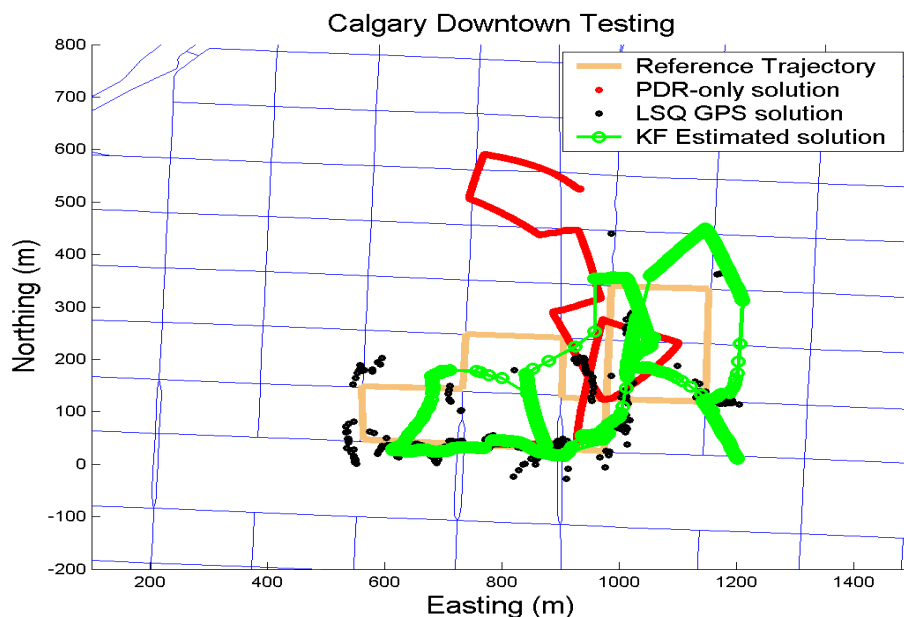

Figure 8.28: Test 3, Scenario C. The Reference, HSGPS, PDR only and Estimated Position Solutions

For the same reasons that we saw in Test 2, the poor heading estimates, especially,
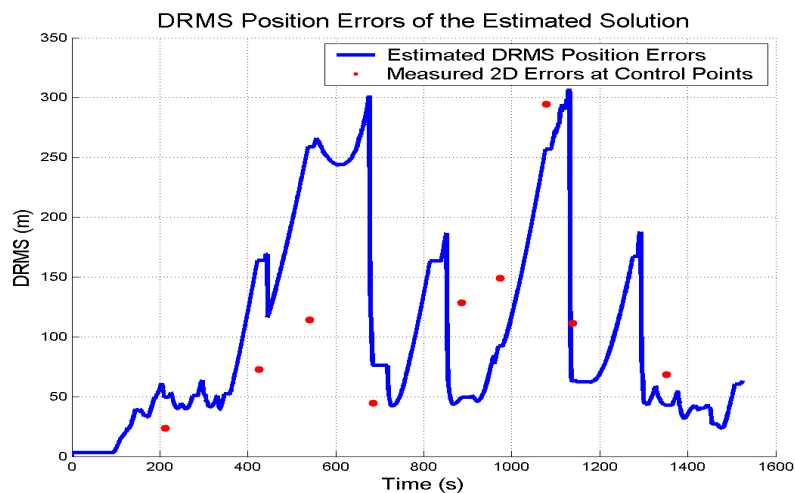
Figure 8.29: Test 3, Scenario C. The Estimated DRMS Error and Measured 2D Errors at Marked Points

lead to a very erroneous propagation of the PDR solution in pure prediction mode. This strategy is not an optimal approach since the solution availability becomes so poor.

The position results of the last scenario, D, are plotted on Figure 8.30. The DRMS estimated position error during the whole test is plotted in Figure 8.31 along with the 2D position errors at the marked points.
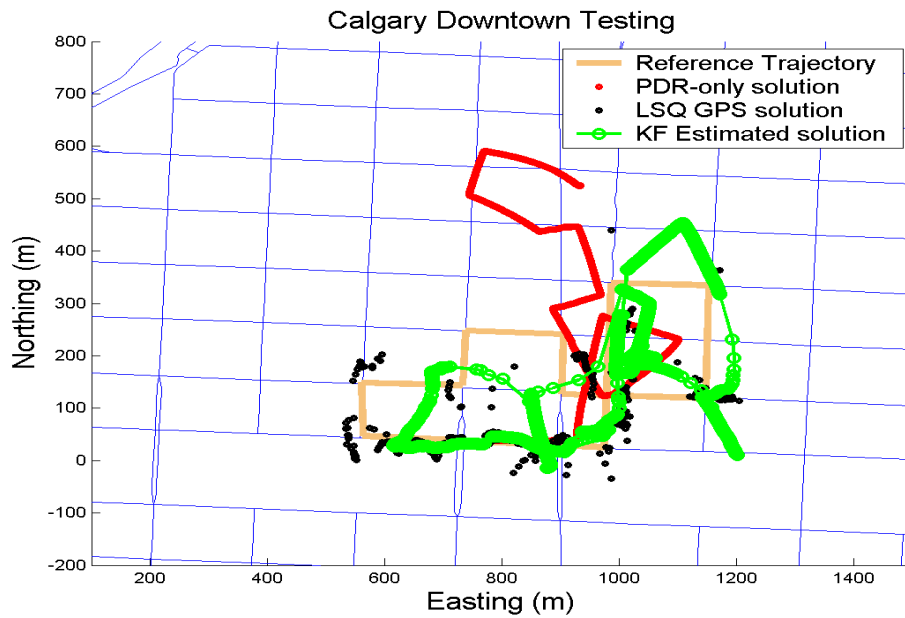
Figure 8.30: Test 3, Scenario D. The Reference, HSGPS, PDR only and Estimated Position Solutions
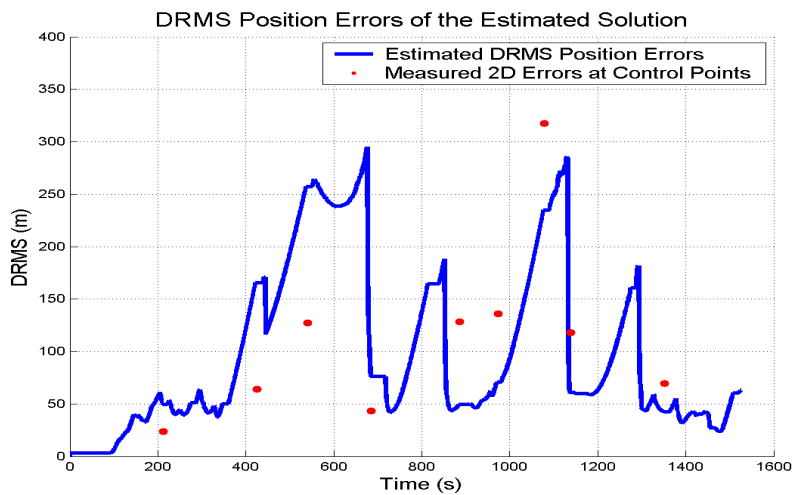

Figure 8.31: Test 3, Scenario D. The Estimated DRMS Error and Measured 2D Errors at Marked Points

In this scenario, availability has been increased by only 10 epochs. The position results are thus very similar along the whole trajectory path, except for a few insignificant changes along the path.

A summary of the DRM position errors at the marked points for all four processing scenarios for Test 3 is given in Table 8.5.

Table 8.4: Test 3: Horizontal Position Errors of the Estimated Solution at Marked Points (in metres)

Marked Point:	Scenario A	Scenario B	Scenario C	Scenario D
Point 1:	63	13	23	23
Start 2:	42	22	72	63
Start 3:	103	87	114	127
Start 4:	47	61	44	43
Start 5:	45	25	128	128
Start 6:	131	104	149	136
Start 7:	140	34	294	317
Start 8:	21	6	111	118
Start 9:	37	45	333	359
Start 10:	45	21	68	69
AVERAGE:	67	**42**	134	138

Comparing the results of the four analyzed strategies in Test 3, the processing Scenario B is again preferable. In this scenario all the HSGPS updates are fed into the filter and the measurement covariance matrix is formed based on the modeled UERE and DOP parameters.

8.6   Test 4

The fourth analyzed test trajectory is shown in Figure 8.32. The test time is equal to approximately 30 minutes of walking. Also, along the trajectory, 10 control points at the street intersections have been manually time-marked for horizontal position

accuracy analysis. In this test, also, only the position domain results will be shown and discussed for every processing scenario.
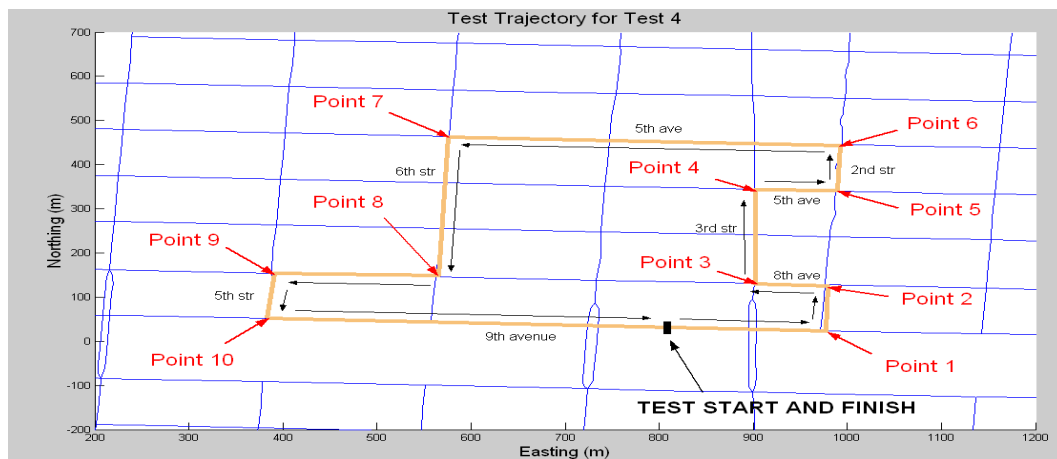

Figure 8.32: Test 4. Downtown Walking Trajectory

The position results for Scenario A are shown in Figure 8.33. The estimated kinematic DRMS position error and the accuracy of the solution at the marked points is shown in Figure 8.34.

As in all three previous tests, the accuracy of the integration results is really poor. It can be concluded that the modeling of the measurement error covariance matrix cannot be done based on the LSQ position variances.
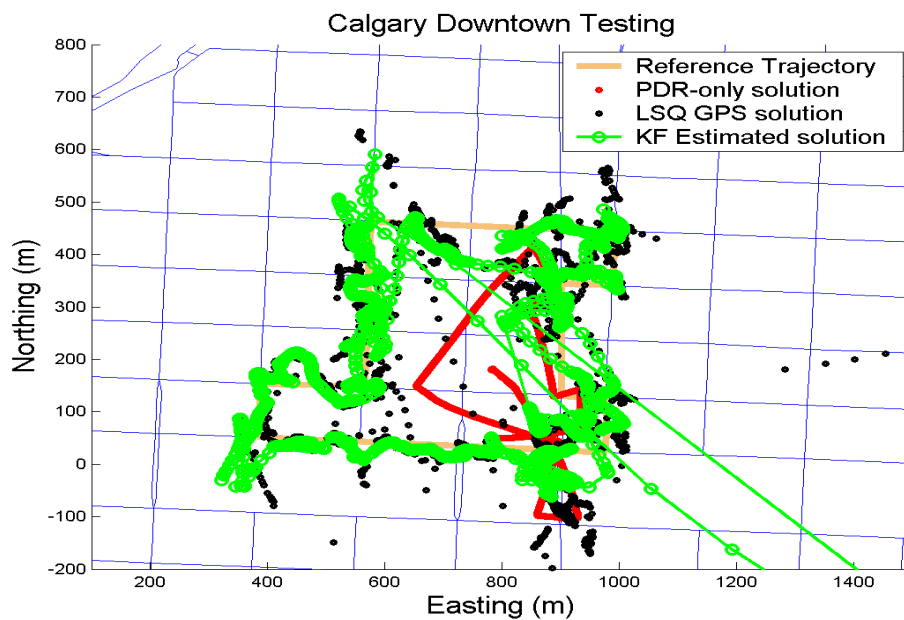
Figure 8.33: Test 4, Scenario A. The Reference, HSGPS, PDR-only and Estimated Position Solutions
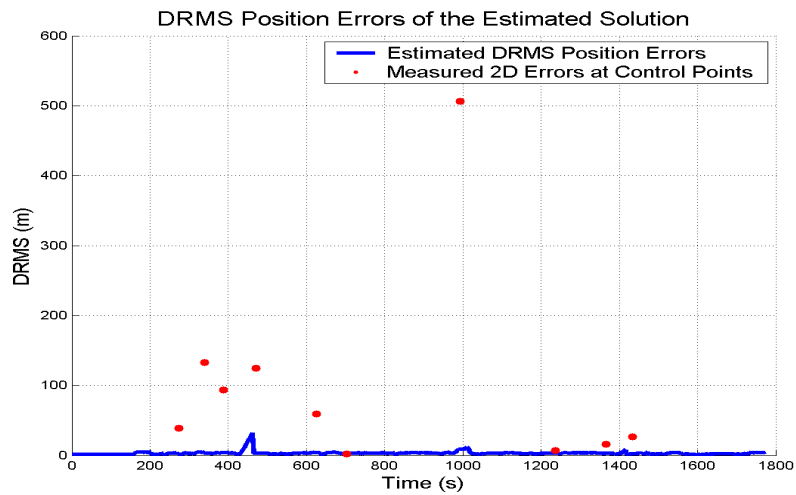

Figure 8.34: Test 4, Scenario A. The Estimated DRMS Kinematic Errors and Measured 2D Errors at Marked Points

The performance of the PDR-only position solution is also very poor. The final 2D position error of the PDR-only solution may seem small, around 200 metres, but the shape of the trajectory due to the very large heading drift is not near the reference trajectory. The final heading error is almost 200 degrees.

The results of Scenario B show very significant position accuracy improvements. The position results for this scenario are shown in Figure 8.35. The horizontal accuracy of the solution computed at the marked trajectory points is plotted versus the estimated kinematic DRMS position error and is shown in Figure 8.36.
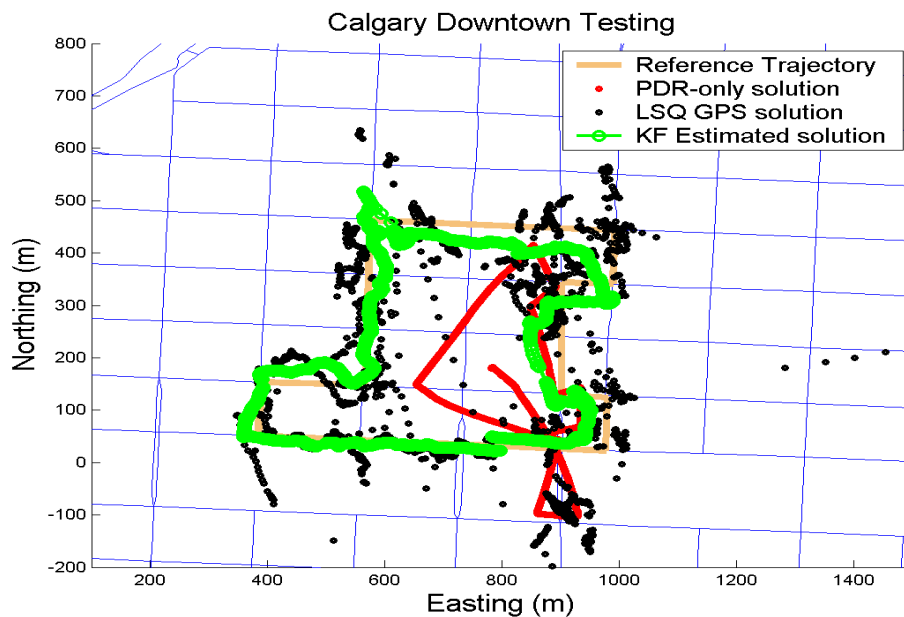

Figure 8.35: Test 4, Scenario B. The Reference, HSGPS, PDR only and Estimated Position Solutions
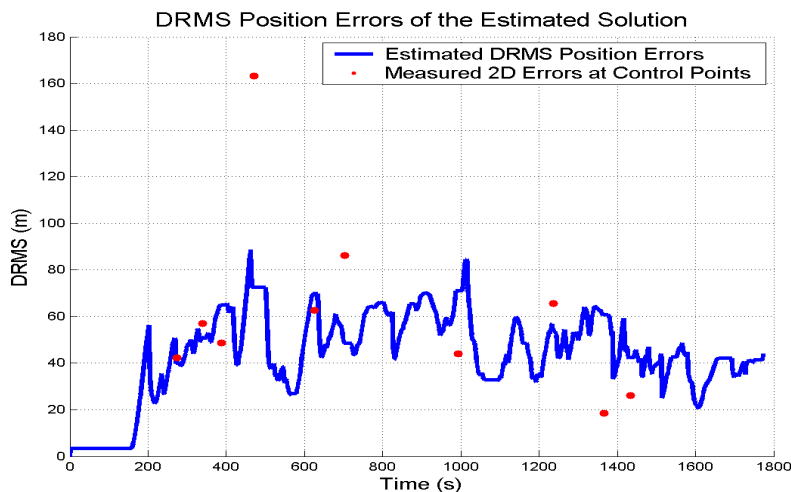
Figure 8.36: Test 4, Scenario B. The Estimated DRMS Error and Measured 2D Errors at Marked Points

The results of this scenario are as good as they can get considering the quality of the HSGPS and PDR data. The average 2D accuracy of the estimated position solution computed with respect to the marked points is only 62 metres.

In Scenario C, the availability of the HSGPS solution also drops significantly, to less than 30%. Figure 8.37 shows the position results achieved in this processing scenario. The DRMS estimated position error during the whole test is plotted in Figure 8.38 along with the 2D position errors at the marked points.

In this case, the estimates of the heading before the filter turns into the prediction mode are slightly better than in previous tests, but again, position accuracy is not improved. The average 2D position errors at the marked points are increased to 91 metres.

The position results of the last scenario, D, are plotted on Figure 8.39. The DRMS estimated position error during the whole test is plotted in Figure 8.40 along with
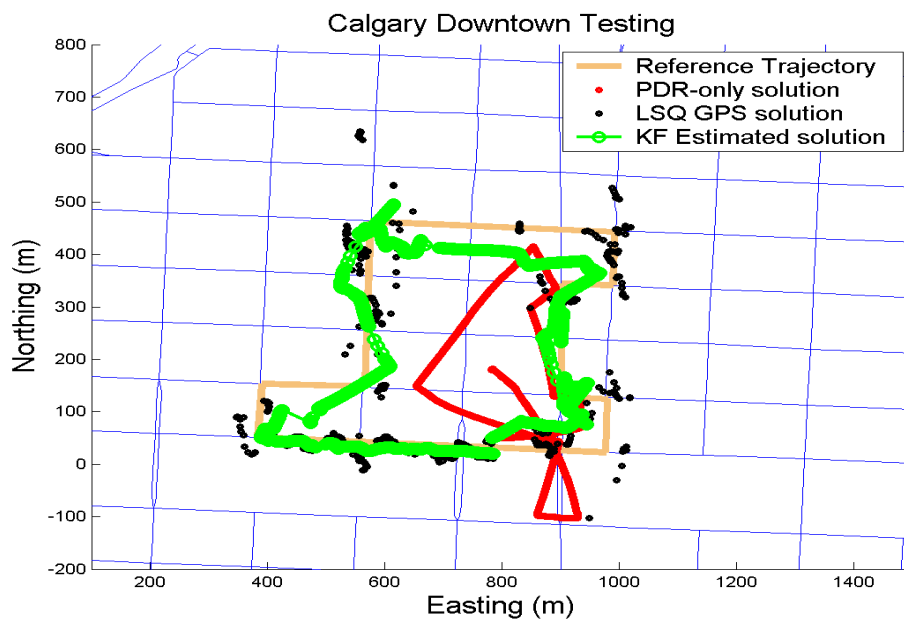
Figure 8.37: Test 4, Scenario C. The Reference, HSGPS, PDR only and Estimated Position Solutions
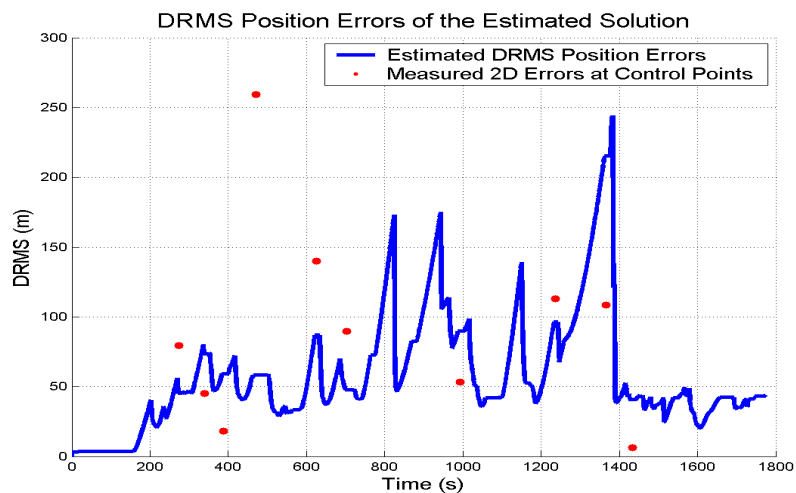
the 2D position errors at the marked points.

Figure 8.38: Test 4, Scenario C. The Estimated DRMS Error and Measured 2D Errors at Marked Points
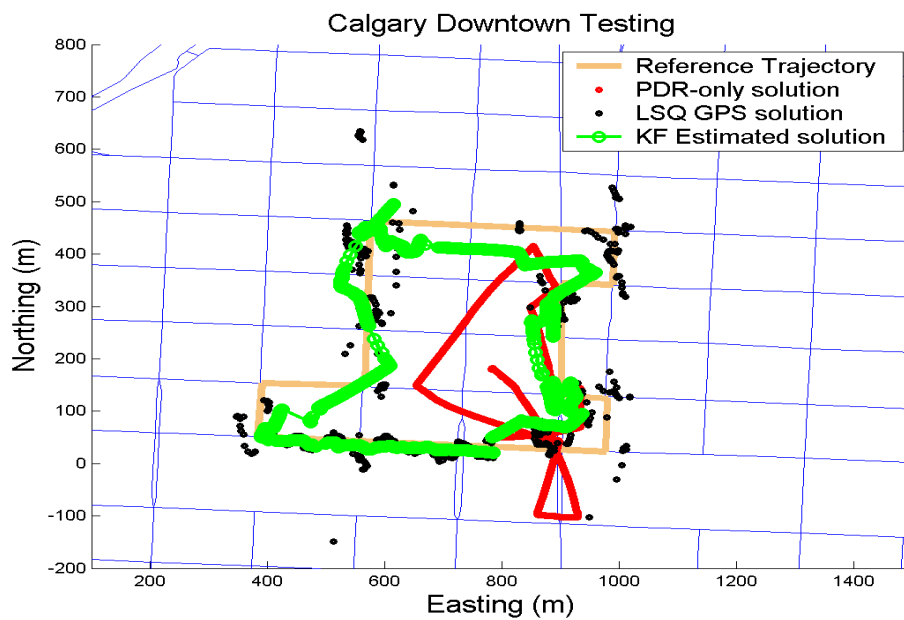

Figure 8.39: Test 4, Scenario D. The Reference, HSGPS, PDR only and Estimated Position Solutions
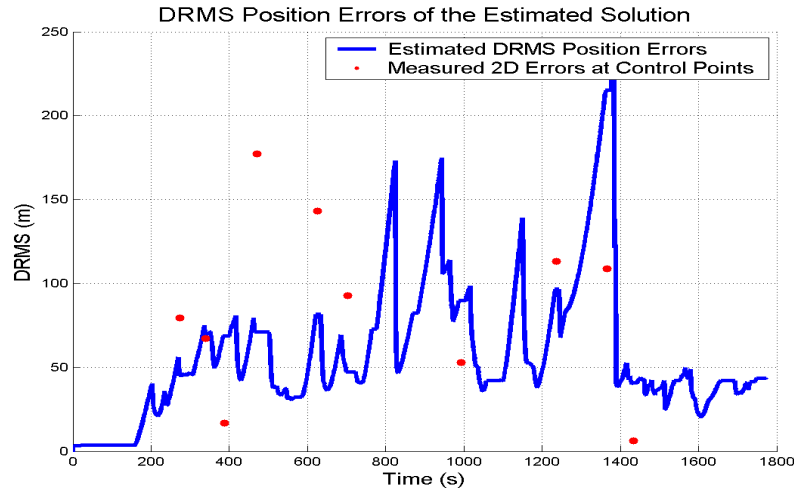
Figure 8.40: Test 4, Scenario D. The Estimated DRMS Error and Measured 2D Errors at Marked Points

In this scenario, availability has been increased only by 15 epochs. The position results are thus very similar along the whole trajectory path except for a few changes along the east part of the trajectory. The summary of DRMS position errors at the marked points for all four processing scenarios for Test 4 is given in Table 8.6.

In this test also, preference should be given to Scenario B, since it leads to the best estimate of the position solution. The processing Scenario B essentially performs the same, or better, in all analyzed tests. In this scenario, all available HSGPS solutions are taken as measurement updates into the filter, and the modeling of the measurement error covariance matrix by the UERE-based model seems to approximate the HSGPS position solution rather adequately. Scenarios C and D essentially nullify the advantage of the HSGPS outstanding solution availability. The erroneous estimates of the heading prior to the filter prediction mode (when the HSGPS solution is considered unavailable) introduce constant heading bias in the PDR mechanization. This bias leads to constant error accumulation, which leads in turn to rather

Table 8.5: Test 4: Horizontal Position Errors of the Estimated Solution at Marked Points (in metres)

Marked Point:	Scenario A	Scenario B	Scenario C	Scenario 4
Point 1:	39	42	79	79
Start 2:	132	57	44	67
Start 3:	93	48	18	16
Start 4:	124	163	259	177
Start 5:	59	62	140	143
Start 6:	2	86	89	92
Start 7:	506	44	53	53
Start 8:	6	65	113	113
Start 9:	15	18	108	108
Start 10:	26	26	6	6
AVERAGE:	100	**61**	91	85

significant position errors.

Chapter 9

Conclusions and Recommendations for Future Work

This chapter presents the conclusions drawn from the results of this thesis and recommendations for future work.

9.1   Conclusions

The contribution of this thesis was the analysis and assessment of the performance of an HSGPS-based pedestrian navigation system aided by a set of low-cost sensors. Auxiliary sensors are only required for GPS-based pedestrian navigation systems in signal degraded environments where the accuracy and reliability of GPS position and velocity solutions, particularly for HSGPS, is poor. Thus, the objective of this thesis was to design and test a low-cost PDR system and to determine the optimal integration strategy that maximized the HSGPS solution accuracy with minimal assumptions.

Chapter 4 presents the design of the low-cost MEMS based inertial senor assembly that was used in the testing. The aspects of the mechanical and electrical design considerations are discussed. The method to synchronize the sensor data with GPS time used in this work is presented.

In Chapter 5, a detailed analysis of the performance of the PDR system described in Chapter 4 is presented. The largest advantage of this novel pedestrian navigation

system is that errors grow proportional to the distance traveled and not travel time as in classical inertial navigation schemes. This chapter presents the analysis of the effects of errors introduced by the primary system parameters, such as heading and step length, on PDR position accuracy. The method for modeling position error growth versus traveled distance for the PDR mechanization for several stochastic step length error models is outlined. This analysis supports the rapid estimation of the expected accuracy of the pedestrian navigation system in PDR-only navigation mode when the behaviour of key system parameter errors is assumed a priori.

Chapter 6 presents the performance and signal quality analysis of the HSGPS receiver in downtown city areas. These urban areas provide a challenging signal environment as the availability of the solution is high (usually more than 90%) while the position and velocity errors are large. The large measurement errors are caused by multipath effects. Also, the HSGPS receiver is susceptible to acquiring either echo-only or cross-correlation signals that may cause unbounded pseudorange and Doppler measurement errors. The RAIM algorithms applied to the HSGPS data has not been shown to be overly successful in improving the position solution accuracy, however, the RAIM does help detect large position outliers. As a result of global solution inconsistency testing, there is a significant reduction in the availability of solutions that are declared reliable, from overall solution availability of (usually) 90% to 30 - 40%.

The integration methodology of the PDR and HSGPS data is proposed and discussed in Chapter 7. Key timing issues and the filter mode operation for different pedestrian motion states and GPS signal conditions are addressed. The optimal integration filter states are then proposed based on the previous analysis of the HSGPS solution accuracy and the quality of the PDR system. A linearized Kalman filter model is developed that propagates the filter states forward based on the PDR measurements

and updates the estimates with the HSGPS data. The discussion of the fault detection algorithms for implementation with a Kalman filter is given, however the proper application of such methods for the proposed system would require several important and rather critical assumptions during the filter initialization. The necessary information required to make these assumptions is not always obtainable.

Chapter 8 presents the experimental results of the system on field data. Several modeling scenarios for the covariance of the HSGPS observations are analyzed. The unknown distribution of the HSGPS errors in a signal-degraded environment presents a challenge for the proper modeling of the covariance matrix for the available HSGPS updates. It has also been shown that the applicability of RAIM in the integrated system is also quite limited. It reduces the solution availability and leads to increased periods during which the filter operates in prediction mode. The filter operates in this mode based on the last available optimal state estimates, which are frequently erroneous. This causes significant error growth during the prediction stage of filter operation. The integrated solution based on the error covariance matrix has been shown to be accurate to 150 metres DRMS more than 90% of the time for the tests under study.

9.2   Future Work Recommendations

The following recommendations can be made for future investigation based on the results of this thesis.

The adaptation of known RAIM processing schemes need to be improved for the case of HSGPS data in signal degraded environments. The frequent multiple blunders occurring at a single epoch and the lack of redundancy in observations makes the existing fault detection schemes not optimal for the HSGPS case. The fault detection

algorithms can also be applied in the Kalman filter. It has been discussed in Chapter 7 that such methods will require the accurate filter initialization. This condition is difficult to achieve for the proposed integration algorithm without relying on many assumptions. Although it may be further studied for the case when a user is walking into a signal-degraded environment such as a downtown area from an open sky environment. In this case, the reliability testing in the Kalman filter could potentially be applied, but the reliability modeling needs to be addressed with great care.

In this thesis several approaches to modeling the error covariance matrix of the HSGPS measurements are analyzed. The proposed method of modeling this matrix based on the UERE and DOP parameters has a clear mathematical meaning, is logically motivated and provides accurate results. Even so, this method is not optimal. Further study of the advanced modeling of this error covariance matrix will additionally improve the results.

The Kalman filter is an infinite memory filter with infinite impulse response time. The effect of the past measurements on the current estimates of the solution is decreased from epoch to epoch but some information still remains. In such a degraded signal environment as a downtown area, filter performance may be improved if the effects of accepted blunderous measurements on the estimated vector were nullified after a certain number of epochs. In other words, the use of a short-memory filter for the integration of HSGPS data is potentially preferable. An example of such filter is a kinematic batch GPS LSQ processing algorithm (Mezentsev, 2004). Such alternative filtering methods can theoretically improve the performance of the integrated results and deserve future investigation.

Another promising approach that may increase the estimation accuracy of the HSGPS pedestrian navigation system is position and velocity correlation testing (Mezentsev et al., 2003). Ideally, during motion maintaining a linear and constant speed, the

velocity solution should mimic the position solution rather well within the limits of the solution accuracy. Linear user motion can be detected with the PDR system however, in pedestrian environments, this additional statistical testing is hard to apply. This is due to the rare occurrence of periods when a user is walking in a straight line with a constant velocity and poor HSGPS solution accuracy. Improved modeling of the statistical position and velocity correlation constraint may further improve the estimated results.

One of the major errors in the PDR mechanization, heading drift, can be solved when accurate MEMS gyros will be available on the market. The price of these systems will not be inexpensive in the near future but the use of superior quality sensors will certainly improve the accuracy of the PDR system. The other major error for the PDR mechanization, step length error, cannot be mitigated further without special hardware. This may take the form of either an RF or shoe-mounted sensor to precisely measure the step length.

In this thesis, the position of static users is not propagated forward. This is one of the biggest advantages of the PDR mechanization. However, if the HSGPS solutions are available they could be used to update the filter state vector. The influence of employing these updates on the system accuracy is an area for future study. For stationary users, the static batch GPS processing technique can also be applied to increase availability and reliability of RAIM integrity analysis.

Bibliography

Abdel-Hamid, W. (2004). An ANFIS Based Modeling of Thermal Drift of MEMS-Based Inertial Sensors. In Proceedings of ION GPS 2004 (September 21-24, Long Beach, CA), pages 784–791. Institute of Navigation, Alexandria, VA, USA.

Baarda, W. (1968). A Testing Procedure For Use In Geodetic Networks. Netherlands Geodetic Commission, Publication on Geodesy, New Series 2. No. 5, Delft, Netherlands.

Bancroft, S. (1985). An Algebraic Solution of the GPS Equations. IEEE Transactions on Aerospace and Electronic Systems, AES.21(7), pages 56–59.

Barbour, N. (2004). Inertial Navigation Sensors. NATO RTO Lecture Series 232 "Advances in Navigation Sensors and Integration Technology", 31 May - 1 June, 2004, Moscow, Russia.

Barbour, N. and G. Schmidt (2001). Inertial Sensor Technology Trends. IEEE Sensors Journal, 1(4), pages 332–339.

Basnayake, C. (2004). Automated Traffic Incident Detection Using GPS-based Transit Probe Vehicles. Ph.D. thesis, Department of Geomatics Engineering, The University of Calgary. UCGE Report 20196, available at: http://www.geomatics.ucalgary.ca/links/GradTheses.html.

Biacs, Z., G. Marshall, M. Moeglein, and W. Riley (2002). The Qualcomm/SnapTrack Wireless-Assisted GPS Hybrid Positioning System and Results from Initial Commercial Deployments. In Proceedings of ION GPS 2002 (September 22-24, Portland, Oregon), pages 378–384. Institute of Navigation, Alexandria, VA, USA.

Brand, T. and R. Phillips (2003). Foot-to-Foot Range Measurement as an Aid To Personal Navigation. In ION 59th Annual Meeting and CIGTF Guidance Test Symposium, Albuquerque, New Mexico, pages 113–121. Institute of Navigation, Alexandria, VA, USA.

Brown, R. and P. Hwang (1992). Introduction to Random Signals and Applied Kalman Filtering. John Wiley And Sons Inc., second edition edition.

Chansarkar, M. and L. J. Garin (2000). Acquisition of GPS Signals at Very Low Signal to Noise Ratio. In Proceedings of ION NTM 2000 (January 26-28, Anaheim, California), pages 731–737. Institute of Navigation, Alexandria, VA, USA.

Cohen, J. (1988). Statistical Power Analysis for the Behavioral Sciences. 2nd edition. Hillsdale, Lawrence Erlbaum Associates.

Collin, J. (2001). Inertial Navigation Techniques for Portable Applications. Master's thesis, Department of Electrical Engineering, Tampere University of Technology.

Collin, J., H. Kuusniemi, O. Mezentsev, G. MacGougan, and G. Lachapelle (2003a). HSGPS under Heavy Signal Masking - Accuracy and Availability Analysis. In 6th Nordic Radio Navigation Conference and Exhibition "NORNA 03", Stockholm-Helsinki. (available at http://plan.geomatics.ucalgary.ca).

Collin, J., G. Lachapelle, and J. Kappi (2002). MEMS-IMU for Personal Positioning in a Vehicle - A Gyro-Free Approach. In Proceedings of ION GPS 2002 (24-27 September, Portland, Oregon), pages 1153–1161. Institute of Navigation, Alexandria, VA, USA.

Collin, J., O. Mezentsev, and G. Lachapelle (2003b). Indoor Positioning System Using Accelerometry and High Accuracy Heading Sensors. In Proceedings of ION GPS 2003 (9-12 September, Portland, Oregon), pages 1164–1170. Institute of Navigation, Alexandria, VA, USA.

El-Sheimy, N. (2003). Inertial Techniques and INS/DGPS Integration. ENGO 623 Lecture Notes. Department of Geomatics Engineering, The University of Calgary.

Elwell, J. (1999). Inertial Navigation for the Urban Warrior. In SPIE Conference on Dizitization of the Battlespace IV, Orlando, Florida, volume 3709, pages 196–204.

FCC (2001). Federal Communications Commision, E-911 mandate Phase II, http://www.fcc.gov.

Gabaglio, V. (2001). Centralized Kalman Filter for Augmented GPS Pedestrian Navigation. In Proceedings of ION GPS 2001 (September 11-14, Salt Lake City, Utah), pages pp. 312–318. Institute of Navigation, Alexandria, VA, USA.

Garin, L. J., M. Chansarkar, S. Miocinovic, C. Norman, and D. Hilgenberg (1999). Wireless Assisted GPS-SiRF Architecture and Field Test Results. In Proceedings of ION GPS 1999 (September 14-17, Nashville, Tennessee), pages 489–497. Institute of Navigation, Alexandria, VA, USA.

Gartnet, G., A. Frank, and G. Retscher (2004). Pedestrian Navigation System in Mixed Indoor/Outdoor Environment - The NAVIO Project. In Proceedings of the 9th International Symposion on ICT and Planning and Impacts of ICT on Physical Space (February 25 - 27, TU Vienna).

Gelb, A. (1974). Applied Optimal Estimation. The M.I.T. Press.

Gilliéron, P.-Y., D. Buchel, I. Spassov, and B. Merminod (2004). Indoor Navigation Performance Analysis. In Proceedings of the European Navigation Conference GNSS 2004 (Rotterdam, Holland).

Godefroy, B. and M. Jeannot (2004). Indoor Positioning: New Solutions Challenging Applications. In Proceedings of the European Navigation Conference GNSS 2004 (Rotterdam, Holland).

Grewal, M., L. Weill, and A. Andrews (2001). Global Positioning Systems, Inertial Navigation and Integration. John Wiley And Sons Inc.

Haddrell, T. and A. R. Pratt (2001). Understanding The Indoor GPS Signal. In Proceedings of ION GPS 2001 (September 11-14, Salt Lake, Utah), pages 1487–1499. Institute of Navigation, Alexandria, VA, USA.

Hamilton, W. (1847). On Quaternions. In Proceedings of the Royal Irish Academy, volume 3, pages 1–10.

Hinton, P. (2004). Statistics Explained. Routledge, London/New York.

Ishlinskii, A. (1987). Classical Mechanics and Inertial Forces. Nauka. In Russian.

Jirawimut, R., S. Prakoonwit, and W. Balachandran (2003). Visual Odometer for Pedestrian Navigation. IEEE Transactions on Instrumentation and Measurement, 52(4), pages 1166–1173.

Jirawimut, R., M. Shah, P. Ptasinski, F. Cecelja, and W. Balachandran (2000). Integrated DGPS and Dead Reckoning for a Pedestrian Navigation System in Signal Blocked Environments. In Proceedings of ION GPS 2000 (September 19-22, Salt Lake, Utah), pages 1741–1747. Institute of Navigation, Alexandria, VA, USA.

Kalman, R. (1960). A New Approach to Linear Filtering and Prediction Problems. ASME Journal of Basic Engineering, pages 35–45.

Kaplan, E. (1996). Understanding GPS: Principles And Applications. Artech House, Inc.

Kelly, R. (1988). The Linear Model, RNP, and the Near-Optimum Fault Detection and Exclusion Algorithm. Invited paper in papers published in NAVIGATION, Volume V, Institute of Navigation (GPS Redbooks), pages 227–259.

Klukas, R., G. Lachapelle, and M. Fattouche (1997). Field Tests of a Cellular Telephone Positioning System. In Presented at IEEE VTC '97 - 47th Annual International Vehicular Technology Conference, Phoenix, AZ.

Kourogi, M. and T. Kurata (2003). A Wearable Augmented Reality System with Personal Positioning Based on Walking Locomoition Analysis. In Proceedings of the Second IEEE and ACM International Symposium on Mixed and Augmented Reality (ISMAR' 03).

Kuang, S. (1996). Geodetic Network Analysis and Optimal Design. AnnArbor Press, Michigan.

Kuusniemi, H. and G. Lachapelle (2004). GNSS Signal Reliability Testing in Urban and Indoor Environments. In Proceedings of ION National Technical Meeting 2004 (January 26-28, San Diego, CA), pages 210–224. Institute of Navigation, Alexandria, VA, USA.

Kuusniemi, H., G. Lachapelle, and J. Takala (2004). Reliability in Personal Positioning. In Proceedings of the European Navigation Conference ENC-GNSS 2004, Rotterdam, The Netherlands, 16-19 May.

Lachapelle, G. (2003). NAVSTAR GPS: Theory and Applications. ENGO 625 Lecture Notes. Department of Geomatics Engineering, The University of Calgary.

Lachapelle, G. (2004). GNSS-Based Indoor Location Technologies. In CD-ROM Proceedings of the International Symposium on GPS/GNSS, Sydney, Australia (6-8 December), 15 pages.

Lachapelle, G., H. Kuusniemi, D. Dao, G. MacGougan, and M. Cannon (2003a). HSGPS Signal Analysis and Performance Under Various Indoor Conditions. In Proceedings of ION GPS 2003 (September 9-12, Portland, Oregon). Institute of Navigation, Alexandria, VA, USA.

Lachapelle, G., H. Kuusniemi, D. Dao, G. MacGougan, and M. Cannon (2004). HSGPS Signal Analysis and Performance Under Various Indoor Conditions. Journal of the U.S. Institute of Navigation, 51(1), pages 29–43.

Lachapelle, G., O. Mezentsev, J. Collin, and G. MacGougan (2003b). Pedestrian and vehicular Navigation Under Signal Masking Using Integrated HSGPS and Self-Contained Sensor Technologies. In CD-ROM Proceedings of 11th IAIN World Congress 2003, Berlin, Germany.

Ladetto, Q. (2000). On Foot Navigation: Continuous Step Calibration using Both Complimentary Recursive Prediction and Adaptive Kalman Filtering. In Proceedings of ION GPS 2000 (September 19-22, Salt Lake, Utah), pages 1735–1740. Institute of Navigation, Alexandria, VA, USA.

Ladetto, Q., V. Gabaglio, and B. Merminod (2001). Two Different Approaches for Augmented GPS Pedestrian Navigation. In Proceedings of the International Symposium on Location Based Services for Cellular Users, Locellus 2001.

Lee, S.-W. and K. Mase (2001). Recognition of Walking Behaviors. In Proceedings of the 2001 IEEE International Conference on Control Applications, Mexico city, Mexico, pages 1152–1155.

Leick, A. (1995). GPS Satellite Surveying. John Wiley And Sons Inc.

Leva, J. (1996). An alternative Closed-Form Solution to the GPS Pseudorange Eqations. IEEE Transaction on Aerospace and Electronic Systems, 32(4), pages 1430–1439.

Levi, R. and T. Judd (1999). Dead Reckoning Navigation System Using Accelerometer to Measure Foot Impacts. US patent.

Ma, C. (2003). Techniques to Improve Ground-Based Wireless Location Performance Using a Cellular Telephone Nework. Ph.D. thesis, Department of Geomatics Engineering, The University of Calgary. UCGE Report 20177, available at: http://www.geomatics.ucalgary.ca/links/GradTheses.html.

MacGougan, G. (2003). High Sensitivity GPS Performance Analysis in Degraded Signal Environments. Master's thesis, Department of Geomatics Engineering, The University of Calgary. UCGE Report 20176, available at: http://www.geomatics.ucalgary.ca/links/GradTheses.html.

MacGougan, G., G. Lachapelle, R. Klukas, K. Siu, L. Garin, J. Shewfelt, and G. Cox (2002). Performance Analysis of A Stand-Alone High Sensitivity Receiver. GPS Solutions, Springer Verlag, 6(3), pages 179–195.

Mezentsev, O. (2004). Self-Contained Sensor Aided Kinematic HSGPS Positioning Algorithm. In Proceedings of ION GPS 2004 (September 21-24, Long Beach, CA), pages 2468–2478. Institute of Navigation, Alexandria, VA, USA.

Mezentsev, O., J. Collin, H. Kuusniemi, and G. Lachapelle (2004). Accuracy Assessment of a High Sensitivity GPS Based Pedestrian Navigation System Aided by Low-Cost Sensors. In Proceedings of 11th Saint Petersburg International Conference on Integrated Navigation Systems, Russia, pages 156–164.

Mezentsev, O., J. Collin, and G. Lachapelle (2003). Vehicular Navigation in Urban Canyons Using a High Sensitivity Receiver Augmented with a Medium Grade IMU. In Proceedings of 10th Saint Petersburg International Conference on Integrated Navigation Systems, Russia, pages 64–70.

Misra, P. and P. Enge (2001). Global Positioning System: Signals, Measurements and Performance. Ganga-Jamuna Press.

Parkinson, B. and J. Spilker (1996). Global Positioning System: Theory And Applications, Volumes 1 and 2. American Institute of Aeronautics and Astronautics, Inc.

Peterson, B., D. Bruckner, and S. Heye (1997). Measuring GPS Signals Indoors. In Proceedings of ION GPS 1997 (September 16-19, Kansas City, Missouri), pages 615–624. Institute of Navigation, Alexandria, VA, USA.

Ray, J. (2000). Mitigation of GPS Code and Carrier Phase Multipath Effects Using a Multi-antenna System. Ph.D. thesis, Department of Geomatics Engineering, The University of Calgary. UCGE Report 20136, available at: http://www.geomatics.ucalgary.ca/links/GradTheses.html.

Ray, J. (2002). Advanced GPS Receiver Technology. ENGO 699.73 Lecture Notes. Department of Geomatics Engineering, The University of Calgary.

Ryan, S. (2002). Augmentation of DGPS for marine navigation. Ph.D. thesis, Department of Geomatics Engineering, The University of Calgary. UCGE Report 20164, available at: http://www.geomatics.ucalgary.ca/links/GradTheses.html.

Savage, P. (1998). Strapdown Inertial Navigation Integration Algorithm Design. Part 1: Attitude Algorithms. Journal of Guidance, Control, and Dynamics, 21(1), pages 19–28.

Scherzinger, B. (2004). Estimation with Application to Navigation. ENGO 699.11 Lecture Notes. Department of Geomatics Engineering, The University of Calgary.

Shkel, A. (2001). Micromachined Gyroscopes: Challenges, Design Solutions, and Opportunities. In Smart Structures and Materials 2001, Proceedings of SPIE, Vol. 4334.

Soderholm, S., T. Juhola, T. Saarnimo, V. Karttunen, and T. Toivanen (2001). Indoor Navigation Using a GPS Receiver. In Proceedings of ION GPS 2001 (September 11-14, Salt Lake, Utah), pages 1479–1486. Institute of Navigation, Alexandria, VA, USA.

Stirling, R., K. Fyfe, and G. Lachapelle (2005). Evaluation of a New Method of Heading Estimation for Pedestrian Dead Reckoning Using Shoe Mounted Sensors. Journal of Navigation, Royal Society of Navigation, Cambridge University Press, 58(1), pages 31–45.

Syrjärinne, J. (2001). Studies of Modern Techniques for Personal Positioning. Ph.D. thesis, Tampere University of Technology, Tampere, Finland.

Teunissen, P. (1998). Quality Control and GPS, Chapter 7 in GPS for Geodesy. Springer, New York.

Titterton, D. and J. Weston (1997). Strapdown Inertial Navigation Technology. Peter Peregrinus Ltd.

Torge, W. (1991). Geodesy. de Gruyter.

van Dierendonck, A. J., P. Fenton, and T. Ford (1992). Theory and Performance of Narrow Correlator Spacing in a GPS receiver. NAVIGATION: Journal of The Institute of Navigation, 39(3), pages 265–283.

van Diggelen, F. (2001a). Global Locate Indoor GPS Chipset & Services. In Proceedings of ION GPS 2001 (September 11-14, Salt Lake, Utah), pages 1515–1521. Institute of Navigation, Alexandria, VA, USA.

van Diggelen, F. (2001b). Indoor GPS: Wireless Aiding And Low Signal Strength Detection. NAVTECH Seminar Course Notes, (March 22, 2001, San Diego, CA).

Webster, J. (1999). Measurement, Instrumentation, and Sensors Handbook. CRC Press.

Weinberg, H. (2003). Modifying the Range of the ADXRS150 and ADXRS300 Rate Gyros. Analog Devices Application Note, AN-625.

Wieser, A. (2001). Robust and fuzzy techniques for parameter estimation and quality assessment in GPS. Ph.D. thesis, Graz University of Technology.